AD-A057 128 SCIENCE APPLICATIONS INC LA JOLLA CALIF F/G 20/1
ACOUSTIC PROPAGATION IN RANDOM OCEANS USING THE TRANSPORT EQUAT--ETC(U)
APR 78 H L WILSON, F D TAPPERT N00014-77-C-0583
UNCLASSIFIED SAI-78-639-LJ NL

1 OF 2
AD
A057 128

NORDA-500

(14) SAI-78-639-LJ

LEVEL II

(2)

(6) ACOUSTIC PROPAGATION IN RANDOM OCEANS USING THE TRANSPORT EQUATION.

(12) 150 p.

by

(10) H. L. Wilson
F. D. Tappert

(11) 18 April 1978

(9) Final Report for Period 11 July 1977 to 31 January 1978

(15) Contract No. N000014-77-C-0583 new

SCIENCE APPLICATIONS, INC.
1200 Prospect Street, P. O. Box 2351
La Jolla, California 92038

TABLE OF CONTENTS

TABLE OF CONTENTS (continued)

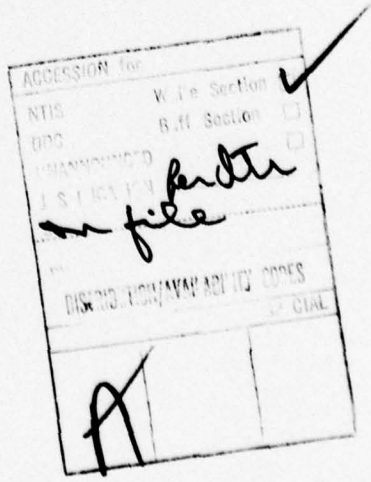

LIST OF FIGURES

LIST OF FIGURES (continued)

LIST OF FIGURES (continued)

LIST OF FIGURES (continued)

LIST OF FIGURES (continued)

LIST OF TABLES

1. INTRODUCTION

This document constitutes the final report for Navy Contract N00014-77-C-0583, which was funded by NORDA (Naval Ocean Research and Development Agency, Code 500) covering the period from 11 July 1977 to 1 January 1978. The object of the research performed under the contract was to adapt an existing radiation transport code for use in underwater acoustic propagation and to apply it to a surface duct propagation problem. The new computer code resulting from the efforts of this contract is called ACTOR (Acoustic Transport in an Ocean that is Random).

During the past three decades the study of sound propagation in the ocean has received considerable theoretical and experimental study. The theoretical state-of-the-art circa 1970 is fairly well summarized in the books by Officer[1] and Urick[2] which also contain references to a vast amount of experimental data. Up to 1970 the theoretical studies were restricted primarily to deterministic oceans using either ray trace codes or normal mode codes. This does not mean that fluctuation phenomena had not been encountered. As long ago as 1947[3] experimental data indicated that the instantaneous reverberation amplitude is Rayleigh distributed. To treat such a problem theoretically requires detailed oceanographic data as well as advanced numerical methods. With the advent of the parabolic equation (PE) method by Tappert and Hardin[4] and Tappert[5] and the transport equation technique by Besieris and Tappert,[6,7] fluctuation phenomena can be treated theoretically in both the long and short wavelength regimes. The inadequacy of the oceanographic data is, however, still a stumbling block for high frequency active sonar fluctuation studies.

In the low frequency regime where acoustic propagation over intercontinental distances can be considered, the characteristics of the deep sound channel become important. It is now generally accepted that fluctuation phenomena in this case are due to the presence of internal waves. For many regions of the world's oceans the space-time scales of

these internal waves are accurately described by the Garrett-Munk model.[8,9] This model of internal waves in conjunction with the PE method has been used by Flatte' and Tappert[10] to describe low frequency fluctuation phenomena in the deep sound channel.

At higher frequencies, where the demands of a finer space grid make calculations using the PE method impractical for fluctuation studies, the transport equation finds one of its natural areas of application. However, because the transport equation is completely new to ocean acoustics, we felt that it should first be applied to an area where experimental data exist. To this end we selected the surface duct propagation study reported by Pedersen and Gordon.[11] While the data reported in Reference 11 goes out to 10 kyd, longer range data to about 65 kyd was generously provided by Pedersen.[12] Of particular interest to us was the cross layer propagation data at 1030 Hz. Beyond 6 kyd neither ray theory nor normal mode theory can adequately account for the level of ensonification observed at the 400 ft, below duct, receiver. Using the transport equation, which can easily incorporate scattering by rough surfaces and by internal waves, we investigated the possibility that these energy transfer mechanisms could account for the energy removed from the surface duct and detected by the receiver below the duct.

The remainder of this report is organized as follows. The second section contains a brief discussion of the transport equation and a rather more detailed description of how Monte Carlo methods are used to obtain its solution. The various scattering kernels used are taken up in Section 3. The experimental data and a comparison of it with the results from normal mode theory and transport theory are presented in Section 4. Various conclusions drawn from the results of our studies are given in Section 5. The acknowledgements of the persons and organizations whose help has been essential for the successful completion of this work are reserved for Section 6. Finally, the references are provided in Section 7. Appendix A contains the results of a preliminary test problem in which the transport code with no scattering mechanisms was compared with a ray theory code and Appendix B is used to discuss our random number generator.

2. THE ACOUSTIC TRANSPORT EQUATION

In this section we provide a simplified description of how the transport equation can be obtained from the parabolic equation. No attempt is made at mathematical rigor and no implication is implied that this is the only way to obtain the transport equation. It is done this way only to show that there is a connection between the transport equation and the parabolic equation which is now in general use in the underwater acoustics community.

2.1 DERIVATION OF THE TRANSPORT EQUATION

We start with the parabolic equation in range r and depth z

$$i \frac{\partial \psi}{\partial r} + \frac{1}{2k} \frac{\partial^2 \psi}{\partial z^2} + \frac{k}{2} \left[\left(\frac{c_o^2}{c^2} - 1 \right) \right] \psi = 0 \quad . \tag{2.1}$$

Letting $c = c_d + \delta c_s$ we can put Eq. (2.1) in the form

$$i \frac{\partial \psi}{\partial r} + \frac{1}{2k} \frac{\partial^2 \psi}{\partial z^2} + V(r,z)\psi = 0 \quad . \tag{2.2}$$

where

$$k = \text{acoustic wave number} = \omega / c_o \quad .$$

ψ is a complex function from which the pressure field is obtained as

$$P(r,z,t) = f(r,z) e^{-i\omega t} \quad .$$

where

$$f(r,z) = \psi(r,z) H(kr) \quad .$$

and $H(kr)$ is the outgoing Hankel function

$$H(kr) \sim \sqrt{\frac{2}{\pi kr}}\, e^{i(kr-\pi/4)}$$

appropriate for 2-D cylindrically symmetric solutions.

Here

$$V(r,z) = \left[\frac{k}{2}\left(\frac{c_o^2}{c_d^2} - 1\right) - k\,\frac{\delta c_s}{c_o}\right] \qquad (2.3)$$

and c_d and c_s are the deterministic and stochastic part of the sound speed, respectively, and c_o is a reference sound speed.

This is mathematically equivalent to the Schroedinger equation with $t \to r$. In Eq. (2.3) δc_s is a random function and should be written $\delta c_s(r,z,\alpha)$ where a given α picks out a member of the ensemble of possible δc_s functions. Now, Eq. (2.2) can be written

$$i\psi^*(r,z_1)\,\frac{\partial\psi(r,z_2)}{\partial r} + \frac{1}{2k}\,\frac{\partial^2}{\partial z_2^2}\,[\psi^*(r,z_1)\psi(r,z_2)]$$

$$+ V(r,z_2)\psi^*(r,z_1)\psi(r,z_2) = 0 \quad . \qquad (2.4)$$

Also

$$- i\psi(r,z_2) \frac{\partial \psi^*(r,z_1)}{\partial r} + \frac{1}{2k} \frac{\partial^2}{\partial z_1^2} [\psi(r,z_2)\psi^*(r,z_1)]$$

$$+ V(r,z_1)\psi^*(r,z_1)\psi(r,z_2) = 0 \quad . \qquad (2.5)$$

Subtracting Eq. (2.5) from (2.4) and defining

$$\rho(r,z_1,z_2) \equiv \psi^*(r,z_1)\psi(r,z_2) \qquad (2.6)$$

we see that ρ satisfies the equation

$$i \frac{\partial \rho}{\partial r} + \frac{1}{2k} \frac{\partial^2 \rho}{\partial z_2^2} - \frac{1}{2k} \frac{\partial^2 \rho}{\partial z_1^2} + \left[V(r,z_2,\alpha) - V(r,z_1,\alpha) \right] \rho = 0 \quad . \qquad (2.7)$$

For propagation primarily in the r-direction (i.e., small θ) we see from Figure 2.1 that the wave vector in the z-direction is approximately $k\theta$.

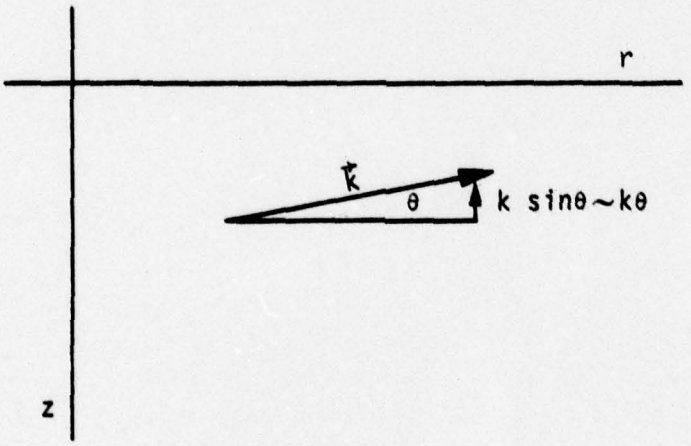

Figure 2.1. Wave Vector Diagram.

If we now introduce the Wigner distribution[13]

$$f(r,z,\theta) = \frac{k}{\pi}\int_{-\infty}^{\infty} dz'\, e^{2ik\theta z'}\, \psi^*(r,z+z')\psi(r,z-z') \qquad (2.8)$$

we see that if Equation (2.7) is operated on by $\frac{k}{\pi}\int_{-\infty}^{\infty} dz'\, e^{ik\theta z'}$ we get

$$i\,\frac{\partial f}{\partial r} = \frac{k}{2k\pi}\int_{-\infty}^{\infty} dz'\, e^{i2k\theta z'}\left[\frac{\partial^2\psi^*(r,z+z')}{\partial(z+z')^2}\psi(r,z-z') - \psi^*(r,z+z)\,\frac{\partial^2\psi(r,z-z')}{\partial(z-z')^2}\right]$$

$$+\frac{k}{\pi}\int_{-\infty}^{\infty} dz'\, e^{i2k\theta z'}\left[V(r,z+z',\alpha) - V(r,z-z',\alpha)\right]\psi^*(r,z+z')\psi(r,z-z') \quad . \qquad (2.9)$$

Omitting the details one can, by an integration by parts, put Eq. (2.9) in the form

$$\frac{\partial f}{\partial r} + \theta\,\frac{\partial f}{\partial z} = \frac{k}{i\pi}\int dz'\, e^{2ik\theta z'}\left[V_1(z+z') - V_1(z-z')\right]\psi^*(z+z')\psi(z-z')$$

$$+\frac{k}{i\pi}\int dz'\, e^{2ik\theta z'}\left[V_2(z+z',\alpha) - V_2(z-z',\alpha)\right]\psi^*(z+z')\psi(z-z') \qquad (2.10)$$

where

$$V_1 = \frac{k}{2}\left(\frac{c_o^2}{c_d^2} - 1\right) \qquad (2.11)$$

$$V_2 = -\,k\,\frac{\delta c_s(r,z,\alpha)}{c_o} \quad . \qquad (2.12)$$

The function f is implicitly understood to be a function of the stochastic part of the index of refraction, i.e., of α. Taylor

expanding $V_1(z + z')$ about the point $z - z'$ we can obtain the transport equation

$$\frac{\partial f}{\partial r} + \theta \frac{\partial f}{\partial z} + \frac{1}{2} \frac{\partial}{\partial z}\left(\frac{c_o^2}{c_d^2} - 1\right)\frac{\partial f}{\partial \theta}$$

$$= \frac{k}{i\pi} \int dz' \, e^{2ik\theta z'} \left[V_2(z+z',\alpha) - V_2(z-z',\alpha)\right] \psi^*(z+z')\psi(z-z') \quad (2.13)$$

where the entire stochastic aspect of the problem is contained in the integral on the right hand side. Averaging this equation over the ensemble of possible δc_s Besieris and Tappert[6,7] show that the following equation results

$$\frac{\partial F}{\partial r} + \theta \frac{\partial F}{\partial z} + \frac{1}{2} \frac{\partial}{\partial z}\left(\frac{c_o^2}{c_d^2} - 1\right)\frac{\partial F}{\partial \theta}$$

$$= \int d\theta' W(z,\theta,\theta')\left[F(r,z,\theta') - F(r,z,\theta)\right] - \nu(z)F \quad (2.14)$$

where $F(r,z,\theta) = \langle f(r,z,\theta,\alpha)\rangle$. This is a transport equation for small angle scattering where the scattering is determined by the kernel $W(z,\theta,\theta')$. The deterministic part of the index of refraction leads to the third term on the left side and accounts for the gradual bending of the rays. The last term accounts for volume absorption with depth dependent absorption coefficient $\nu(z)$ (measured in inverse range units).

The details of the scattering kernel $W(\theta,\theta')$ are taken up in Section 3.

The physical significance of the function F that satisfies the transport equation can be seen as follows. From Eq. (2.8) we find

$$I(r,z) \equiv \int F(r,z,\theta)d\theta = \langle|\psi(r,z)|^2\rangle \quad . \quad (2.15)$$

Thus the integral of F over angle gives the mean acoustic intensity at depth z and range r. This is just what is needed to compute the average transmission loss. Furthermore,

$$J(r,z) \equiv \int F(r,z,\theta)\theta d\theta = \left\langle -\frac{i}{2k}\left(\psi^* \frac{\partial\psi}{\partial z} - \psi \frac{\partial\psi^*}{\partial z}\right)\right\rangle \quad . \qquad (2.16)$$

The right hand side is just the mean vertical flux of acoustic energy as can be seen by writing ψ in polar coordinates, $\psi = Ae^{i\phi}$. Defining the geometrical vertical angle as the vertical phase derivative, $\Theta = \frac{1}{k}\frac{\partial\psi}{\partial z}$, we obtain

$$I(r,z) = \langle A^2(r,z)\rangle \quad , \qquad (2.17a)$$

$$J(r,z) = \langle A^2(r,z)\Theta(r,z)\rangle \quad . \qquad (2.17b)$$

In fact, F contains information equivalent to the mutual coherence function since the Fourier transform of F with respect to θ yields

$$n(r,z,\zeta) \equiv \int F(r,z,\theta)e^{-2ik\theta\zeta}d\theta = \langle\psi^*(r,z+\zeta)\psi(r,z-\zeta)\rangle \; . \qquad (2.18)$$

Therefore, the transport equation (2.14) may be viewed as an equation for *the mutual coherence function.* As the range r increases, i.e., as the separation between source and receiver increases, the coherence of the acoustic field decreases and this effect is just what Eq. (2.14) describes.

Other derivations of the transport equation can be found in References 14 - 17.

2.2 VALIDITY CONDITIONS FOR THE TRANSPORT EQUATION

For the transport equation, as given by Eq. (2.14), to be an accurate representation of the full elliptic wave equation in a medium with random inhomogeneities several conditions must be met. These

conditions, as summarized by Watson,[17] are:

1. We require $\alpha\lambda << 1$ where α is the extinction coefficient and λ is the acoustic wavelength. Using a wavepacket picture this condition says that the front of the packet should not undergo significant extinction relative to the back, i.e., the packet should not suffer severe distortion from its original form. In this case it may change direction but still will represent a particle with given momenta;

2. The eikonal approximation must be valid in the absence of internal wave scattering; and

3. To obtain Eq. (2.14) the long-time Markovian approximation was invoked. This requires that $F(r,z,\theta)$ vary slowly over the horizontal diffusion length.

2.3 THE MONTE CARLO METHOD OF SOLUTION

2.3.1 Introduction

The transport equation derived in Section 2.1 is used extensively in many areas of physics, including radiative transfer in stellar atmospheres, neutron transport in nuclear reactors, and to calculate the x-ray, neutron, and gamma outputs from nuclear weapons. Because most of these applications involve complex geometries, realistic cross sections and/or are non-linear, a vast amount of effort has been devoted to developing numerical methods for solving the transport equation. In one-dimensional geometries the predominance of effort has been spent on finite difference techniques, many of which are described by Richtmyer and Morton.[18]

For two- and three-dimensional problems the geometrical complexities encountered in many uses has led to the development of sophisticated Monte Carlo methods. As applied to neutron transport the Monte Carlo method is aptly described in Reference 19 while the method as applied to non-linear thermal radiation transport is discussed by Fleck.[20,21]

The problem of calculating acoustic propagation through the ocean is complicated, from the finite difference viewpoint, because of the refractive nature of the deterministic part of the sound speed profile. This is compounded by the fact that the fluctuating part of the profile results in predominantly forward scattering at very small angles. For this reason we have selected the Monte Carlo method to use as the basis for obtaining numerical solutions of the acoustic transport equation as it is represented by Eq. (2.14). It is easily adaptable to complex geometries and complex media. In addition, the Monte Carlo method is readily modified to accept changes or additions to the physics, it is easy to incorporate time dependence into it, and a multigroup description of the field can easily be included.

There is a vast literature available concerning the many facets of the Monte Carlo method and its applications. Subsections 2.2.2 and 2.3.3 provide only a brief glimpse of certain important features of the Monte Carlo technique. Finally, subsection 2.3.4 discusses how the Monte Carlo method is applied to the specific problem of acoustic propagation in a realistic ocean environment.

2.3.2 Sampling Techniques

The major fundamental difference between the Monte Carlo method and other methods of obtaining the solution to a given physical or mathematical problem is its reliance on random sampling to represent certain features of the problem. And basic to all random sampling techniques is the availability of a set of random numbers, ξ , which are uniformly distributed on the interval (0,1]. The random number generator which we use is described in Appendix B along with the results of several "goodness" tests.

(a) Function Sampling

To construct the Monte Carlo solution of a transport problem there exists a function which describes the probability that a Monte Carlo

particle will go a distance x before scattering. The probability of the particle undergoing a first collision between x and $x + dx$ is given by

$$p(x)dx = e^{-\sigma x}\sigma dx \tag{2.19}$$

where σ is the macroscopic cross section of the medium and is interpreted as the probability per unit length of undergoing a collision. Integrating the right side of (2.19) from $x = 0$ to x' and calling the result ξ, gives

$$\xi = \int_0^{x'} e^{-\sigma x}\sigma dx$$

$$= 1 - e^{-\sigma x'} ,$$

or,

$$x' = -\frac{1}{\sigma} \ln \xi \quad . \tag{2.20}$$

By sampling ξ uniformly on $(0,1]$, Eq. (2.20) provides the correct probability distribution for the distance to collision. This example was selected because it is used later in sampling the distance which an "acoustic" particle or ray goes before scattering.

In general, if $p(x)$ is a probability density function on the interval $a \leq x < b$, then

$$\xi = P(x) = \int_a^x p(x)dx \tag{2.21}$$

determines x uniquely as a function of ξ. Often an analytic solution for x cannot be obtained, and either iterative methods must be used or tables of partial integrals (obtained numerically) can be employed.

(b) Biasing and Importance Sampling

Biasing and importance sampling are really only slightly different aspects of the same thing. A more detailed discussion of these ideas can be found in Reference 22. We will present an example of biasing and importance sampling to indicate the general principles involved. To make this example relevant to the acoustics problem consider the situation shown in Figure 2.2. Here we have a region of

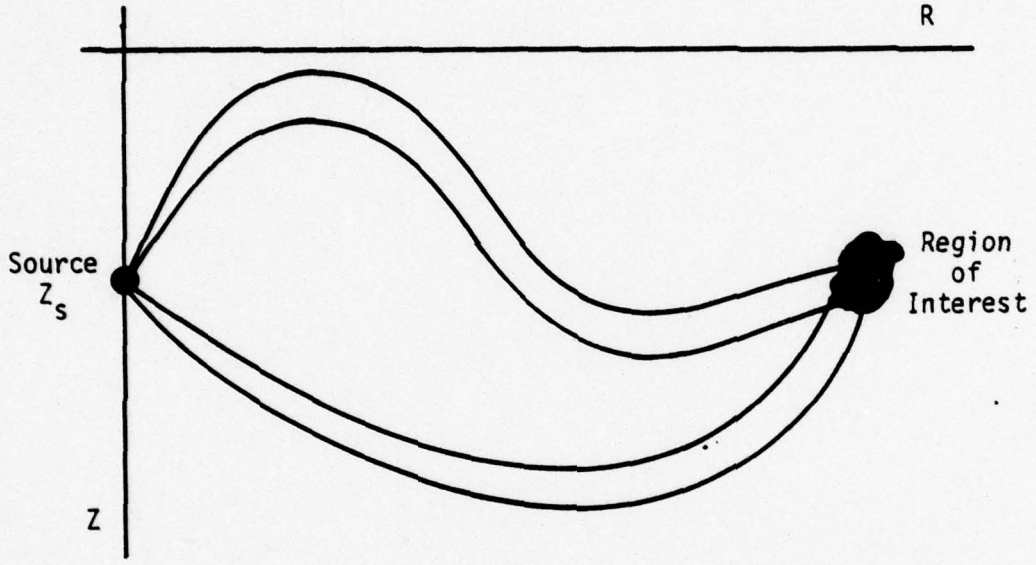

Figure 2.2. Schematic of Biasing in Underwater Acoustic Propagation.

interest where, say, either the propagation loss and/or the angular distribution of the acoustic intensity due to the source at $R = 0$, $Z = Z_s$ is required. Since, as indicated, only rays which lie in the two bands will pass through the region of interest, we importance sample the source so that the vast majority of rays are emitted in these two bands. Then, to account for the overemphasis on the number of rays in these two bands, we bias their weights to properly represent the energy being emitted into these two small angular intervals. The variances of the answers predicted in the region of interest typically are proportional to $1/\sqrt{N}$ where N

is the number of rays contributing to the answer. Hence, by increasing N we reduce the variance.

(c) Estimators

Typically in forward analog Monte Carlo four types of estimators are encountered, generally only one or two in any given problem. These are called the collision estimator, the last event estimator, the track-length estimator, and the point-detector estimator. The acoustic transport problem has two cross sections which characterize the medium. These are the absorption cross section, σ_a , and the scattering cross section, σ_s , which combine to form a total cross section $\sigma_T = \sigma_a + \sigma_s$.

In the usual acoustic transport calculation the ocean is divided up into zones of varying sizes (see Figure 2.3) which all have the property that as far as absorption is concerned they are "optically" thin, i.e., $\sigma_a \Delta x << 1$ where Δx is the maximum dimension of the zone. To calculate the acoustic absorption in a given zone using the collision

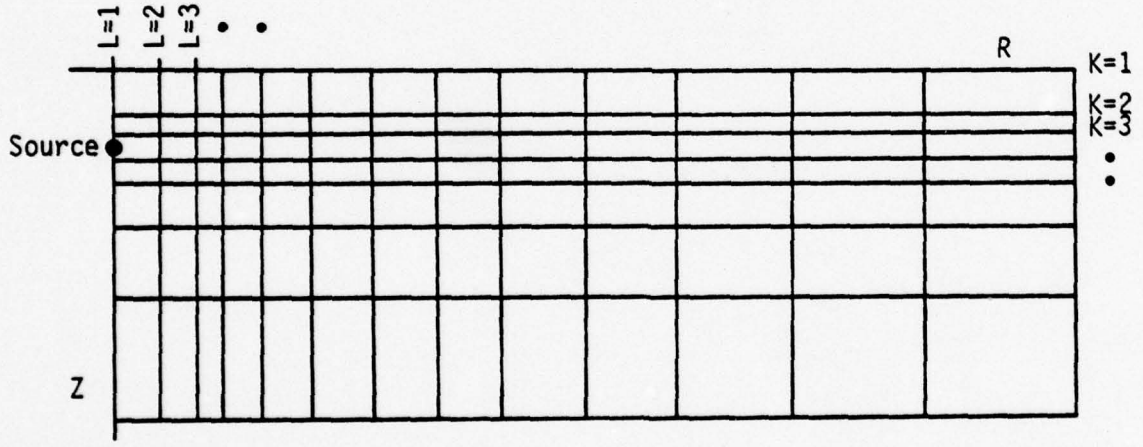

Figure 2.3. Typical Zoning for an Acoustics Problem.

estimator, we would tally $E\ \sigma_a/\sigma_t$ at each collision which takes place in that zone and reduce the weight E accordingly. In the last event estimator the particle is killed when $\xi < \sigma_a/\sigma_t$, and its entire weight is scored

in the zone in which it died. If the random number $\xi \geq \sigma_a/\sigma_t$ scattering occurs and no weight is lost. The collision estimator as well as the last event estimator lead to poor statistical results in optically thin regions. Because the acoustic absorption coefficient is so small, i.e., $1/\sigma_a >> \Delta x$ where Δx is the maximum zone size, we must consider a better estimator, the path-length estimator. The path-length estimator scores the quantity $E\, e^{-\sigma_a s}$ in the zone for which the corresponding path length is s. As discussed in Reference 22 the relative error of the path-length estimator is much less than either of the other two discussed above.

The point detector estimator would not be particularly useful because of the refractive nature of the medium and hence will not be discussed.

2.3.3 Variance Reduction

(a) Central Limit Theorem and Variance Calculation

The variance calculation which will be incorporated into the acoustic transport code is based on the one described by Cashwell and Everett[23] which makes use of the central limit theorem. For the purpose of describing the application of this theorem, let us define an experiment E as placing a Monte Carlo particle in the system and tracking it completely out of the system (even if it is carrying 0 weight). Now define a sample space Ω as all the possible histories of the above initial particle placements and paths through the system. Also, define a random variable x_i on this sample space Ω as

$$x_i = \begin{cases} \text{weight of particle at exit, if history } i \text{ of } \Omega \text{ exits in angular group } \alpha \text{ and frequency group } \nu. \\ 0, \text{ if history } i \text{ of } \Omega \text{ exits in some angular group } \alpha' \neq \alpha \text{ or frequency group } \nu' \neq \nu. \end{cases}$$

Assume the experiment E is performed N different times (N Monte Carlo particle trackings), and form the sum

$$S_N = x_1 + \ldots + x_N \quad . \tag{2.22}$$

Notice that the x_i are mutually independent with the same probability distribution. If we let

$$\begin{aligned} \mu &= \text{expectation, or mean, of } x_i \text{ (same for all } x_i) \\ b &= \sigma^2 = \text{variance of } x_i \text{ (same for all } x_i) \end{aligned} \tag{2.23}$$

then the central limit theorem states

$$P\left(\left|\frac{S_N}{N} - \mu\right| < \mu\varepsilon\right) = \operatorname{erf}\left(\frac{N\mu\varepsilon}{\sqrt{2bN}}\right) \quad \text{as} \quad N \to \infty \tag{2.24}$$

$$P\left(\left|S_N - N\mu\right| \leq N\mu\varepsilon\right) = \operatorname{erf}\left(\frac{N\mu\varepsilon}{\sqrt{2bN}}\right) \quad \text{as} \quad N \to \infty \tag{2.25}$$

where $\operatorname{erf}(x)$ is the well known "error function"

$$\operatorname{erf}(x) = \frac{2}{\sqrt{\pi}} \int_0^x e^{-t^2} dt \tag{2.26}$$

which is tabulated and drawn in Figure 2.4.

In a radiation transport calculation, we are interested in the probability that the calculated total weight exiting the system in a particular angular group and frequency group, as determined by tracking N Monte Carlo particles through the system, is within the true theoretical value by a factor ε. We can use the central limit theorem in the above form to give us an estimate of this measure of accuracy by making the following approximations in the right-hand side of Eq. (2.25):

1. Replace $N\mu$ by S_N ; and
2. Replace b by

$$\sum_{i=1}^{N} \frac{(x_i)^2}{N} - \left(\frac{S_N}{N}\right)^2 \quad . \tag{2.27}$$

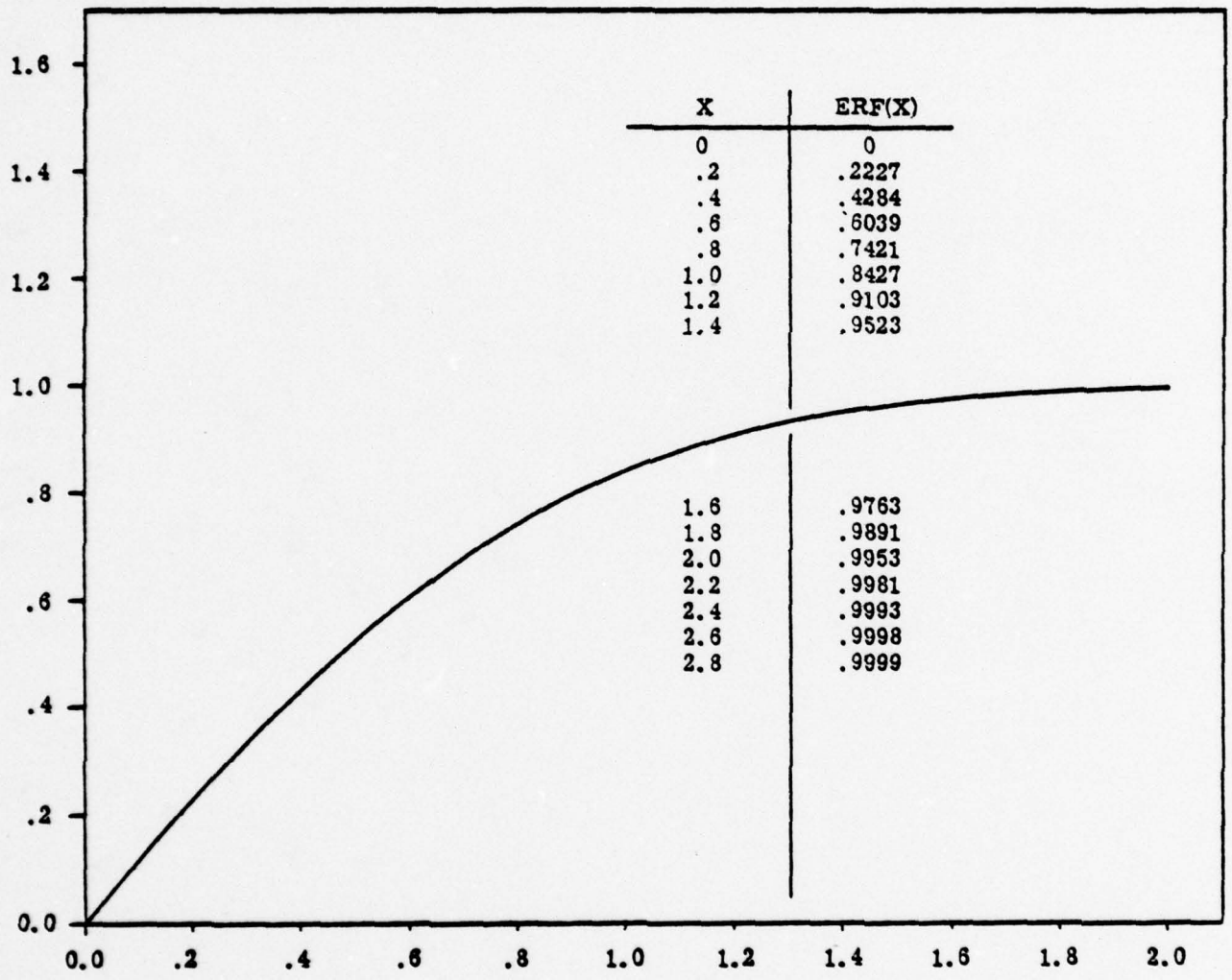

X	ERF(X)
0	0
.2	.2227
.4	.4284
.6	.6039
.8	.7421
1.0	.8427
1.2	.9103
1.4	.9523
1.6	.9763
1.8	.9891
2.0	.9953
2.2	.9981
2.4	.9993
2.6	.9998
2.8	.9999

Figure 2.4. Plot of Error Function Versus its Argument.

In the acoustics code we are interested in the error bars to be put on the dB loss points. Thus,

$$\text{dB loss} = 10 \log_{10}\left(\frac{I}{I_o}\right) \tag{2.28}$$

$$\Delta(\text{dB loss}) = 10 \log_{10} e \; \Delta \ell n \left(\frac{I}{I_o}\right)$$

$$= 4.3 \frac{\Delta I}{I} \quad . \tag{2.29}$$

ΔI is obtained by summing over the product of the particles weight and path length in a zone. Now we want the errors to imply that if the same calculation (with different random number sequence) were repeated, the results would lie within the error bars with 2/3 probability.

So, given

$$N\mu \cong S_N$$

and

$$b \cong \sum \frac{x_i^2}{N} - \left(\frac{S_N}{N}\right)^2$$

we can find ε such that $\text{erf}(S_N \varepsilon / \sqrt{2bN}) = 2/3$. With this ε we then set the error bars in dB loss as follows:

$$\Delta(\text{dB loss}) = 4.3(2\varepsilon) \tag{2.30}$$

Thus, the top of the error bar is at dB loss - $\varepsilon(4.3)$ and bottom is at dB loss + $\varepsilon(4.3)$.

(b) Splitting and Russian Roulette

The usefulness of splitting and Russian Roulette is very limited in acoustic transport applications. The primary reason is that

the typical absorption coefficients for frequencies of interest are so small that over the distances of interest only a small fraction of the particles weight is lost. Furthermore, the distances which two different particles might traverse in going from source to "detector" do not differ significantly. Thus, all particles arriving at the detector do so with almost the same weight. Splitting and Russian Roulette, on the other hand, are most useful when the particles arrive with a wide spread in weights. In such a case it is advantageous to kill the low weight particles or particles unlikely to contribute to the answer with probability p and to multiply the weight if it survives (probability $1 - p$) by the factor $1/p$. In a like manner a particle of weight, E, which enters a region of interest might be split into n identical particles each of weight E/n.

2.3.4 Simulating Particle Transport

(a) Source Sampling

The solution of the transport equation for acoustic propagation by Monte Carlo methods begins by sampling the source. The sampling procedure is shown in Figure 2.5. We assume an isotropic source

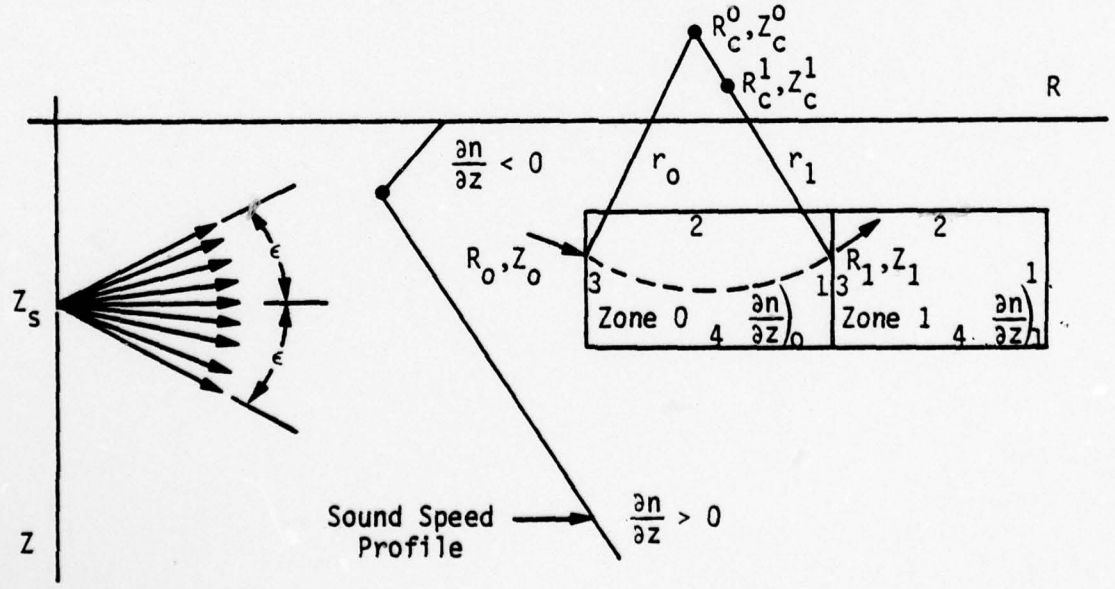

Figure 2.5. Source Sampling and Tracking Schematic.

at depth Z_s. For typical problems there is only a limited range of initial angles for which energy can propagate to large ranges. This range, as denoted above, runs from $+\varepsilon$ to $-\varepsilon$ relative to the horizontal where $\varepsilon = \text{Arccos}\,(c_s/c_m)$. Here c_s is the sound speed at the source and c_m is the maximum sound speed along the profile. Within the range ε to $-\varepsilon$ rays (particles) are started equally spacedin angle. Thus, the cosine of the J^{th} particle relative to the vertical axis, C(J) , is

$$C(J) = \cos\,(ARG) \tag{2.31}$$

where

$$ARG = \left[(90 - \varepsilon) + \frac{2J\varepsilon}{N}\right]\frac{\pi}{180} \tag{2.32}$$

and N is the total number of particles considered. Usually 3000 to 5000 particles are used.

(b) Particle Tracking

As a result of the source sampling each particle begins its trajectory characterized by several parameters. These are

X = range coordinate = R
Z = depth coordinate
A = cosine of trajectory relative to horizontal
C = cosine of trajectory relative to vertical
KI = K index of zone in which the particle is located
LI = L index of zone in which the particle is located
EN = weight of the particle
IE = flag denoting which of the four sides of a zone was last crossed.

Each zone in the mesh is labeled with two integers K,L as shown in Figure 2.3 and A is obtained from C as $A = \sqrt{1-C^2}$. A is assumed to be positive since, consistent with the parabolic equation approximation, we allow no backward reflected energy.

Referring to Figure 2.5 we have a particle entering zone 0, in which the gradient of the index of refraction is $\left(\partial n/\partial z\right)_o$, at point $\left(R_o,Z_o\right)$. Knowing that the trajectory in zone 0 is a circle of radius $r_o = 1/(\partial n/\partial z)_o$ allows a determination of the center of curvature, $\left(R_c^o,Z_c^o\right)$, to be made. The equation of the circle describing the trajectory is then solved simultaneously with the equation for each zone 0 boundary. After the intersection points of the circle with each of the four sides are known, the distances from $\left(R_o,Z_o\right)$ to each of these points can be calculated. The shortest distance to boundary (SDB) is then

$$SDB = Min\left[S_1^{(1)},\ S_1^{(2)},\ S_2^{(1)},\ S_2^{(2)},\ S_3^{(1)},\ S_3^{(2)},\ S_4^{(1)},\ S_4^{(2)}\right] \quad ,$$

where $S_i^{(1)}$, $S_i^{(2)}$ are the distances to the two points where the circle crosses the i^{th} side. If any $S_i^{(1)}$, $S_i^{(2)}$ is less than 10^{-6} it is set to 10^{10}. This avoids counting the point where the particle just crossed the boundary ($S_i = 0$) as the SDB. After the particle crosses side 1 (see Figure 2.5) its new direction cosines are calculated and its new center of curvature $\left(R_c^1,Z_c^1\right)$ is determined using the new value of $(\partial n/\partial z)_1$. The new radius of curvature is $r_1 = 1/(\partial n/\partial z)_1$. This procedure continues until the particle either exits the mesh at the maximum range of interest or is assumed to be absorbed in the bottom because its trajectory crosses a bottom segment.

(c) Scattering

In the process of tracking the particle through the mesh it could either scatter from the surface or from internal waves. If a flat surface is assumed then specular reflection obtains and at the surface the C direction cosine merely becomes -C. A rough surface results in the reflected ray coming off with some probability distribution $f(\theta_i,\theta)$ which is a function of the incident angle, θ_i , as well as the exit angle. The details of the surface scattering probability functions will be covered in the next section.

After calculating the distances to the various zone boundaries, as discussed above, the next step is to determine the distance to scattering. The scattering here is volume scattering and internal waves are assumed to be the scattering mechanism. The distance to scattering is obtained using the results of Eq. (2.16),

$$S_{sc} = -\frac{1}{\sigma_s} \ell n\ \xi, \tag{2.33}$$

where σ_s is the scattering cross section and ξ is a random number. If

$$S_{sc} > SDB$$

the particle is advanced to the appropriate boundary as discussed before. On the other hand, if

$$S_{sc} < SDB$$

a scattering takes place before reaching the nearest boundary. In this case the particle is advanced along its trajectory a distance S_{sc} to the scattering point. Here the new direction cosines are determined from the scattering probability distribution function $g(\theta,\theta')$, where θ' is the angle relative to the horizontal after scattering. Given the new angle θ' and gradient of n, $\partial n/\partial z$, the new center of curvature, (R_c^N, Z_c^N) can be found. Since the particle has not changed zones, the radius of curvature remains unchanged. With these new conditions an updated trajectory circle is obtained and the process continues as before.

The details of the internal wave scattering kernel will also be discussed in the next section.

(d) Transmission Loss Calculation

To calculate transmission loss we use a method based on the path-length estimator discussed in Section 2.3.2(c) in which every

particle which passes through a zone contributes to the tally in that zone.

Consider the average weight of the i^{th} particle in zone (K,L):

$$\bar{\varepsilon}_i(K,L) = \int_0^{s_i} \varepsilon_0^i \, e^{-\sigma_a s'} \, ds'/c\Delta t \qquad (2.34)$$

where

ε_0^i = weight of the particle upon entering zone (K,L)

σ_a = absorption coefficient in zone (K,L)

s_i = distance travelled in zone (K,L)

c = velocity of sound in zone (K,L)

Δt = time step.

The quantities c and Δt will eventually drop out of our expressions.

If we assume $\sigma_a s_i << 1$, which is always valid for the σ_a's and zoning sizes which we use, then

$$\bar{\varepsilon}_i(K,L) = \frac{\varepsilon_0^i \, s_i}{c\Delta t} \quad . \qquad (2.35)$$

Averaging this over the volume of the zone gives

$$\bar{\varepsilon}_i^V(K,L) = \frac{\bar{\varepsilon}_i(K,L)}{VOL(K,L)}$$

$$= \frac{\varepsilon_0^i \, s_i}{c\Delta t \; \frac{1}{2}(R_1+R_2)\Delta R \Delta Z \Delta\phi} \quad . \qquad (2.36)$$

Here R_1 and R_2 are the two R values which bound the zone, $\Delta Z = Z_2 - Z_1$ is the depth thickness of the zone and $\Delta R = R_2 - R_1$ and $\Delta\phi$ is the azimuthal angle increment.

Now, at a reference range of r_r, select a small volume of thickness s_r; then the reference volume is

$$V_r = s_r r_r^2 \sin\theta d\theta d\phi \quad \text{(see Figure 2.6)}$$

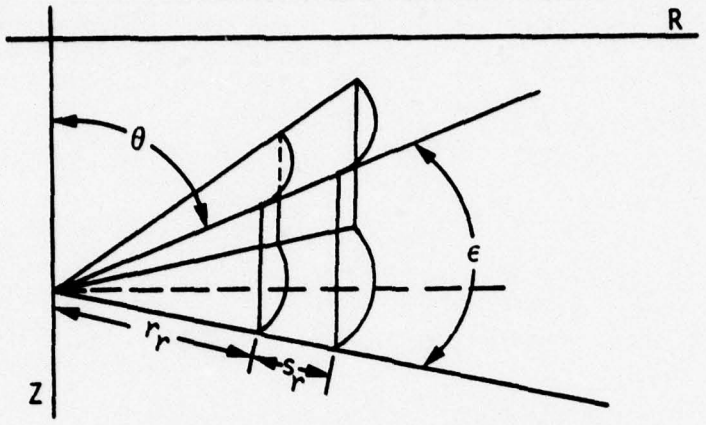

Figure 2.6. Schematic of Small Volume Element at Radius r_r.

or

$$V_r = 2r_r^2 s_r \sin\varepsilon \, \Delta\phi \quad . \tag{2.37}$$

Hence

$$\bar{\varepsilon}_{ref} = \frac{E s_r}{c\Delta t V_r} \tag{2.38}$$

and the transmission loss becomes (in decibels)

$$N(K,L) = 10 \log_{10} \frac{\bar{\varepsilon}_{K,L}}{\bar{\varepsilon}_{ref}}$$

$$= 10 \log_{10} \left[\frac{\sum_i \varepsilon_0^i s_i (2 \sin\varepsilon) r_r^2}{\frac{1}{2}\Delta R \Delta Z (R_1 + R_2) E} \right] \tag{2.39}$$

where the sum is over all particles which pass through zone K,L and E is the total weight emitted through the reference volume. If R and Z are measured in kilometers and the dB loss is reference 1 meter then $r_r = 10^{-3}$.

The final step is to assign error bars to the values of N and this is done as discussed in Section 2.3.3.

3. SCATTERING MODELS

In this section we discuss the various scattering models, both surface and internal wave, that were incorporated into the ACTOR code. For surface scattering these include the phase screen model and the sawtooth mode. The sinusoidal model was studied but was not put into the code because it appeared to differ only slightly from the sawtooth model at least as far as the average scattering angle and variance are concerned. This will be discussed more fully in Section 3.1.3. The phase screen model is developed in Section 3.1.1. We attempted to use this model in conjunction with the Pierson-Moskowitz[24] spectrum for fully developed seas; however, the sea state which obtained during the experiment, the results of which we were attempting to calculate, were such (extremely calm sea) that it did not apply. Therefore, we proceeded to develop the sawtooth model which was used although we also included in ACTOR the coding necessary to apply the phase screen model should it be needed at some future time.

The internal wave scattering models are discussed in Section 3.2. First we explain how the results of the Garrett-Munk[8,9] model are incorporated into the ACTOR code. This is done in Sections 3.2.1 and 3.2.2. We also briefly describe another model, the Gaussian model, in Section 3.2.3.

3.1 SCATTERING BY ROUGH SURFACES

3.1.1 The Phase-Screen Approximation

As pointed out by Schnieder,[25] the treatment of scattering by non-periodic rough boundaries in the Monte Carlo method cannot be done by direct simulation. The reason is that the propagation distance scales are so large compared with correlation distance associated with the typical rough ocean surface. Therefore, we simulate instead the average scattering "transfer function" which takes the incident ray with angle θ_o to the

exit ray with angle θ (see Figure 3.1) for the random rough surface described by the random function $\xi(r)$. We use the convention that upward going rays have negative angles and downward rays have positive angles; thus $\theta_o < 0$ and $\theta > 0$. The needed relation is

$$f(0,\theta,r) = \int_{-\infty}^{0} G(\theta,\theta_o) f(0,\theta_o,r) d\theta_o \qquad (3.1)$$

which holds for $0 < \theta < \infty$.

For a plane wave incident at angle θ_o the corresponding incident pressure is

$$P_{inc} = e^{ik(r\cos\theta_o - Z\sin\theta_o)} \quad . \qquad (3.2)$$

Using the phase screen approximation, near $Z = 0$ the scattered wave is given by

$$P_{sc} = -e^{ik(r\cos\theta_o + Z\sin\theta_o)} e^{i\phi(r)} \quad . \qquad (3.3)$$

The total pressure field is

$$P = P_{inc} + P_{sc} \qquad (3.4)$$

and the surface boundary condition is

$$P[r,\xi(r)] = 0$$

from which it follows that

$$\phi(r) = -2k\xi(r)\sin\theta_o \quad . \qquad (3.5)$$

The scattered field at $Z = 0$ therefore is

$$P_{sc}(o,r) = -e^{ik[r\cos\theta_o - 2\xi(r)\sin\theta_o]} \quad . \qquad (3.6)$$

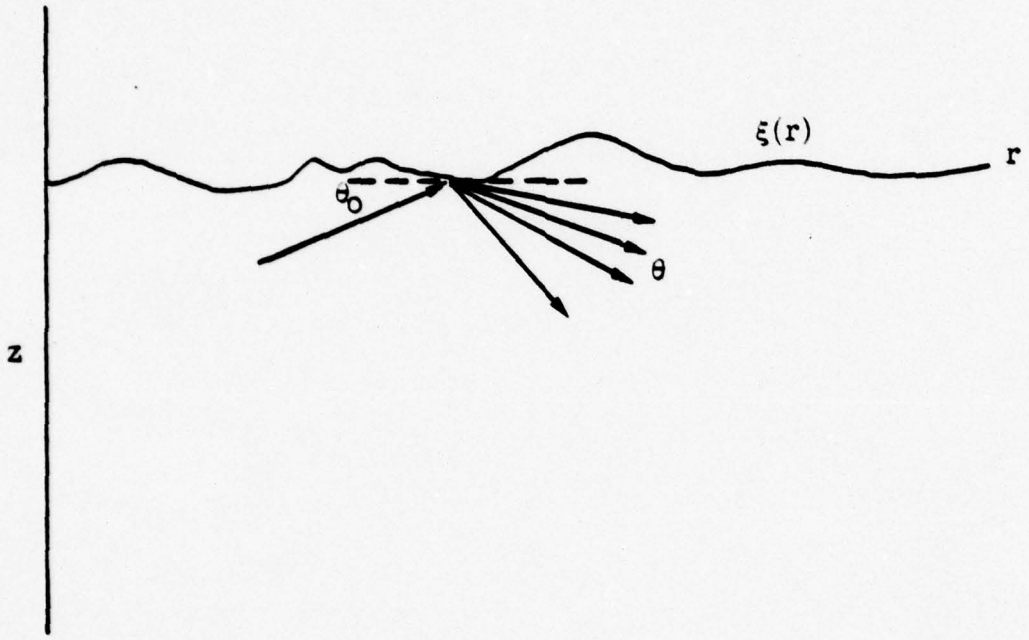

Figure 3.1. Schematic of Rough Surface Scattering.

In the parabolic (small angle) approximation we write this as

$$P_{sc}(o,r) = \psi(o,r)e^{ikr} \tag{3.7}$$

and

$$\psi(o,r) = - e^{i\Phi(r)} \tag{3.8}$$

$$\Phi(r) = kr(\cos\theta_o - 1) - 2k\xi(r)\sin\theta_o \approx - \tfrac{1}{2}kr\theta_o^2 - 2k\xi(r)\theta_o \quad . \tag{3.9}$$

Using the Wigner function to calculate the transition probability $G(\theta,\theta_o)$ we get

$$G(\theta,\theta_o) = \frac{k\theta_o}{2\pi}\int_{-\infty}^{\infty} dy\ e^{-\frac{1}{2}ik\theta^2 y}\langle\psi(r - \tfrac{1}{2}y)\psi^*(r + \tfrac{1}{2}y)\rangle \quad . \tag{3.10}$$

For a surface with statistical properties given by

$$\left.\begin{aligned} \langle\xi^2(r)\rangle &= h^2 \\ \langle\xi(r + \tfrac{1}{2}y)\xi(r - \tfrac{1}{2}y)\rangle &= h^2\rho(y),\ \rho(0) = 1 \end{aligned}\right\} \tag{3.11}$$

and assuming $\xi(r)$ is Gaussian we get

$$G(\theta,\theta_o) = \frac{k\theta_o}{2\pi}\int_{-\infty}^{\infty} dy\ e^{-ik\theta_o(\theta + \theta_o)y}\ e^{-4k^2\theta_o^2h^2[1 - \rho(y)]} \quad . \tag{3.12}$$

This is the basic formula which gives G as a function of the correlation function of the surface fluctuations, $\rho(y)$. Note that

$$\int G(\theta,\theta_o)d\theta = 1 \quad . \tag{3.13}$$

Two limits can now be investigated based on the Rayleigh parameter, $R = 2kh\theta_o$. The cases $R << 1$ and $R >> 1$ will be considered and then combined into a single interpolation equation.

For $R \gg 1$ we use

$$e^{-4k^2\theta_o^2h^2[1 - \rho(y)]} \approx e^{-2k^2\theta_o^2h^2y^2/L^2} \tag{3.14}$$

where

$$\frac{1}{L^2} = -\left.\frac{d^2\rho}{dy^2}\right|_{y = 0} . \tag{3.15}$$

The quantity L is called the correlation length of the random surface. The rms slope is given by

$$\left\langle\left(\frac{d\xi}{dr}\right)^2\right\rangle^{\frac{1}{2}} = \frac{h}{L} . \tag{3.16}$$

We then obtain

$$G(\theta,\theta_o) = \frac{L}{2h\sqrt{2\pi}} e^{-(\theta + \theta_o)^2L^2/8h^2} . \tag{3.17}$$

The rms angle of scatter is found to be

$$\left\langle(\Delta\theta)^2\right\rangle^{\frac{1}{2}} = \frac{2h}{L} \ll 1 . \tag{3.18}$$

In the opposite case $R \ll 1$ and we obtain, skipping some algebra,

$$G(\theta,\theta_o) = (1 - 4k^2\theta_o^2h^2)\delta(\theta + \theta_o) + D(\theta,\theta_o) \tag{3.19}$$

where

$$D(\theta,\theta_o) = 4k^2\theta_o^2h^2 \frac{k\theta_o}{2\pi} \int_{-\infty}^{\infty} e^{-ik\theta_o(\theta + \theta_o)y} \rho(y)dy . \tag{3.20}$$

The first term on the right in Eq. (3.19) is the specular term and the second is the diffuse scatter term. As an example take

$$\rho(y) = e^{-y^2/2L^2} \quad . \tag{3.21}$$

Then

$$D(\theta + \theta_o) = 4k^2h^2\theta_o^2 \frac{kL\theta_o}{\sqrt{2\pi}} e^{-k^2L^2\theta_o^2(\theta + \theta_o)^2/2} \quad . \tag{3.22}$$

The width of the diffuse scatter angular spectrum is now

$$\langle(\Delta\theta)^2\rangle^{\frac{1}{2}} = \frac{1}{kL\theta_o} \quad . \tag{3.23}$$

Both of these results can be consolidated into a single formula by interpolation. We get

$$G(\theta,\theta_o) = S(\theta_o)\delta(\theta + \theta_o) + D(\theta,\theta_o) \tag{3.24}$$

where the specular component is given by

$$S(\theta_o) = e^{-4k^2h^2\theta_o^2} \tag{3.25}$$

and the diffuse component is given by

$$D(\theta,\theta_o) = \left(1 - e^{-4k^2h^2\theta_o^2}\right)\frac{1}{\sqrt{2\pi\sigma^2}} e^{-(\theta + \theta_o)^2/2\sigma^2} \tag{3.26}$$

where

$$\sigma^2 = \frac{1}{k^2L^2\theta_o^2} + \frac{4h^2}{L^2} \quad . \tag{3.27}$$

We can now check both limits. When $2kh\theta_o >> 1$ the specular component vanishes, $\sigma^2 = 4h^2/L^2$, and $D(\theta,\theta_o)$ reduces to the previous expression. On the other hand, when $2kh\theta_o << 1$ the specular component dominates and we have $\sigma^2 = 1/k^2L^2\theta_o^2$. Again we recover the previous result.

Equation (3.24) is sampled statistically in such a way as to on the average reproduce the angular distribution implied by the expressions for $S(\theta_o)$ and $D(\theta,\theta_o)$.

To understand why the phase screen method fails when used in conjunction with the Pierson-Moskowitz spectrum for the sea state (wind speed) conditions which were observed during the experiment, consider the following.

If $\xi(x)$ *is the wave height, let*

$$h^2 = \langle \xi^2(x) \rangle \quad ; \tag{3.28}$$

then from Reference 24

$$h^2 = \frac{\alpha u^4}{4\beta g^2} \quad , \tag{3.29}$$

where α and β are two dimensionless constants

$$\alpha = 8.1\ (10^{-3}) \quad ,$$

$$\beta = 0.74 \quad ,$$

u is the windspeed and g is the gravitational constant (9.75 m/sec^2). The correlation length, L, is then given by

$$L = \frac{h}{\langle s^2 \rangle^{\frac{1}{2}}} \tag{3.30}$$

where the average slope squared is

$$\langle s^2 \rangle = \alpha\ \ell n\ \frac{k_c^2\, u^4}{\beta g^2} \tag{3.31}$$

Here k_c is a cut-off wave number in the Pierson-Moskowitz spectrum. One way to determine k_c is to consider the Cox and Munk[26] expression for the average slope squared,

$$S_o^2 = (5.12 \times 10^{-5}\ u \pm .004)$$

where u is the windspeed in cm/sec. At $u = 500$ cm/sec $S_o^2 = 0.0256 \pm .004$. Taking S_o^2 as 0.0256 we get

$$0.0256 = 8.1\ (10^{-3})\ \ell n\left(\frac{k_c^2\ 625}{0.74\ (9.75)^2}\right)$$

or

$$k_c = 1.63\ m^{-1}\ .$$

So,

$$\langle s^2\rangle = 8.1\ (10^{-3})\ell n(0.038\ u^4) \quad . \qquad (3.32)$$

For consistency we check this with the maximum value of $\langle s^2\rangle$ which is taken to be 0.082 inferred from Kinsman[27] who claims $S_{max} = 2/7$ as the theoretical upper limit to S. Since the Pierson-Moskowitz spectrum applies to fully developed seas with wind speeds of 20-40 knots (10-20 m/sec) we would hope that when $u = 20$ m/sec is substituted into Eq. (3.32) that we would get $\langle s^2\rangle \cong 0.082$. Doing this gives

$$\max\langle s^2\rangle = 8.1\ (10^{-3})\ell n\ 0.038\ (20)^4$$
$$= 0.071$$

which is reasonably close to 0.082.

Now consider the results for h^2 and $\langle s^2\rangle$ under the experimental conditions of $u \cong 4$ m/sec. We get from Eq. (3.29)

$$h^2 = 0.0074 \quad ,$$

and $\langle s^2 \rangle = 0.0184$ from Eq. (3.32).

For the surface duct in which the measurements were made the largest angle of incidence, θ_o , at the surface was about 3^o or 0.053 radians. The Rayleigh parameter for 1000 Hz sound thus becomes

$$R = 2kh\theta_o$$

$$\cong 0.038$$

where k is the acoustic wavenumber $\cong 4.2\ m^{-1}$. Since the Rayleigh parameter is very small we have almost total specular reflection. The real trouble arises, however, in the angular distribution of the diffuse component the width of which is given by Eq. (3.23)

$$\langle (\Delta\theta)^2 \rangle^{1/2} = \frac{1}{kL\theta_o}$$

where

$$L = h/\langle s^2 \rangle^{1/2} \quad . \tag{3.33}$$

With our parameters this becomes

$$\langle (\Delta\theta)^2 \rangle^{1/2} = 7.13 \text{ radians} \quad .$$

Since this is obviously a nonphysical result, we can only assume that the scattering at the acoustic frequencies of about 1000 Hz or less is specular and takes place from facets which result from the swell component. This conclusion is what led us to develop the sawtooth model discussed next.

3.1.2 *The Sawtooth Model*

Even in the simple sawtooth model the actual details involved in working out the scattering angle for all cases are very extensive. Therefore, we will only outline the method and provide the results for the various situations that can arise when an acoustical "packet" or ray specularly scatters from a sawtooth surface profile. Thus we assume a surface wave of the form shown in Figure 3.2,

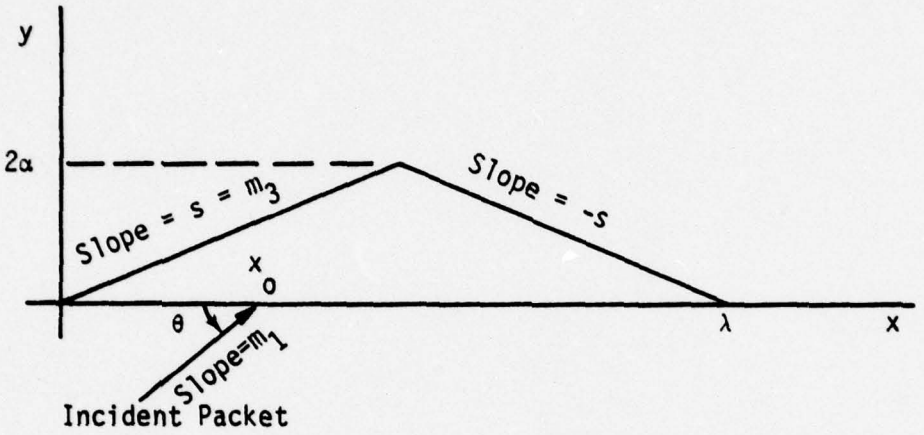

Figure 3.2. Schematic of Sawtooth Surface Wave.

where

$$S = 4\alpha/\lambda \quad . \tag{3.34}$$

Geometrical considerations show that a ray of incident slope m_1 specularly reflecting from a surface with slope m_3 will exit from the reflection with slope m_2 given by

$$m_2 = \frac{2m_3 - m_1 (1 - m_3^2)}{1 + 2m_1 m_3 - m_3^2} \quad . \tag{3.35}$$

If we assume

$$|m_1| << 1 \quad ; \quad |m_3| << 1 \quad , \tag{3.36}$$

i.e., small angles of incidence and shallow waves, then Eq. (3.35) becomes

$$m_2 \cong 2m_3 - m_1 \quad . \tag{3.37}$$

We assume the packet intersects the x-axis at $x_o (0 \leq x \leq \lambda)$, and at an angle θ $(0 \leq \theta \leq \pi/2)$ corresponding to a slope m_1 $(0 \leq m_1 < \infty)$. We need to distinguish several cases.

Case I, $x_o > \lambda/2$

This is the case shown in Figure 3.3.

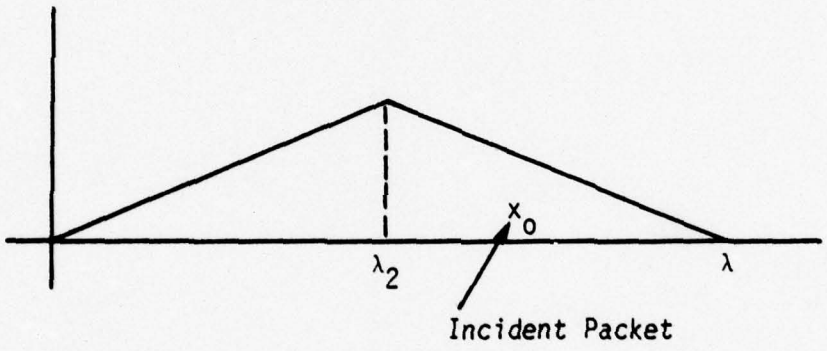

Figure 3.3. Geometry of the Case Where $x_o > \lambda/2$.

In this case the packet always hits the right half of the wave (for any positive m_1) and, with $m_3 = -S$ in Eq. (3.37),

$$m_2 = -(2S + m_1) \quad . \tag{3.38}$$

This equation shows that the slope of the reflected packet is always negative, no matter what m_1 is, and hence the scattered packet does not interact anymore with the wave, i.e., we have single scattering. It

is important to note that this is a consequence of assuming small angles ($S << 1$ and $m_1 << 1$). To see this let us consider the general reflection formula, Eq. (3.35). If the incident slope were given by

$$m_1 = \frac{2S}{S^2 - 1} \quad , \tag{3.39}$$

then Eq. (3.35) predicts $m_2 = 0$ and the reflected packet would travel horizontally to the left and hit the left side of the wave, resulting in multiple scattering. But for $S << 1$, Eq. (3.39) has no solution since we restrict m_1 to be positive as well as S.

Case II, $x_0 < \lambda/2$

This is the situation shown in Figure 3.4.

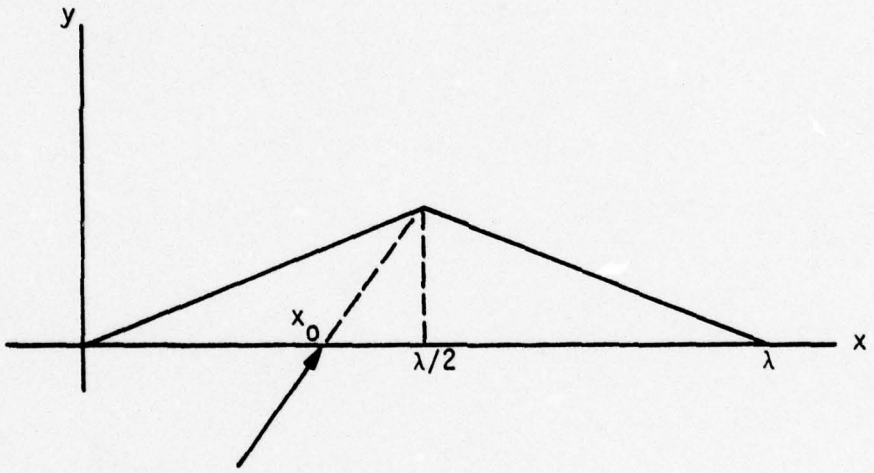

Figure 3.4. Geometry of the Case Where $x_0 < \lambda/2$.

Here there are two subcases. Depending on m_1 , the packet may hit either the right half of the wave or the left half. Figure 3.4 shows the "cross-over" value of m_1. For m_1 less than that shown, the packet hits the right half; for m_1 greater than that shown, it hits the left half.

Given x_o , let us compute the critical value of m_1 , which we call m_1^*. The wave surface is

$$y = Sx \tag{3.40}$$

and the packet trajectory is

$$y = m_1 (x - x_o) \quad . \tag{3.41}$$

Demanding that these lines intersect at $x = \lambda/2$ leads to the result

$$m_1^* = \left(\frac{\lambda}{\lambda - 2x_o}\right) S \quad . \tag{3.42}$$

Case II-A, $x_o < \lambda/2$, $m_1 < m_1^*$

Here the packet hits the right half of the wave and, from Eq. (3.37),

$$m_2 = - (2S + m_1) \tag{3.43}$$

and we have single scattering.

Case II-B, $x_o < \lambda/2$, $m_1 > m_1^*$

In this case the packet hits the left half of the wave and Eq. (3.37) gives

$$m_2 = 2S - m_1 \quad . \tag{3.44}$$

The question now is: Does this reflected packet hit the right side of the wave and have a second scattering? The algebra involved in answering this question is lengthy and will be omitted. The result is essentially that there are several subcases.

Case II-B-1, $\lambda/3 \leq x_o \leq \lambda/2$, $m_1 > m_1^*$

In this case there is no second scattering from the right side of the wave.

Case II-B-2, $0 \leq x_o \leq \lambda/3$, $m_1 > m_1^*$

Here we find two subcases.

Case II-B-2a, $0 \leq x_o \leq \lambda/3$, $\bar{m}_1 \leq m_1 < \infty$

Here

$$m_1 = \left(\frac{2\lambda}{x - x_o}\right)s \tag{3.45}$$

and in this case there is no second scattering.

Case II-B-2b, $0 \leq x_o \leq \lambda/3$, $m_1^* \leq m_1 \leq \bar{m}_1$

In this case we get a second scattering. Call the slope of the path following the second scattering m_4. From Eq. (3.44), m (incident on right half of wave) = $2S - m_1$, and thus from Eq. (3.37)

$$m_4 = -2S - (2S - m_1)$$

$$= -4S + m_1 \quad . \tag{3.46}$$

The largest possible value of m_4 is

$$(m_4)_{max} = -S\left(\frac{2\lambda - 4x_o}{\lambda - x_o}\right) \tag{3.47}$$

and since $0 \leq x_o \leq \lambda/3$ we have

$$(m_4)_{max} < 0 \quad .$$

Thus, this second-reflected packet cannot go back and hit the left half of the wave again. Hence a third scattering is not possible.

Let us summarize our results. Let m_i be the slope of the incident packet (previously called m_1), let m_r be the negative of the slope of the scattered (once or twice) packet and S is the slope of the sawtooth wave. If we define the incident angle

$$\theta = \tan^{-1} m_i \tag{3.48}$$

and the reflected angle

$$\phi = \tan^{-1} m_r \tag{3.49}$$

we have the picture shown in Figure 3.5.

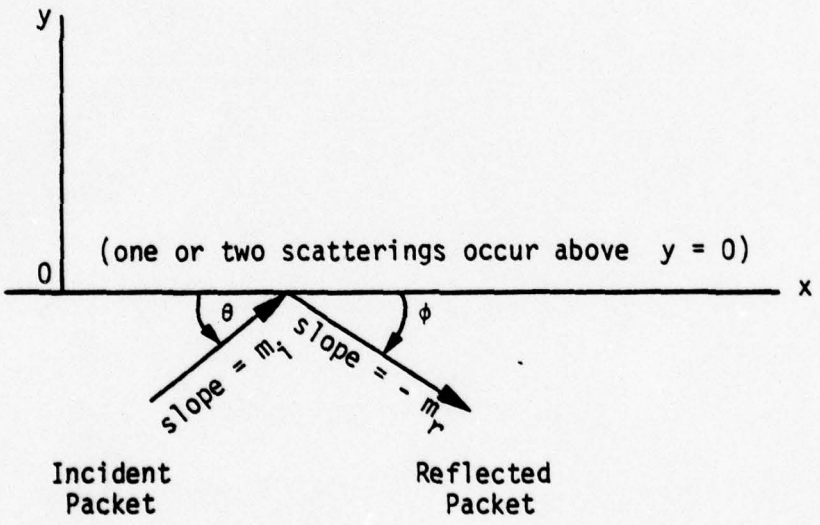

Figure 3.5. Schematic of Incident and Final Angles.

With this picture we then have

$\underline{0 \leq x_o \leq \lambda/3}$

$$m_r = m_i + 2S \quad , \quad 0 \leq m_i \leq \left(\frac{\lambda}{\lambda - 2x_o}\right)S$$

$$m_r = 4S - m_i \quad , \quad \left(\frac{\lambda}{\lambda - 2x_o}\right)S \leq m_i \leq \left(\frac{2\lambda}{\lambda - x_o}\right)S$$

$$m_r = m_i - 2S \quad , \quad \left(\frac{2\lambda}{\lambda - x_o}\right)S \leq m_i \leq \infty$$

$\underline{\lambda/3 \leq x_o \leq \lambda/2}$

$$m_r = m_i + 2S \quad , \quad 0 \leq m_i \leq \left(\frac{\lambda}{\lambda - 2x_o}\right)S$$

$$m_r = m_i - 2S \quad , \quad \left(\frac{\lambda}{\lambda - 2x_o}\right)S \leq m_i < \infty$$

$\underline{\lambda/2 \leq x_o \leq \lambda}$

$$m_r = m_i + 2S \quad , \quad 0 \leq m_i < \infty$$

We now assume that the phase of the surface wave is completely random at the time of first scattering (and that the wave is stationary until the packet has left the scattering region). We want to ensemble average our results over all possible phases, or equivalently over x_o. Thus

$$\bar{m}_r = \frac{1}{\lambda} \int_0^{\lambda} dx_o \, m_r \quad . \tag{3.50}$$

To compute the variance we will also need

$$\overline{m_r^2} = \frac{1}{\lambda} \int_0^{\lambda} dx_o \, m_r^2 \quad . \tag{3.51}$$

The algebraic details of these calculations will be omitted and only the results presented. For $\overline{m_r}$ we have

$\underline{m_i \leq S}$

$$\overline{m}_r = m_i + 2S \tag{3.52}$$

$\underline{S \leq m_i \leq 2S}$

$$\overline{m}_r = 4S - \frac{S^2}{m_i} \tag{3.53}$$

$\underline{2S \leq m_i \leq 3S}$

$$\overline{m}_r = 2m_i - 6S + 11 \frac{S^2}{m_i} \tag{3.54}$$

$\underline{m_i \geq 3S}$

$$\overline{m}_r = m_i + \frac{2S^2}{m_i} \quad . \tag{3.55}$$

In Table 3.1 we have listed several values of $Z = \overline{m}_r/S$ for various values of $\xi = m_i/S$. A corresponding plot is given in Figure 3.6.

For $\overline{m_r^2}$ we get

$\underline{m_i \leq S}$

$$\overline{m_r^2} = (m_i + 2S)^2 \tag{3.56}$$

Table 3.1. Mean Value of Reflection Tangent Versus Incident Tangent.

Functional Form	$\xi \equiv m_i/S$	$\xi \equiv \bar{m}_r/S$
$Z = \xi + 2$	0.0	2.00
$Z = 4 - \frac{1}{\xi}$	1.0	3.00
	1.2	3.17
	1.4	3.29
	1.6	3.38
	1.8	3.44
$Z = 2\xi - 6 + \frac{11}{\xi}$	2.0	3.50
	2.2	3.40
	2.4	3.38
	2.6	3.43
	2.8	3.53
$Z = \xi + \frac{2}{3}$	3.0	3.67
	3.4	3.99
	3.8	4.33
	4.4	4.85
	5.0	5.40
	5.6	5.96
	6.2	6.52
	7.0	7.29
	8.0	8.23
	9.0	9.22
	10.0	10.10

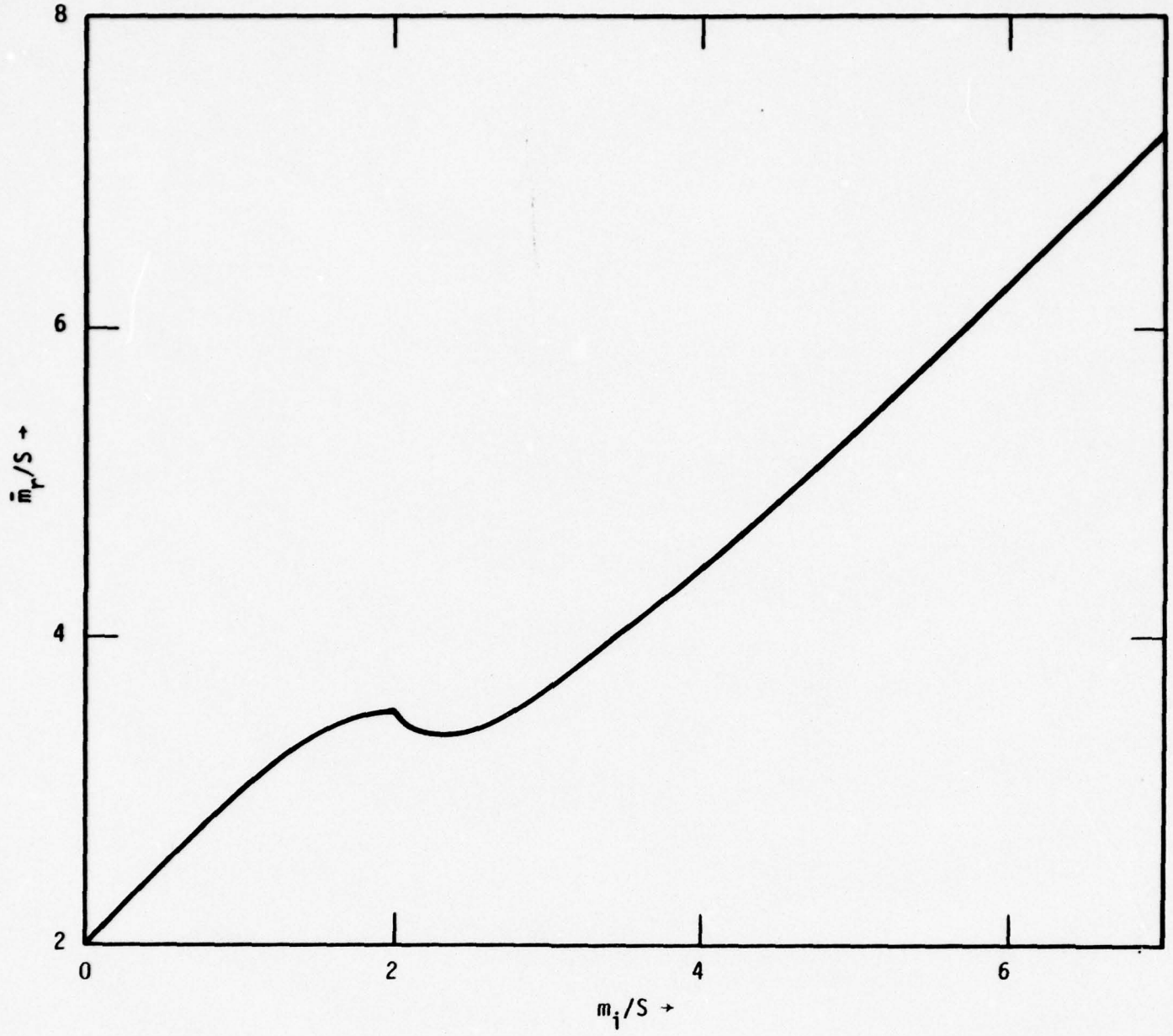

Figure 3.6. Mean Value of Reflection Tangent $\bar{m}_r$ Versus Incident Tangent m_i ($S = 4\alpha/\lambda$).

$S \leq m_i \leq 2S$

$$\overline{m_r^2} = m_i^2 - 2m_i S + 16S^2 - 6\frac{S^3}{m_i} \tag{3.57}$$

$2S \leq m_i \leq 3S$

$$\overline{m_r^2} = m_i^2 + 2m_i S - 4S^2 + 18\frac{S^3}{m_i} \tag{3.58}$$

$m_i \geq 3S$

$$\overline{m_r^2} = m_i^2 + 8S^2 \quad . \tag{3.59}$$

Defining a variance, σ^2 , as

$$\sigma^2 \equiv \overline{m_r^2} - (\overline{m}_r)^2 \tag{3.60}$$

we get

$m_i \leq S$

$$\sigma^2 = 0 \tag{3.61}$$

$S \leq m_i \leq 2S$

$$\sigma^2 = m_i^2 \left(1 - \frac{S}{m_i}\right)^3 \left(1 + \frac{S}{m_i}\right) \tag{3.62}$$

$2S \leq m_i \leq 3S$

$$\sigma^2 = -3m_i^2 + 26m_i S - 84S^2 + 150\frac{S^3}{m_i} - 121\frac{S^4}{m_i^2} \tag{3.63}$$

$\underline{m_i \geq 3S}$

$$\sigma^2 = 4S^2 \left(1 - \frac{S^2}{m_i^2}\right) \quad . \tag{3.64}$$

Note from this equation that as S goes to zero so does σ^2, as it should.

In Table 3.2 we tabulate values of $Z = \sigma^2/S^2$ for various values of $\xi = m_i/S$ with a corresponding plot given in Figure 3.7.

The results just obtained are used in the ACTOR code by fitting to a Gaussian. For a given incident angle θ with tangent m_i we obtain m_r by sampling from

$$P(m_r) = \frac{1}{\sqrt{2\pi}\,\sigma} \exp\left[-\frac{(m_r - \bar{m}_r)^2}{2\sigma^2}\right] \quad . \tag{3.65}$$

3.1.3 The Sinusoidal Model

For the swell component of surface roughness we used the sawtooth model in our calculations. We recognized at the outset that this was only an approximation to the more realistic sinusoidal character of swell. An attempt was made to calculate the scattering angle as a function of x_o and m_i for the sinusoidal model as was done for the sawtooth model. This turned out to be analytically impossible. By ignoring second scattering, however, we were able to obtain analytic solutions for the moments of m_r in the no-shadowing region. In the shadowing region, again ignoring second scattering, these moments were obtained numerically.

The no-shadowing case is depicted in Figure 3.8. This is the case where

$$m_i > 2\pi \frac{\alpha}{\lambda} \tag{3.66}$$

Table 3.2. Variance of Reflection Tangent Versus Incident Tangent.

Functional Form	$\xi \equiv m_1/S$	$Z \equiv \sigma^2/S^2$
$Z = 0$	0.0	0.000
	1.0	0.000
$Z = \xi^2 \left(1 - \frac{1}{\xi}\right)^3 \left(1 + \frac{1}{\xi}\right)$	1.2	0.012
	1.4	0.078
	1.6	0.219
	1.8	0.442
	2.0	0.750
$Z + - 3\xi^2 + 26\xi - 84 + \frac{150}{\xi} - \frac{121}{\xi^2}$	2.2	1.862
	2.4	2.613
	2.6	3.113
	2.8	3.418
	3.0	3.556
$Z + 4^{\cdot}\left(1 - \frac{1}{\xi^2}\right)$	3.4	3.654
	3.8	3.723
	4.4	3.793
	5.0	3.840
	5.6	3.872
	6.2	3.896
	7.0	3.918
	8.0	3.938
	9.0	3.951
	10.0	3.960

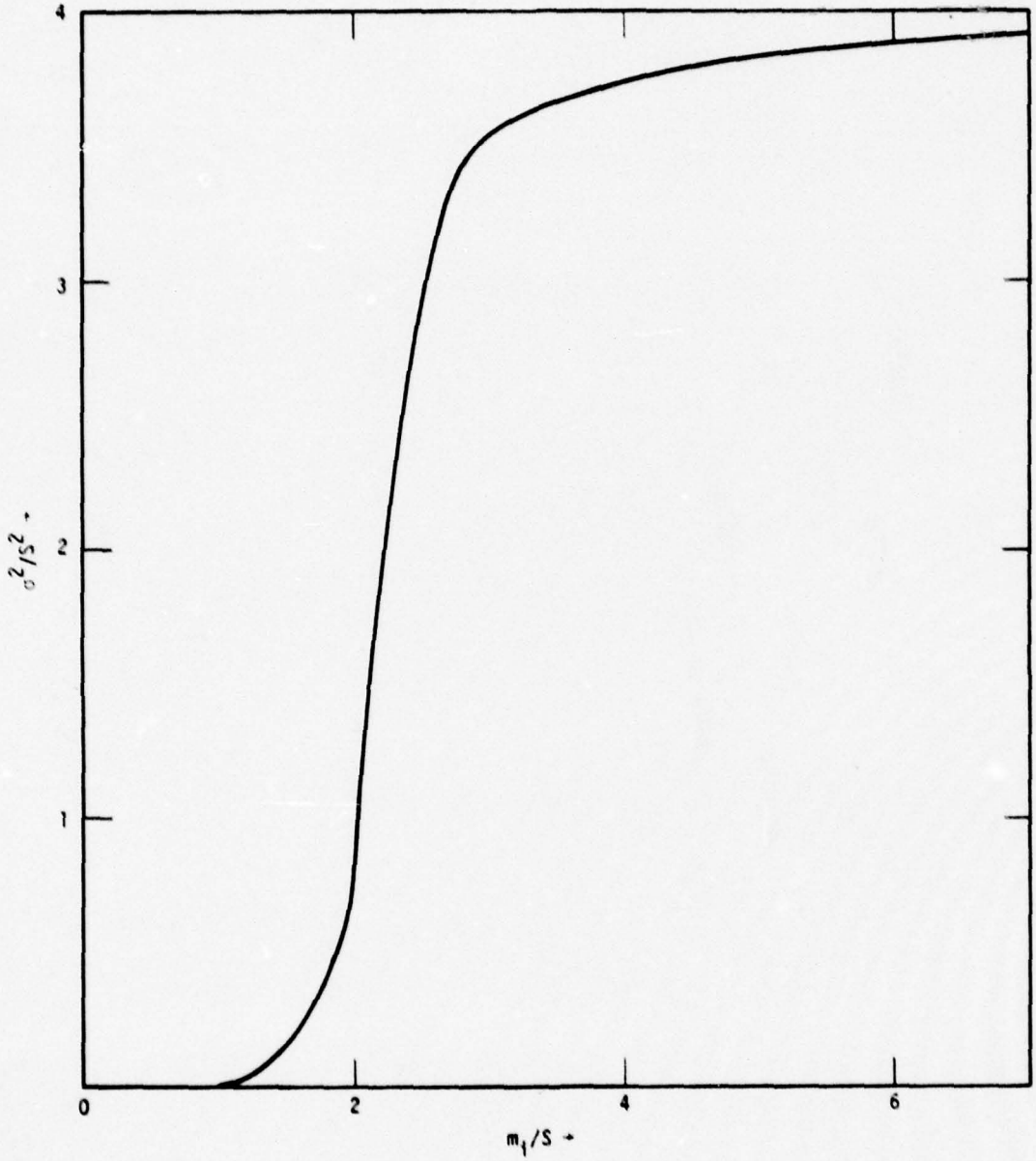

Figure 3.7. Variance of Reflection Tangent σ^2 Versus Incident Tangent m_i ($S = 4\alpha/\lambda$).

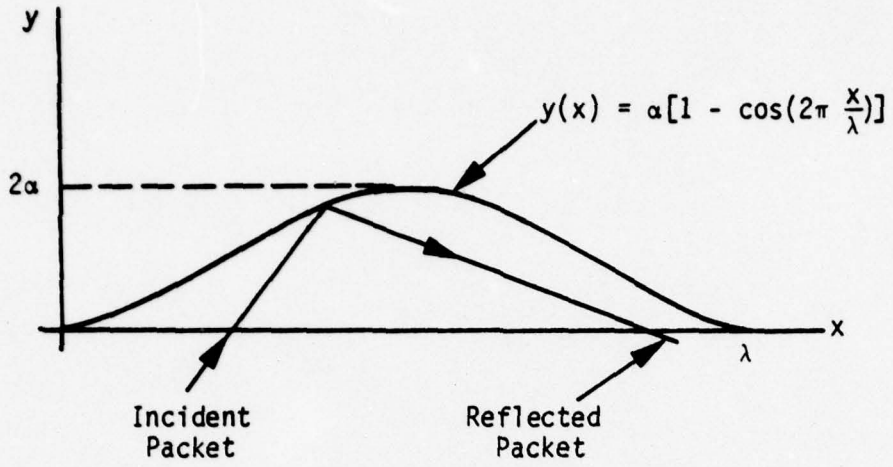

Figure 3.8. Geometry of No-Shadowing Case.

and if we use the same definition of S as in the sawtooth model ($S = 4\alpha/\lambda$) we have

$$m_i > \frac{\pi}{2} S \quad . \tag{3.67}$$

We will not present any details for the sinusoidal model but will only list the results. For the no-shadowing region with no second scattering the first moment and variance become

$$\bar{m}_r = m_i + \frac{\pi^2}{4} \frac{S^2}{m_i} \tag{3.68}$$

$$\sigma^2 = \frac{\pi^2}{2} S^2 \left[1 - \frac{\pi^2}{8} \frac{S^2}{m_i^2} \right] \quad . \tag{3.69}$$

The case of the onset of shadowing is shown in Figure 3.9. For x_o values smaller than that shown, shadowing becomes important and results for the first two moments of m_r were obtained numerically.

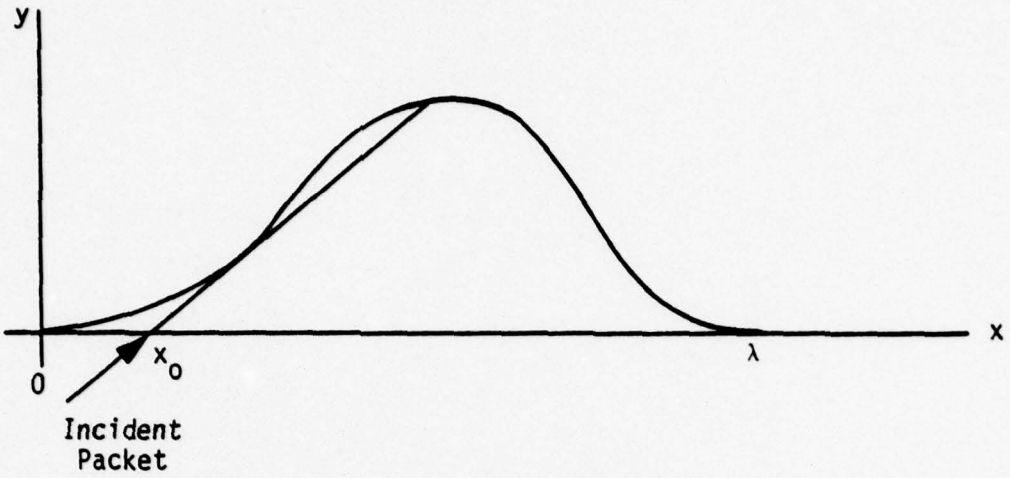

Figure 3.9. Geometry for the Case of Onset of Shadowing.

The sawtooth profile was also reinvestigated assuming no second scattering so we could compare with the sinusoidal surface in the non-shadowed case, Eqs. (3.68) and (3.69). The results are

$$\bar{m}_r \text{ (sawtooth)} = m_i + 2\frac{S^2}{m_i} \tag{3.70}$$

$$\bar{m}_r \text{ (sinusoidal)} = m_i + \frac{\pi^2}{4}\frac{S^2}{m_i} \tag{3.71}$$

$$\sigma^2 \text{ (sawtooth)} = 4S^2\left(1 - \frac{S^2}{m_i^2}\right) \tag{3.72}$$

$$\sigma^2 \text{ (sinusoidal)} = \left(\frac{\pi^2}{2}\right) S^2\left(1 - \frac{\pi^2}{8}\frac{S^2}{m_i^2}\right) \tag{3.73}$$

We see that in the non-shadowed region the sawtooth model is brought into agreement with the sinusoidal model if, in the sinusoidal model, we set

$$\pi^2 = 8 \quad . \tag{3.74}$$

In Figure 3.10 we show $\bar{m}_r/S$ for the sawtooth with no second scattering plotted against m_i/S. While in Figure 3.11 we have the corresponding results for the sinusoidal model. Note that in this case we plot $\bar{m}_r/S'$ versus m_i/S' where

$$S' = \frac{2\pi\ \alpha}{\sqrt{2}\ \lambda} \tag{3.75}$$

whereas for the sawtooth model S is used, where

$$S = 4\ \frac{\alpha}{\lambda} \quad . \tag{3.76}$$

This transformation makes the model results identical in the non-shadowed region. Figures 3.12 and 3.13 contain the corresponding results for σ^2.

First, we compare the results of the sawtooth model with and without second scattering, i.e., Figures 3.6 and 3.10. We see the following effects due to the neglect of second scattering:

1. For $m_i \leq S$ there is no effect on either the mean or the variance;
2. For $m_i \geq 3S$ there is no effect on either the mean or the variance;
3. For $S \leq m_i \leq 3S$ the neglect of second scattering
   (a) decreases the mean
   (b) increases the variance.

The surface duct problem that will be discussed in Section 4 had $S = 0.0025$ with $m_i \approx \tan 2^\circ = 0.035$ so $m_i/S \cong 14$. Thus, in the sawtooth model for this problem we can safely neglect second scattering.

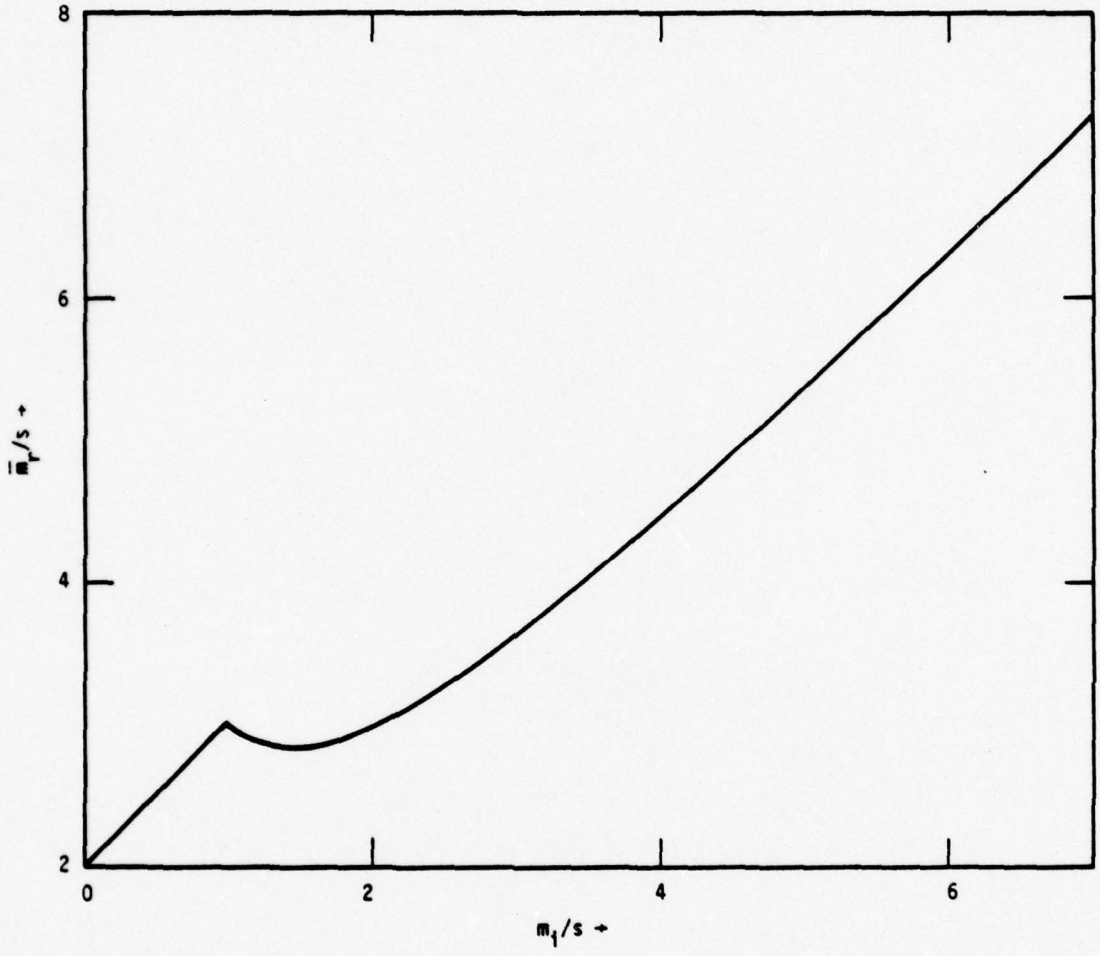

Figure 3.10. Mean Value of Reflection Tangent $\bar{m}_r$ Versus Incident Tangent m_i, Neglecting Second Scattering for Sawtooth Model ($S = 4\alpha/\lambda$).

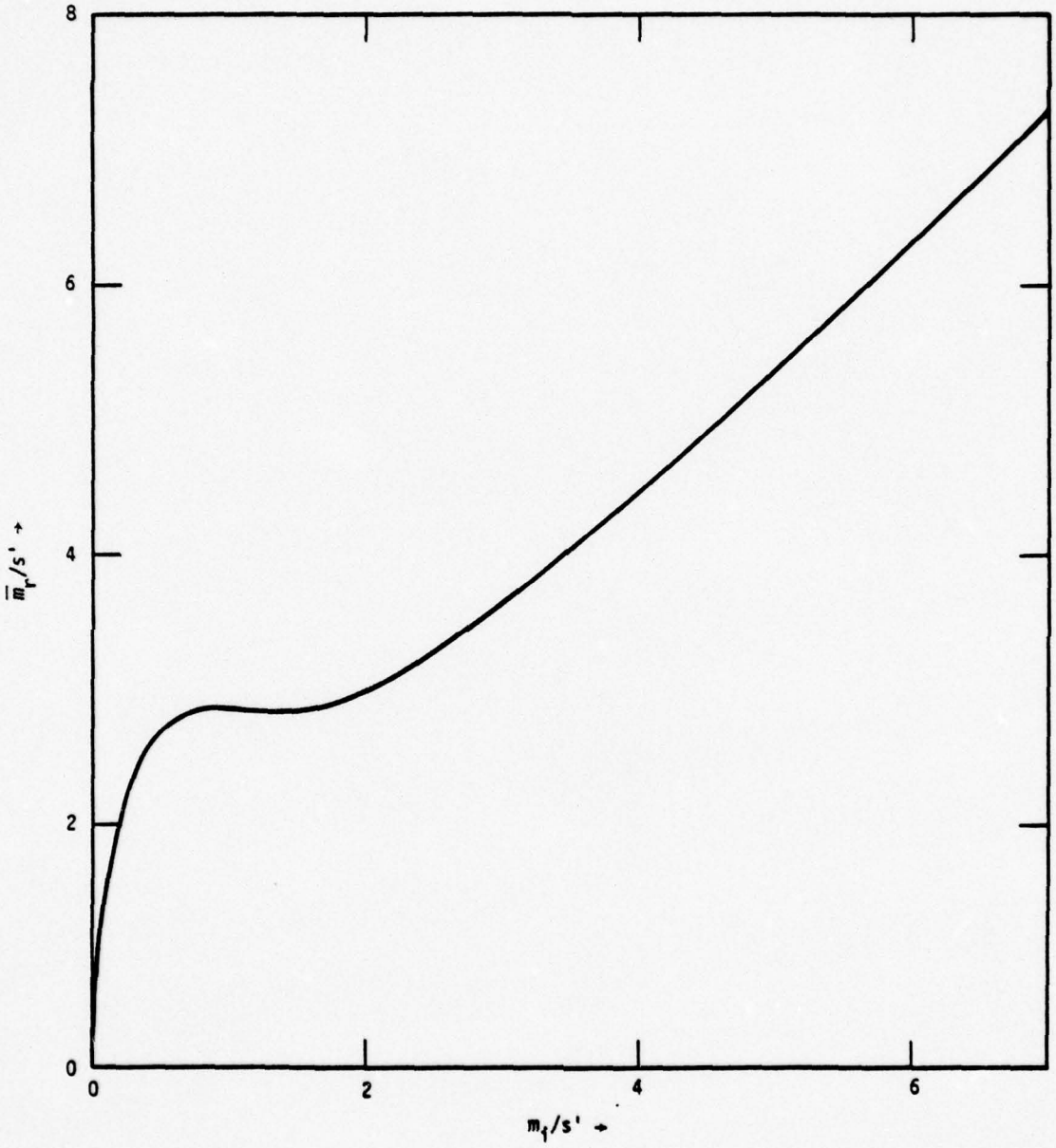

Figure 3.11. Mean Value of Reflection Tangent $\bar{m}_r$ Versus Incident Tangent m_i, Neglecting Second Scattering for Sinusoidal Model ($S' = 2\pi\alpha/\sqrt{2}\lambda$).

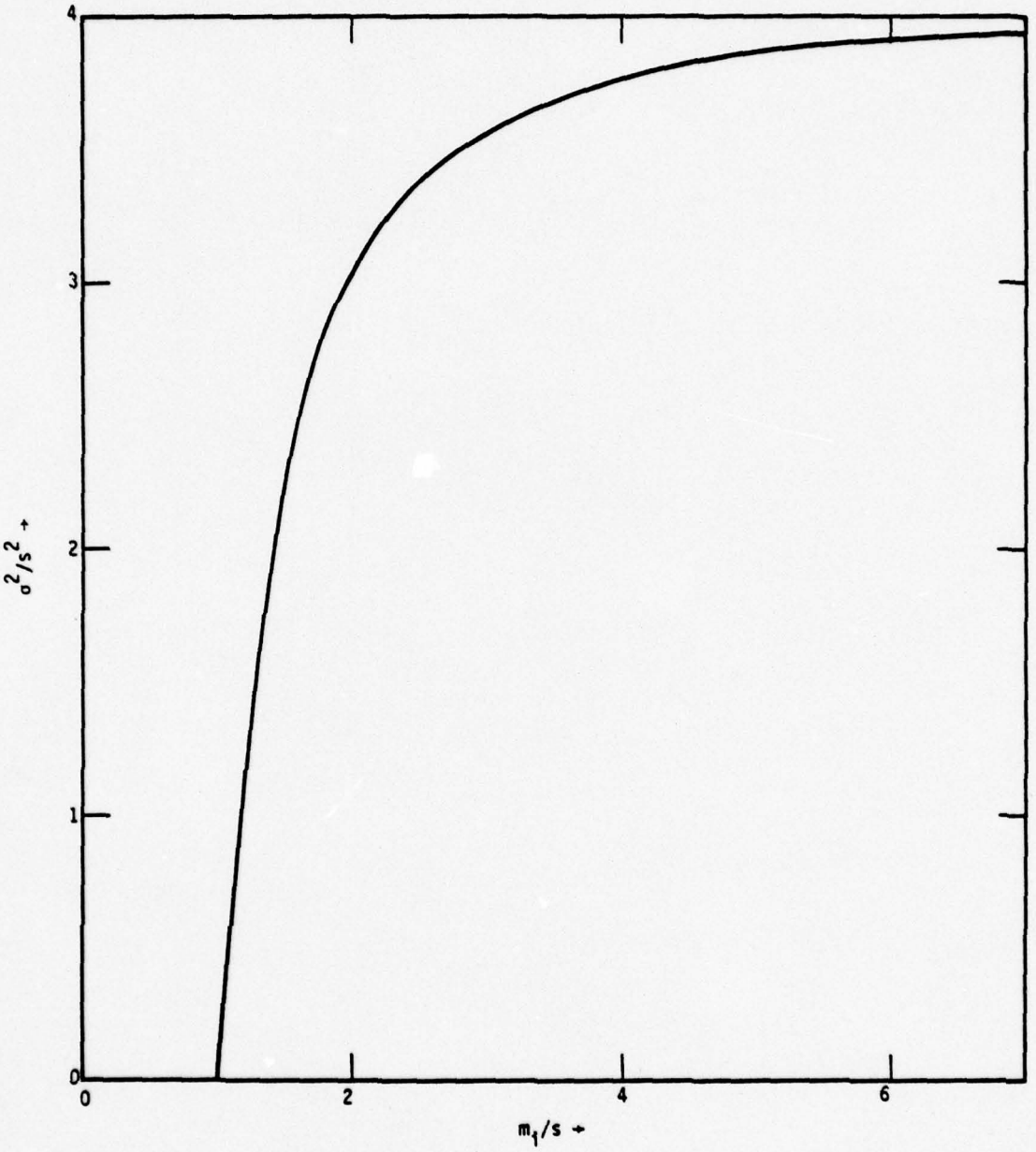

Figure 3.12. Variance of Reflection Tangent σ^2 Versus Incident Tangent m_i, Neglecting Second Scattering for Sawtooth Model ($S = 4\alpha/\lambda$).

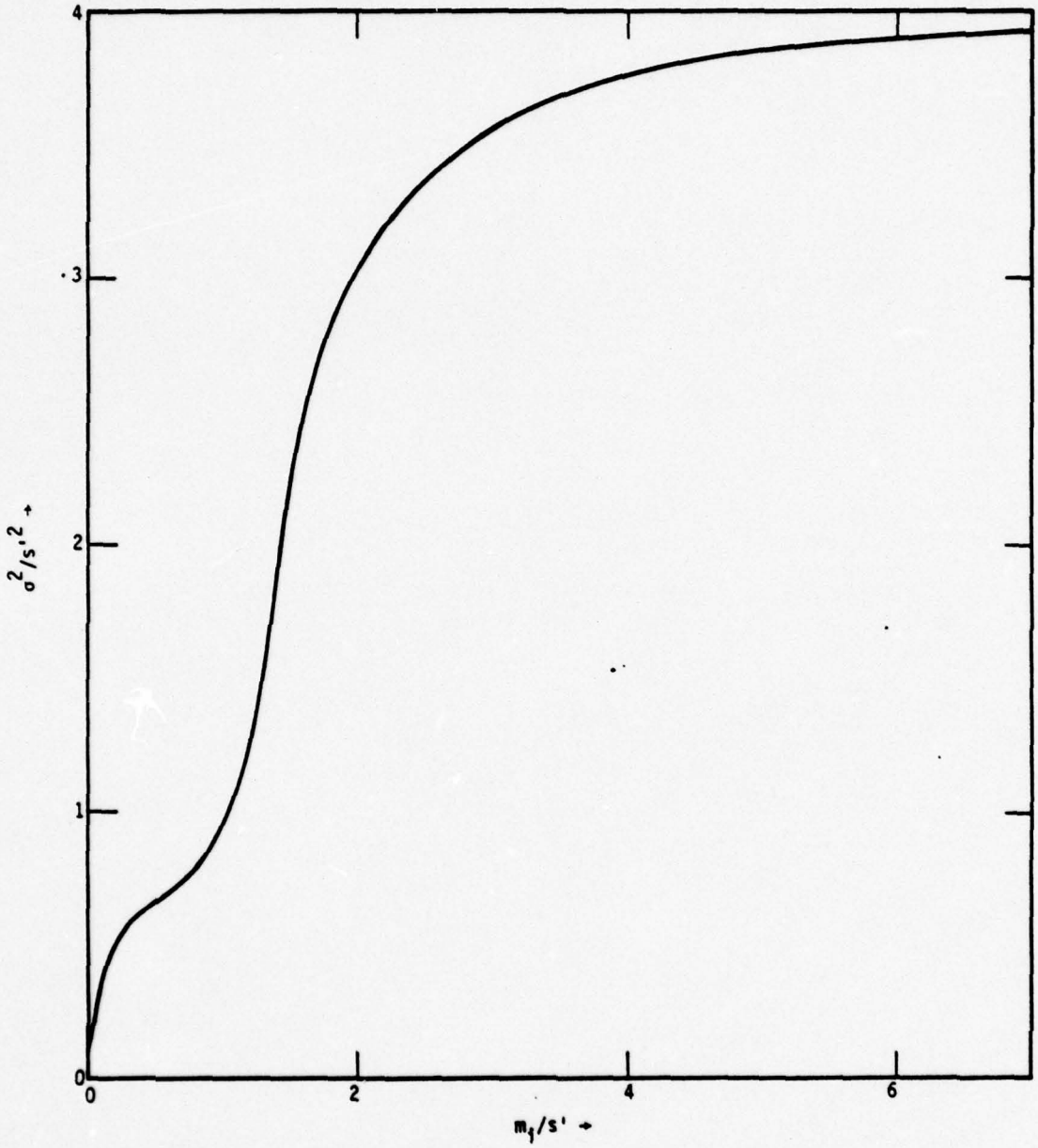

Figure 3.13. Mean Value of Reflection Tangent σ^2 Versus Incident Tangent m_i, Neglecting Second Scattering for Sinusoidal Model ($S' = 2\pi\alpha/\sqrt{2}\lambda$).

We now compare the sinusoidal model without second scattering with the sawtooth model also without second scattering. In the non-shadowing region $\bar{m}_r$ and σ^2 as a function of S' have the same form as in the sawtooth model when plotted as a function of S. Thus, for

$$m_i > 2\pi \frac{\alpha}{\lambda} = \sqrt{2}\, S'$$

the sinusoidal and sawtooth models are in exact agreement if S' in the sinusoidal model replaces S in the sawtooth model. For the case

$$m_i < \sqrt{2}\, S'$$

there is a smoothing which occurs in the sinusoidal model due to the fact that a distribution of scattering slopes is available. Also, in the sinusoidal model as m_i/S' approaches zero so does $\bar{m}_r/S'$. This is because the available points on the sinusoid where scattering can take place are those corresponding to very small slopes.

We conclude that for our applications the sawtooth model is perfectly adequate. If, in the future, situations are encountered where m_i/S' is very small, provisions would have to be made to more accurately include the region below $m_i/S' = \sqrt{2}$. Also, the effects of multiple scattering would have to be investigated.

3.2 SCATTERING BY INTERNAL WAVES

3.2.1 The Total Scattering Cross Section

In this section we discuss how the internal wave spectrum of Garrett and Munk[8,9] is sampled for use in the Monte Carlo acoustic transport code, ACTOR.

From Reference 28 the acoustic scattering cross section can be written

$$\sigma(\hat{q},\hat{q}') = \frac{q^4}{2k} F(k,Q,Z) \qquad (3.77)$$

where $F(k,Q,Z)$ is the power spectrum of sound speed fluctuations and the following definitions hold:

$\hat{q}'$ = unit vector in direction of incident packet

$\hat{q}$ = unit vector in direction of scattered packet

$\vec{K} = q(\hat{q} - \hat{q}')$

q = wavenumber corresponding to momentum transfer vector, $\vec{K}$

$\vec{K} = (k,Q)$

$k = \sqrt{k_1^2 + k_2^2}$ = horizontal component of $\vec{K}$

Q = vertical component of $\vec{K}$

We are interested in evaluating the scattering coefficient

$$\sigma_s(\hat{q}') = \int \sigma(\hat{q},\hat{q}')d\Omega_q \quad . \tag{3.78}$$

Since we are integrating over all $\hat{q}$ directions with $\hat{q}'$ fixed we see

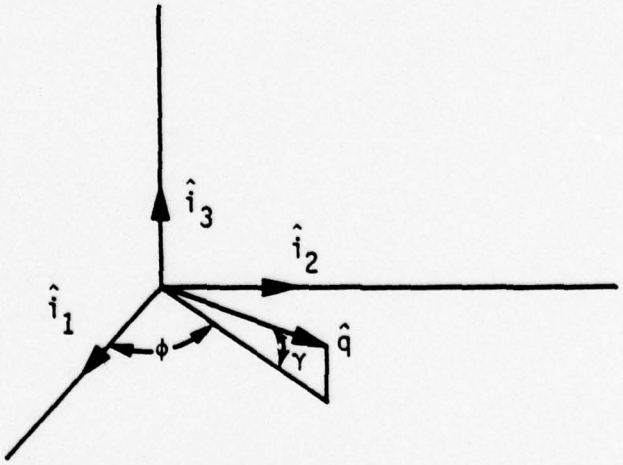

Figure 3.14. Geometry Schematic for $d\Omega_q$ Calculation.

from Figure 3.14 that

$$d\Omega_q = \cos\gamma \, d\gamma d\phi$$

$$= d\gamma d\phi \quad \text{for small } \gamma \text{, i.e., small vertical angles.} \tag{3.79}$$

Now

$$d\vec{K} = (dk, dQ)$$

$$\cong (q d\phi, q d\gamma) \tag{3.80}$$

or

$$d\gamma d\phi = \frac{dk dQ}{q^2} \quad . \tag{3.81}$$

Thus

$$\sigma_s(\hat{q}') = \int \frac{q^4}{2k} F(k,Q,Z) \frac{dk dQ}{q^2}$$

$$= \frac{q^2}{2} \int \frac{1}{k} F(k,Q,Z) dk dQ \quad 0 < k \lesssim Q \quad .$$

Using the Garrett-Munk[8,9] power spectrum we get

$$\sigma_s(\hat{q}') = \frac{\alpha}{2} q^2 \int_{Q_{min}}^{\infty} dQ \int_0^Q dk \, \frac{kQ}{[k^2 + \beta^2 Q^2]^2 [Q^2 + Q_*^2]} \tag{3.82}$$

where

$$\alpha = \frac{8}{\pi} \langle \mu^2 \rangle \frac{\omega_i}{n_o} \frac{j_*}{B} \tag{3.83}$$

$$\beta^2 = \frac{\omega_i^2}{n^2} << 1 \tag{3.84}$$

Q_{min} = a minimum allowable change in vertical wavenumber upon scattering due to finite depth of the ocean .

$$Q_* = j_* \pi \, n/(Bn_o) \tag{3.85}$$

$$Q = j \, \pi \, n/(Bn_o) \quad . \tag{3.86}$$

In the above equations the following definitions hold:

$$\langle \mu^2 \rangle = \langle \mu_o^2 \rangle \, (n/n_o)^3$$

$\langle \mu_o^2 \rangle$ = variance of the sound-speed fluctuations extrapolated to the surface

$\cong 2.5 \times 10^{-7}$

ω_i = inertial frequency (7.3×10^{-5} sec^{-1} at 30° latitude)

$n = n(Z)$ = buoyancy (Brunt-Vaisälä) frequency

B = scale of the sound channel ($\sim$ 1 km)

n_o = n at the surface (5.2×10^{-3} sec^{-1})

j_* = constant, suggested in Reference 29 to be 3.

Equation (3.82) can be written

$$\sigma_s(\hat{q}') = \frac{\alpha}{2} q^2 \int_{Q_{min}}^{\infty} dQ \, \frac{Q}{(Q^2 + Q_*^2)} \int_0^Q dk \, \frac{k}{[k^2 + \beta^2 Q^2]^2} \quad . \tag{3.87}$$

Letting

$$x = k^2 + \beta^2 Q^2 \quad , \quad dx = 2kdk$$

and

$$k = 0 \Rightarrow x = \beta^2 Q^2$$

$$k = Q \Rightarrow x = (1 + \beta^2) Q^2$$

we get

$$\sigma_s(\hat{q}') = \frac{\alpha}{4} q^2 \int_{Q_{min}}^{\infty} dQ \, \frac{Q}{(Q^2 + Q_\star^2)} \, \frac{Q^2}{\beta^2 Q^2 (1 + \beta^2) Q^2} \tag{3.88}$$

and using the fact that $\beta^2 << 1$ we get

$$\sigma_s(\hat{q}') = \frac{\alpha}{4\beta^2} q^2 \int_{Q_{min}}^{\infty} \frac{dQ}{Q(Q^2 + Q_\star^2)} \quad . \tag{3.89}$$

We must now assign a value to Q_{min}. Presumably $2\pi/(\text{ocean depth}) \leq Q_\star$. Since Q_{min} only appears in the argument of a log, its actual value is rather unimportant and we choose $Q_{min} = Q_\star$. We then get

$$\sigma_s(\hat{q}') = - \frac{\alpha}{4\beta^2} \frac{q^2}{2Q_\star^2} \ell n(\tfrac{1}{2})$$

$$= \frac{1}{\pi^3} q^2 \langle \mu^2 \rangle \frac{n_o}{\omega_i} \frac{B}{j_\star} \ell n(2) \quad . \tag{3.90}$$

Using $j_\star = 3$, $B = 1.2$ km and scaling to a depth of $-B$ gives

$$\sigma_s(\hat{q}') = 0.13 \, f_{KHz}^2 \left[\frac{n(Z)}{n(-B)}\right]^3 \text{ km}^{-1}$$

$$= 0.56 \, f_{KHz}^2 \left[\frac{n(Z)}{n(-B)}\right]^3 \text{ dB/km} \tag{3.91}$$

where f is the acoustic frequency in kilohertz and the scaling used the canonical form

$$n(Z) = n_o e^{Z/B}, \quad Z \leq 0 \quad . \tag{3.92}$$

3.2.2 Sampling the Scattering Kernel

After integrating over the horizontal wavenumber, i.e., in going from Eq. (3.87) to (3.89), we obtain the change in the vertical component of $\vec{K} = q(\hat{q} - \hat{q}')$ to be given by the density function

$$\rho(Q) = \frac{1}{Q(Q^2 + Q_*^2)} \tag{3.93}$$

in which

$$\int_{Q_*}^{\infty} \rho(Q)dQ = \frac{1}{2Q_*^2} \ell n(2) \tag{3.94}$$

To sample from $\rho(Q)$ we normalize by the right side of Eq. (3.94) and using the results of Section 2.3.2 we set

$$\xi = \frac{\displaystyle\int_{Q_*}^{Q} \frac{dQ'}{Q'(Q'^2 + Q_*^2)}}{\dfrac{1}{2Q_*^2} \ell n(2)} \tag{3.95}$$

or

$$\xi \ell n(2) = \ell n \left(\frac{Q^2 + Q_*^2}{Q^2} \right) \tag{3.96}$$

hence

$$Q = \pm \frac{Q_\star}{\sqrt{2^\xi - 1}} \tag{3.97}$$

When $\xi = 1$, $Q = \pm Q_\star$ as it should and in Table 3.3 we list various values of Q for the corresponding ξ.

Table 3.3. Values of Q Corresponding to Various Values of the Random Number, ξ.

ξ	Q
1.0	$\pm\ Q_\star$
0.75	$\pm$ 1.21 $Q_\star$
0.50	$\pm$ 1.55 $Q_\star$
0.25	$\pm$ 2.30 $Q_\star$
0.10	$\pm$ 3.73 $Q_\star$
0.01	$\pm$ 12.00 $Q_\star$
0.001	$\pm$ 38.00 $Q_\star$

We see from this table that $|Q|$ satisfies the following:

50% of the time $|Q|$ will lie between $Q_\star$ and 1.55 $Q_\star$

75% of the time $|Q|$ will lie between $Q_\star$ and 2.30 $Q_\star$

90% of the time $|Q|$ will lie between $Q_\star$ and 3.73 $Q_\star$

99% of the time $|Q|$ will lie between $Q_\star$ and 12.00 $Q_\star$

99.9% of the time $|Q|$ will lie between $Q_\star$ and 38.00 $Q_\star$

Translating these Q's into changes in vertical angle we get (at $Z = -B = -1.2$ km)

$$Q_\star = \frac{j_\star \pi\ n}{B n_o} = 2.88\ \text{km}^{-1} \quad . \tag{3.98}$$

Now, the acoustic wavenumber is

$$q = \frac{2\pi f}{c} \cong 4 \times 10^{3} \text{ km}^{-1} \quad \text{at} \quad f = 1000 \text{ Hz}$$

so, referring to Figure 3.15 we see that

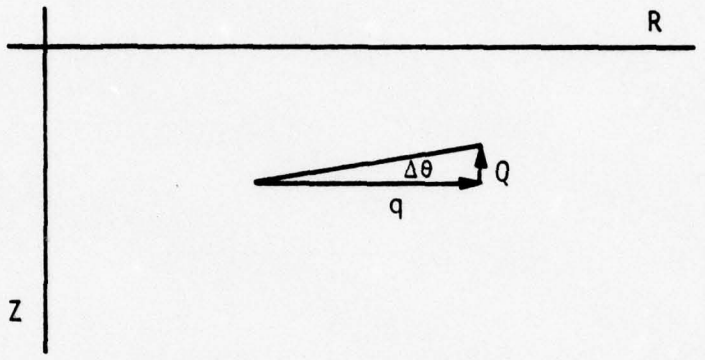

Figure 3.15. Vertical Angle Change Due to Scattering.

for $Q = Q_{*}$ $\quad \Delta\theta \cong 0.04^{\circ}$

$Q = 4\ Q_{*}$ $\quad \Delta\theta \cong 0.16^{\circ}$

$Q = 12\ Q_{*}$ $\quad \Delta\theta \cong 0.48^{\circ}$.

We assume small angles and that $\Delta(\text{Tan}\theta) = \Delta\theta$.

An approximate picture of the probability density function is shown in Figure 3.16.

Watson[28] derived an expression for the rms vertical scattering angle (in radians) for a ray on the sound channel axis. He found

$$(\overline{\theta_z^2})^{\frac{1}{2}} = 1.1 \times 10^{-3}\ R_{km}^{\frac{1}{2}} \quad . \qquad (3.99)$$

The derivation made use of the diffusion approximation in angle in which no limit is placed on the smallness of $|\theta - \theta'|$.

We simulated the same problem, i.e., a channel axis ray undergoing multiple scattering as it proceeds in range, using Monte Carlo methods in which the scattering cross section was obtained from Eq. (3.91) and the scattering angle was obtained by sampling from Eq. (3.98), the probability density of which is shown in Figure 3.16. An interesting difference between the Monte Carlo method and the diffusion method lies in the fact that the Monte Carlo method samples from a distribution which requires each scattering angle to exceed some minimum, while the diffusion method allows all $|\theta - \theta'| > 0$. It is remarkable, however, that both methods give essentially the same results for the rms scattering angle as a function of range as can be seen from Figure 3.17. This might not be surprising at large ranges after many scatterings have occurred, but the good agreement even at 10 km (~ 2 scatterings) is surprising.

We did not check the angular distribution as a function of range but it would not be surprising if substantial differences appeared between the results predicted by the two methods at short ranges. Some effort will be made to investigate this at a later date.

3.2.3 The Gaussian Model for Internal Wave Scattering

In Sections 3.2.1 and 3.2.2 the Garrett-Munk model for internal wave scattering was discussed. A salient feature of that model as presented was the neglect of range-dependent sound-speed fluctuation correlations. This led to a scattering kernel which depended only on the difference between the incident and scattered angles and the scattering integral becomes a convolution integral.[6] The development by Watson[28] also ignored range-dependent correlations. We will show here how the Garrett-Munk formalism changes when a more accurate expression is used for the horizontal change in wavenumber. This results from taking into account the range-dependent sound-speed fluctuations. We will then suggest a simpler model, the Gaussian model, for doing approximately the same thing.

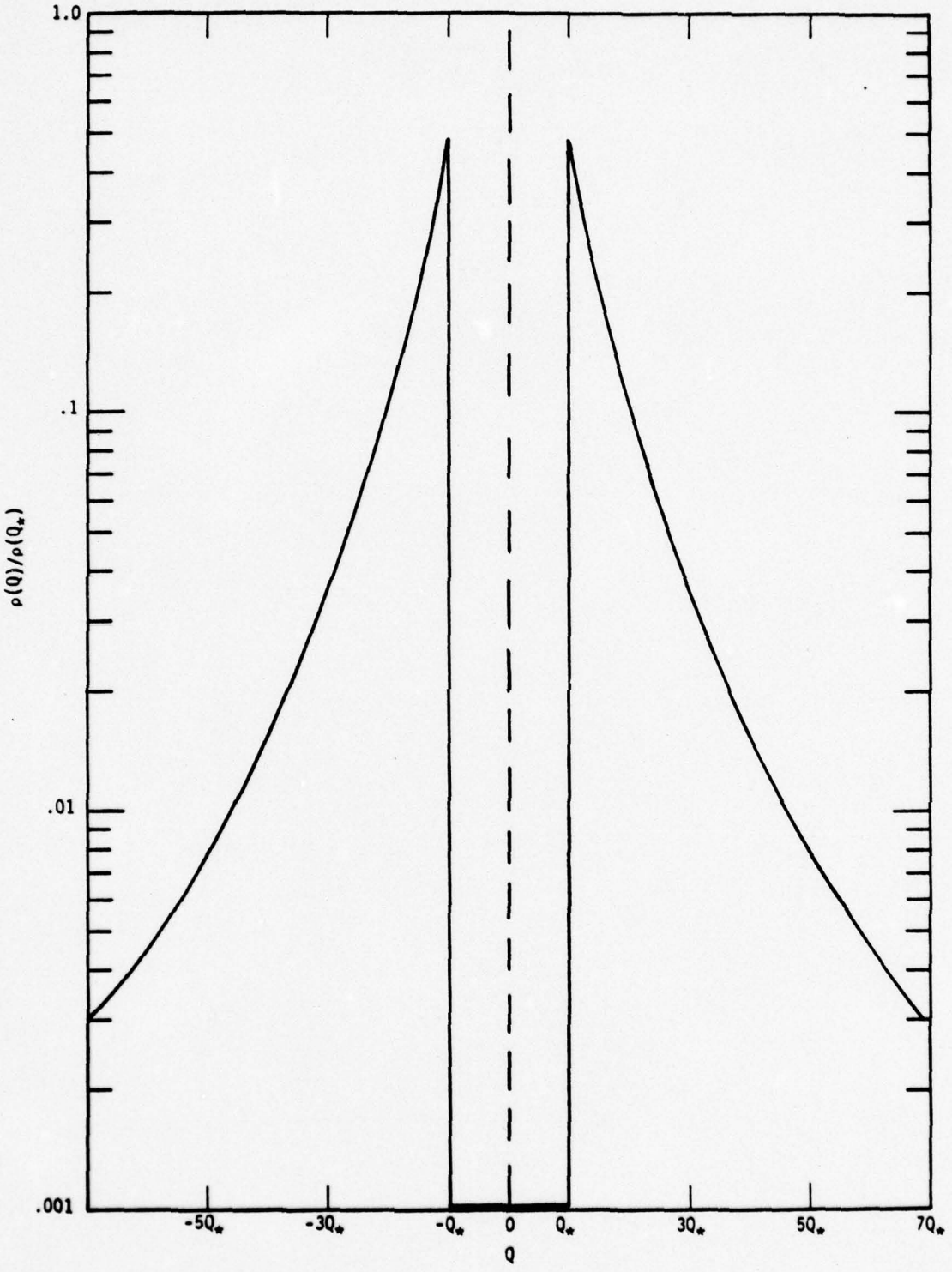

Figure 3.16. Relative Probability Density $\rho(Q)/\rho(Q_*)$ Versus Q.

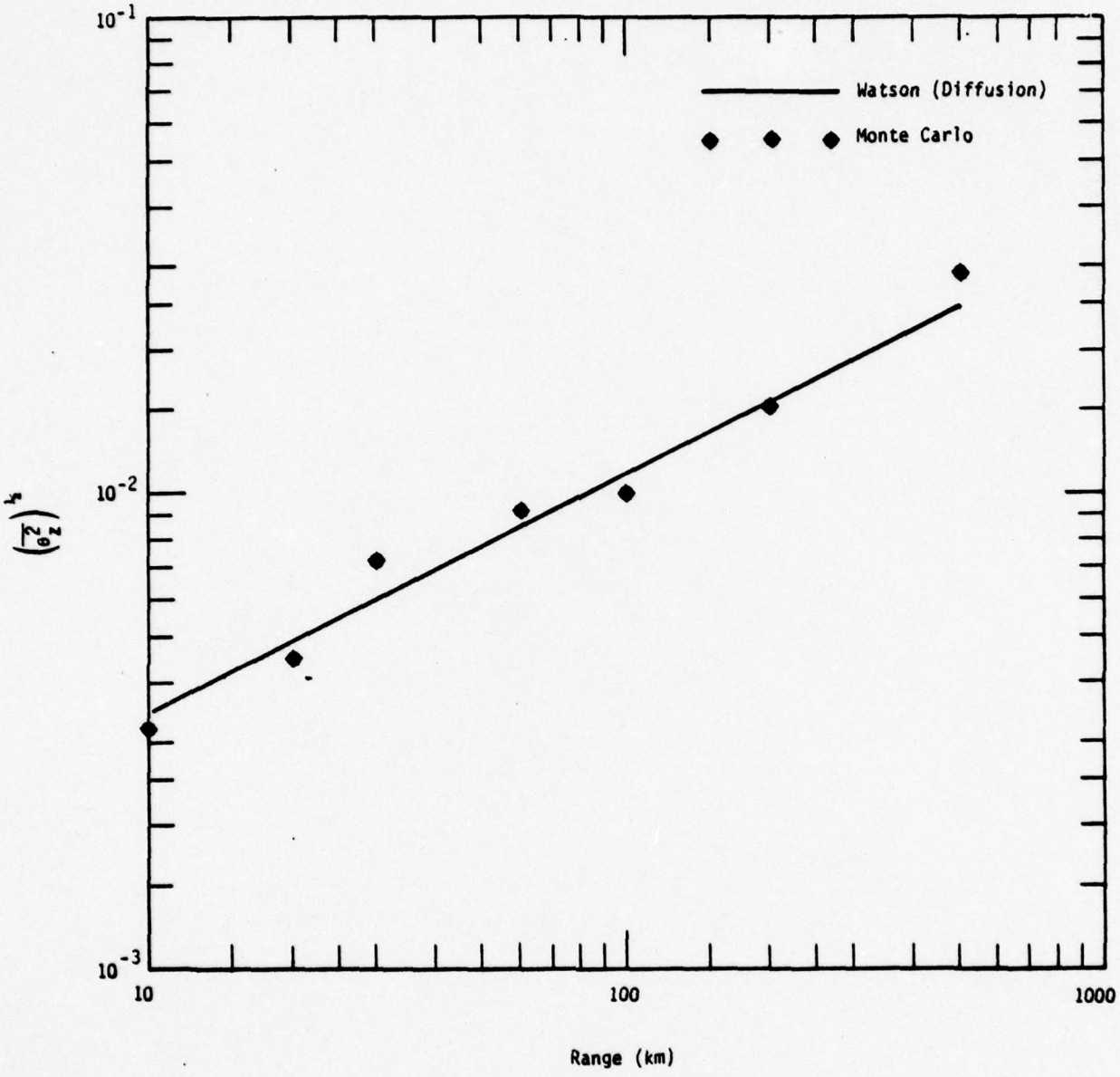

Figure 3.17. RMS Vertical Scattering Angle for a Channel Axis Ray as Determined by Diffusion in Angle and by Monte Carlo.

Using θ as the small vertical scattered angle with θ' the incident angle we have

$$\sigma_s(\theta') = \iint \frac{q^4}{2k} F(k,\theta,z,)d\theta d\phi \tag{3.100}$$

$$Q \cong q(\theta-\theta')$$

$$\frac{k^2}{q^2} \cong (\phi-\phi')^2 + (\tfrac{1}{2}\theta^2-\tfrac{1}{2}\theta'^2)^2 \tag{3.101}$$

where the notation is the same as in Section 3.2.1. It is the second term in this expression for $(k/q)^2$ that is new. Thus,

$$\sigma_s = \iint \frac{q^4}{2|\phi-\phi'|} F(q\sqrt{(\phi-\phi')^2+(\tfrac{1}{2}\theta^2-\tfrac{1}{2}\theta'^2)^2},\ q(\theta-\theta'),z)d\theta d\phi$$

$$= \int g(\theta,\theta',z)d\theta \tag{3.102}$$

where

$$g(\theta,\theta',z) = \int \frac{q^4}{2|\phi-\phi'|} F(q\sqrt{(\phi-\phi')^2 + (\tfrac{1}{2}\theta^2-\tfrac{1}{2}\theta'^2)^2},\ q(\theta-\theta'),z)d\phi$$

$$\cong \alpha q^3 \frac{|\theta-\theta'|}{\left[q^2(\theta-\theta')^2+Q_*^2\right]} \int_0^{q|\theta-\theta'|} \frac{kdk}{\left[k^2+q^2(\tfrac{1}{2}\theta^2-\tfrac{1}{2}\theta'^2)^2+\beta^2q^2(\theta-\theta')^2\right]^2} . \tag{3.103}$$

After performing the integration

$$g(\theta,\theta',z) = \frac{\alpha/2}{|\theta-\theta'|\left[(\theta-\theta')^2+Q_*^2(z)\right]\left[\beta^2(z) + (\frac{\theta+\theta'}{2})^2\right]} . \tag{3.104}$$

where

$$Q_*(z) = (J_*\Pi/qB)\ (n(z)/n_o)$$

and

$$\beta(z) = \omega_i/n(z) \quad .$$

The function g is the rate per unit distance along a ray for scattering from θ' to θ at depth z. It is even in θ and θ', which is the principle of detailed balance.

The additional term, not found before, is $[(\theta+\theta')/2]^2$. Note that it is only important when $(\theta+\theta')/2 > \beta(z)$. The parameter β measures the degree of anisotropy. If β were of order unity, then the additional term would not be needed because all angles are small anyway. The fact that corrections may be needed for angles of order of the anisotropy factor is here confirmed explicitly. We have

$$\beta(z) = \frac{\omega_i}{n_o} e^{-z/B} \quad , z < 0 \quad .$$

For the canonical values, $\beta(z) = 0.014\ e^{-z}$ where z is in kilometers and Table 3.4 lists the values of β and θ_* for various depths.

Table 3.4. Depth Dependence of β and θ_* .

z(km)	β(rad)	β(deg)	θ_*(rad)	θ_*(deg)
0	0.014	0.8	0.00225	0.13
-1	0.038	2.2	0.00083	0.05
-2	0.104	5.9		
-3	0.282	16.2		

Also, at 1 kHz,

$$\theta_*(z) = 0.00225\ e^{z} \quad ,$$

and it is seen that the correction term is only needed near the surface where the anisotropy is large.

The total cross section is given by

$$\sigma(\theta',z) = \frac{\alpha}{2} \int_{\theta'+\theta_*}^{\infty} \frac{d\theta}{|\theta-\theta'| \left[(\theta-\theta')^2+\theta_*^2\right]\left[\beta^2+(\frac{\theta+\theta'}{2})^2\right]}$$

$$+ \frac{\alpha}{2} \int_{-\infty}^{\theta'-\theta_*} \frac{d\theta}{|\theta'-\theta| \left[(\theta-\theta')^2+\theta_*^2\right]\left[\beta^2+(\frac{\theta+\theta'}{2})^2\right]} . \quad (3.105)$$

This can be put into the form

$$\sigma(\theta',z) = \frac{\alpha}{2} \int_1^{\infty} d\xi \left\{\frac{1}{\xi} - \frac{\xi}{\xi^2+1}\right\} \left\{\frac{1}{\beta^2+(\theta'+\frac{\theta_*\xi}{2})^2} + \frac{1}{\beta^2+(\theta'-\frac{\theta_*\xi}{2})^2}\right\} . \quad (3.106)$$

which is much more complicated than before.

In the Gaussion model the scattering kernel is given by

$$W(z,\theta,\theta') = 2\pi q \hat{\Gamma}(z,\theta-\theta', \tfrac{1}{2}\theta^2-\tfrac{1}{2}\theta'^2) . \quad (3.107)$$

where

$$\hat{\Gamma}(z,\theta,u) = \frac{1}{(2\pi)^2} \int dz' \int dr' e^{-iq(\theta z'-ur')} \Gamma(z,z',r) . \quad (3.108)$$

and

$$\Gamma(z,z',r') = \frac{1}{c_o^2} \langle \delta c(z+\tfrac{1}{2}z', r+\tfrac{1}{2}r') \rangle \langle \delta c(z-\tfrac{1}{2}z', r-\tfrac{1}{2}r') \rangle . \quad (3.109)$$

To say more about W, one needs to know the correlation function of sound speed fluctuations $\Gamma(z,z',r')$ or its power spectrum $\hat{\Gamma}(z,\theta,u)$. Usually one is only able to estimate the horizontal and vertical scale

lengths (L_H and L_V, respectively) and the depth dependence of $\Gamma(z,o,o) = 1/c_o^2 \langle \delta c(z,r)\delta c(z,r)\rangle$. It is generally believed that $\Gamma(z,o,o)$ is largest near the main thermocline and decreases rapidly below. Thus a reasonable but crude model for $\Gamma(z,z',r')$ which contains only four parameters is

$$\Gamma(z,z',r') = \sigma^2 e^{-z/B} e^{-z'^2/2L_V^2} e^{-r'^2/2L_H^2} .$$

Typical values might be $\sigma \approx 5\times10^{-4}$, $B \approx 1$ km, $L_V \approx 100$ m, and $L_H \approx 10$ km. An expression for W then follows immediately

$$W(z,\theta,\theta') = L_V L_H k_o^3 \sigma^2 e^{-3z/2B} e^{-\frac{1}{2}L_V^2 k_o^2(\theta-\theta')^2} e^{-\frac{1}{8}L_H^2 k_o^2(\theta^2-\theta'^2)^2}$$

where $\sigma = (\Delta c/c_o)$.

This is the Gaussian model alluded to earlier. It contains, in at least an approximate manner, the essential oceanography and we feel it would be very useful in performing internal wave scattering sensitivity studies. We have not as yet incorporated it into ACTOR; however, at a later date when comparisons of transport theory with the method of path integrals[29] are made, we expect the Gaussian model to play an important role precisely because it does account for range-dependent sound-speed fluctuation correlations whereas the method of path-integrals, as applied to date, does not.

4. THE EXPERIMENTAL DATA AND ITS COMPARISON WITH TRANSPORT AND NORMAL MODE CALCULATIONS

4.1 THE EXPERIMENTAL ACOUSTIC DATA

The experimental data and the normal mode calculations with which we will compare our transport results were both supplied to us by Mel Pedersen and DeWayne White[30] of the Naval Ocean Systems Center, San Diego, California. They also provided the expressions for the sound speed as a function of depth.

The following description of how the experimental data were obtained was taken from Reference 31.

> "The experimental data were obtained in 1955 off the California coast in 2200-fathom water. One ship, towing two acoustic sources, opened range from a second ship on a fixed course at a speed of about three knots. These two sources were 530- and 1030-cps Fessenden oscillators, which were strapped together rigidly and towed at a depth of about 54 ft. This depth was monitored on a pressure (depth) indicator. The two sources were pulsed alternately with evenly-spaced 500-msec pulses. Eight pulses per minute were transmitted at each frequency.
>
> Signals were monitored on hydrophones at nominal depths of 50, 232, and 400 ft. The sound pulses at the two frequencies were separated by means of filters and were recorded on a six-channel recorder. Acoustic travel times were obtained by measuring the time difference between a pulse received by radio transmission and the corresponding acoustic pulse received on the hydrophone at 50-ft depth."

From this description we see that one pulse was received during each 10-yard range interval. The first step in reducing the vast amount of data was to average it over 100-yard intervals. Thus

$$\frac{\bar{I}}{I_{ref}} = \frac{1}{10} \sum_{i=1}^{10} I_i/I_{ref} \qquad (4.1)$$

and

$$\overline{\left(\frac{I}{I_{ref}}\right)^2} = \frac{1}{10}\sum_{i=1}^{10}(I_i/I_{ref})^2 \quad . \tag{4.2}$$

The transmission loss curves are then obtained by plotting $10 \log_{10} (\bar{I}/I_{ref})$ versus range.

The transport equation results provide an expected value for I/I_{ref} averaged over all members of the internal wave ensemble. The measurement, on the other hand, basically picks out only one member of the ensemble since only one measurement was made at each ten-yard interval and the time between measurements was small compared with an internal wave period. If we assume that internal wave phenomena represent a stationary random process, then we can look at the time series in range to deduce a range averaged variance.

$$\overline{\sigma^2} = \overline{\left(\frac{I}{I_{ref}}\right)^2} - \left(\frac{\bar{I}}{I_{ref}}\right)^2 \quad . \tag{4.3}$$

To be sure, the actual standard deviation, σ, is a function of range being smaller in regions of high intensity and larger in regions of low intensity.

The standard deviation data were provided to us by Mel Pedersen[32] as a function of range for each frequency and for each depth. We will not present that data but only provide average values of $\bar{\sigma} = \sqrt{\overline{\sigma^2}}$ for each case. These average values, after appropriate scaling, are given in Table 4.1 and are to be interpreted as meaning that the vast majority of the range dependent σ's for each range-depth case lie below the corresponding value listed in the table.

Table 4.1. Average Standard Deviation in Decibels as a Function of Range and Frequency.

Frequency (Hz)	Depth (ft.)	$\bar{\sigma}$ (db)
530	50	0.7
530	232	0.8
530	400	2.0
1030	50	0.8
1030	232	2.5
1030	400	4.0

4.2 THE SURFACE DUCT MODEL

The vast majority of the transport and normal mode results presented in the next section were obtained using the surface duct model shown in Figure 4.1. This is a two-layer model with layer number one being the top layer. The index of refraction in the i^{th} layer is given by

$$n_i^2 = 1 - 2 \frac{\gamma_i}{c_i} (Z - Z_i) \qquad (4.4)$$

where Z_i is the depth at the top of the i^{th} layer, c_i is the sound speed at the top of the i^{th} layer, and γ_i characterizes the strength of the gradient in the i^{th} layer. The parameters for the two-layer model are given in Table 4.2.

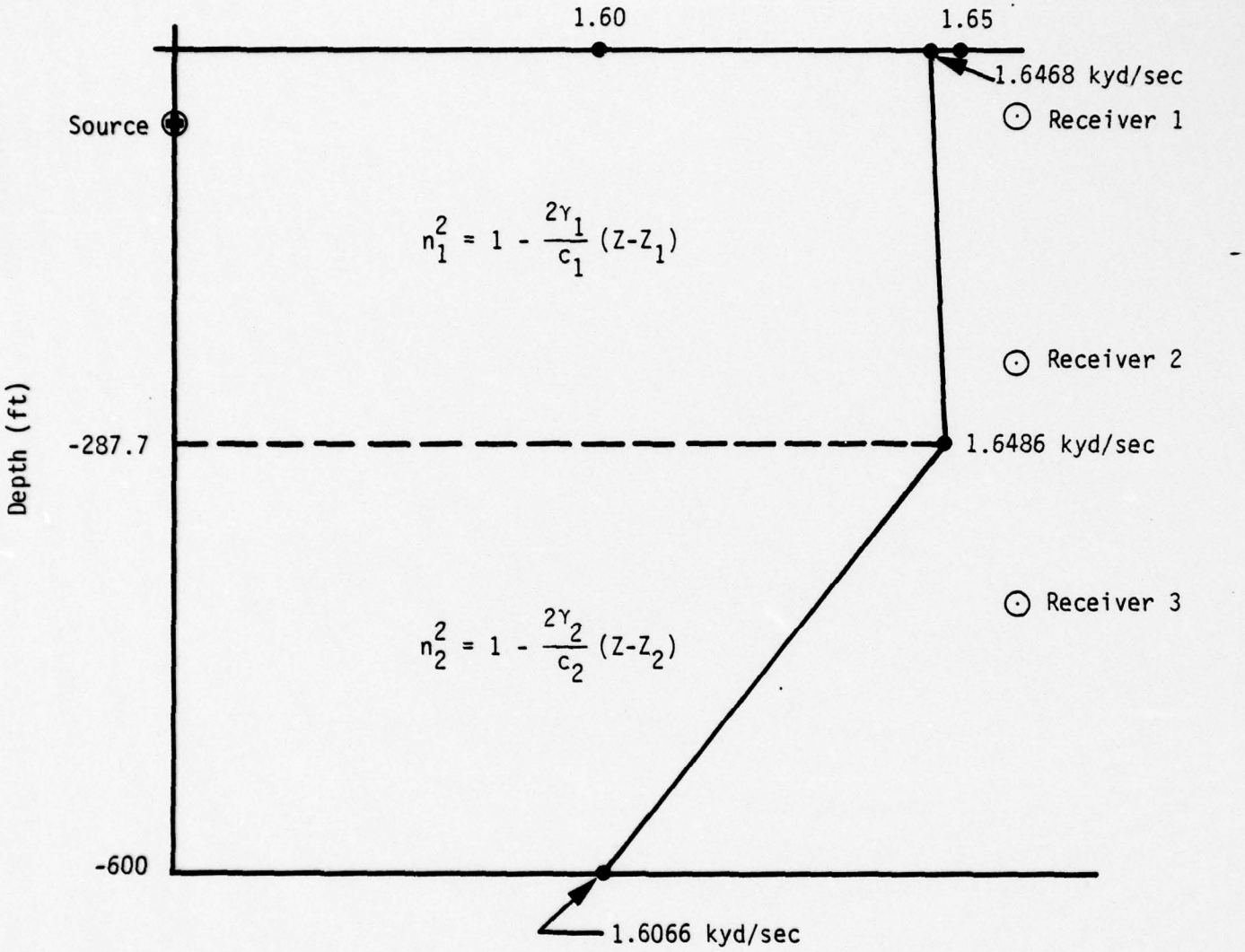

Source Depth = 0.0183333 kyd = 55 feet

Receiver Depths = 0.0166667 kyd = 50 feet
0.0773333 kyd = 232 feet
0.1333333 kyd = 400 feet

Figure 4.1. The Two-Layer Surface Duct Model.

Table 4.2. Parameters Characterizing the Two-Layer Model.

Layer Number, i	c_i(kyd/sec)	γ_i (sec^{-1})	Z_i (yd)
1	1.6468	-0.01884	0.0
2	1.6486	0.418	-95.897

The sound speed at the source and the maximum sound speed were, respectively,

$$c_s = 1.6471 \text{ kyd/sec}$$

$$c_{max} = 1.6486 \text{ kyd/sec}$$

resulting in a propagation cone of 2ε where

$$\varepsilon = \text{Arccos}\,(c_s/c_{max}) = 2.44^\circ \quad . \qquad (4.5)$$

Typically we ran ACTOR using $\varepsilon = 3.0^\circ$.

After making several calculations with ACTOR using the two-layer duct we noticed a consistent tendency to underestimate the intensity at the 50 foot receiver. A small number of problems were subsequently run using a three-layer duct suggested by Pedersen.[33] This was the form used by him in the theoretical calculations reported in Reference 31. This model is shown in Figure 4.2 with the relevant parameters being given in Table 4.3.

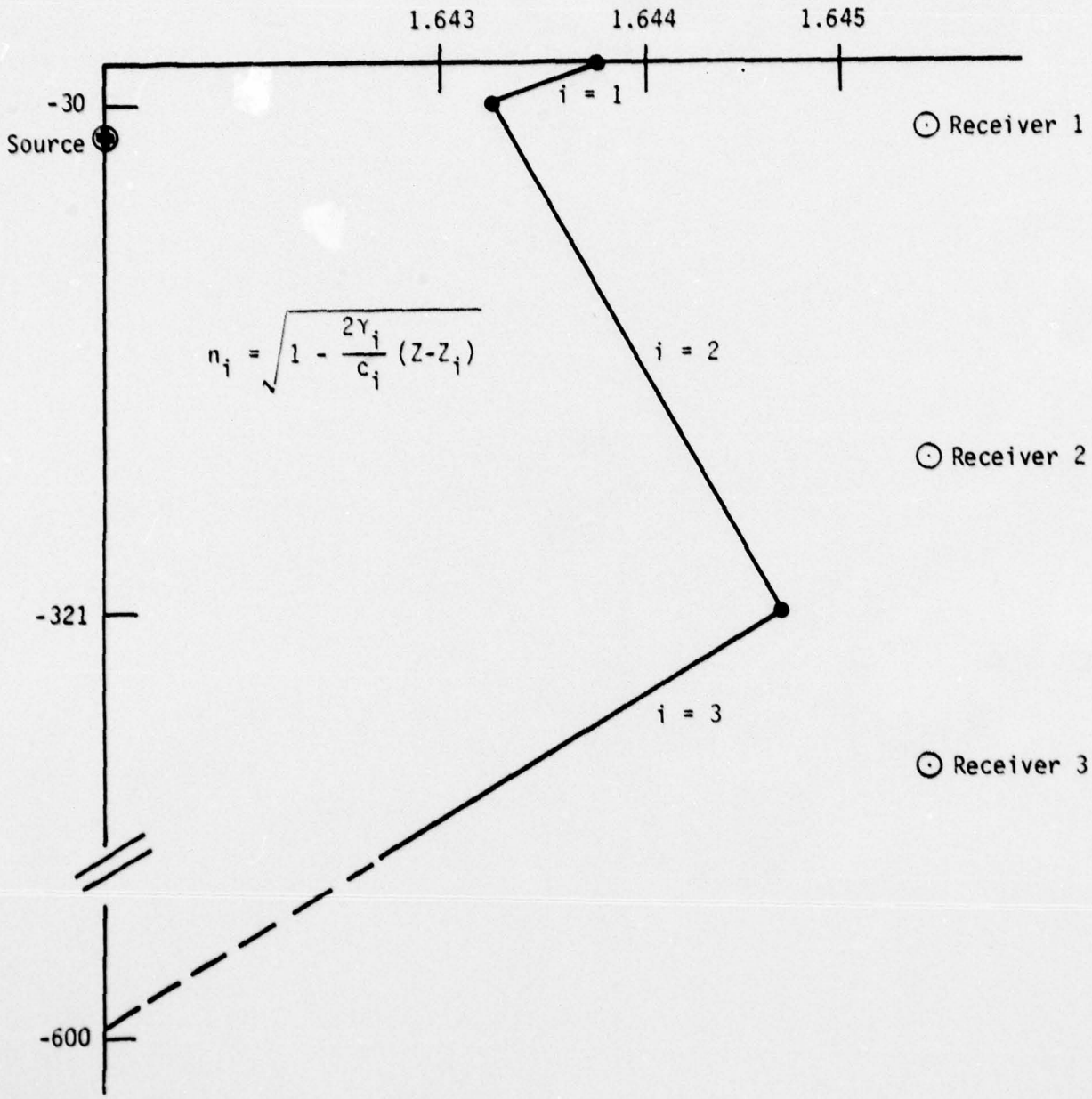

Figure 4.2. The Trilinear Surface Duct Model.

Table 4.3. Parameters Characterizing the Three-Layer Model.

Layer Number, i	c_i (kyd/sec)	γ_i (sec^{-1})	Z_i (ft)
1	1.64384	0.062	0
2	1.64322	-0.015	-30
3	1.64467	0.390	-321

4.3 COMPARISON OF TRANSPORT RESULTS WITH EXPERIMENT AND WITH THE NORMAL MODE RESULTS

In this section we compare the transport results obtained with the ACTOR code with the experimental results and with those obtained using the NOSC normal mode code. The normal mode results are presented as obtained from both the phased addition option as well as the random phase addition option. The normal mode results, as well as the experimental data, were, as mentioned in the previous section, provided by M. Pedersen and D. White.[30]

The transport results depend upon the influence of two physical mechanisms, namely, rough surface scattering and internal wave scattering. The scattering models used to describe these mechanisms were discussed in Section 3. The only surface scattering model used was the sawtooth model and the scattering by internal waves was described by the Garrett-Munk model.

Before presenting any of the results, an explanation concerning the captions is in order. The slope of the sawtooth for the surface model is specified by the symbol S. When there is only specular reflection from a flat surface, S = 0.

The internal wave scattering is characterized by one of the following words in parentheses: general, linear, or quadratic. The explanation is aided by considering Figure 4.3. Above the bottom of the surface duct three options are shown for specifying σ_{IW} the

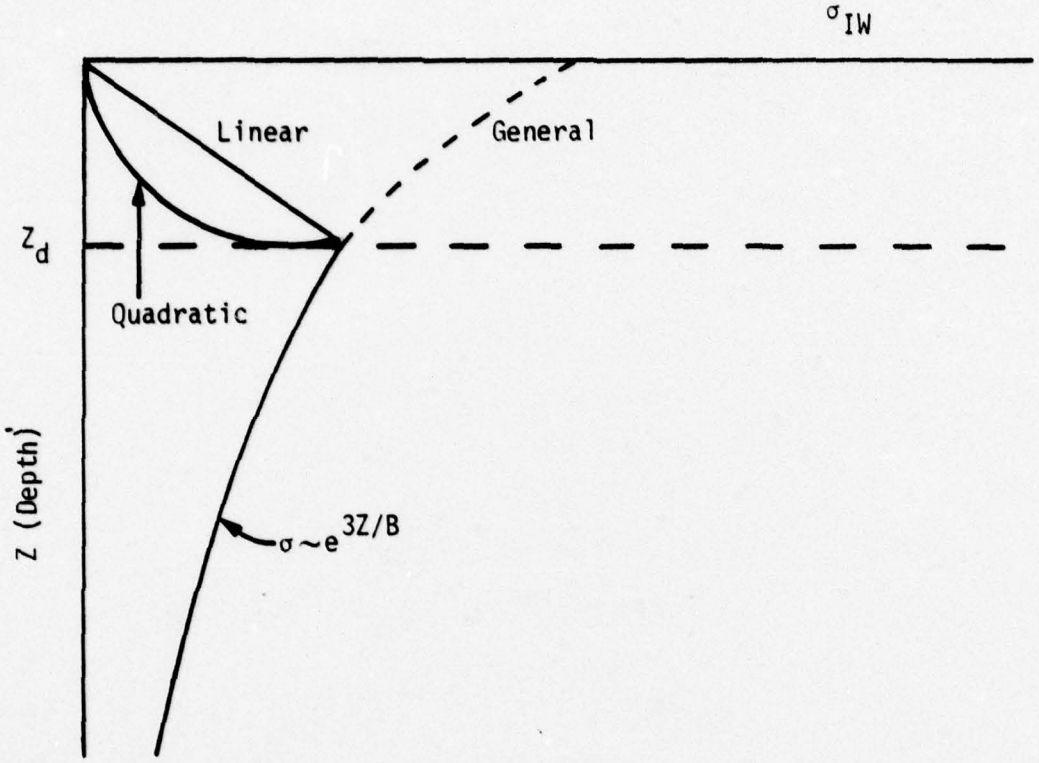

Figure 4.3. Description of the Internal Wave Scattering Cross Section in the Duct.

scattering cross section due to internal waves. The general expression for σ_{IW} is given by Eqs. (3.91) and (3.92).

The first calculation run with internal waves used the general expression for σ_{IW}. The results are shown in Figures 4.4 - 4.6 for ν = 1030 Hz at the receiver depths of 50, 232, and 400 feet, respectively. We see immediately from Figure 4.4 that the scattering near the surface is much too strong since the transport results fall progressively farther below the experimental data as range increases. This is not surprising because the general expression does not apply to the almost isothermal conditions which exist in the surface duct. In fact, we expect the scattering cross section to approach zero at the surface.

We picked two options for letting σ_{IW} go to zero at the surface. They are shown in Figure 4.3 along with the general expression. The linear option is a simple linear interpolation in depth between zero at the surface and the general expression value at the bottom of the duct, Z_d. The quadratic option does quadratic interpolation such that $\sigma_{IW} = 0$ at the surface, $\sigma_{IW} = \sigma_{IW}$ (general expression) at $Z = Z_d$ and $\sigma_{IW} = \frac{1}{4}\,\sigma_{IW}$ (general expression) at $Z = 3/4\ Z_d$.

The case where $S = 0$ (specular reflection from a flat surface) and with the linear option is shown in Figures 4.7 - 4.9. We now see that the transport results at the 50 foot receiver are in much better agreement with the experimental data. Also, the transport results for the 232 foot and 400 foot receivers are quite good. At short range (< 10 kyd) for the 400 foot cross layer case there is some discrepancy but, with the diffraction contribution, the calculated and experimental results would be in reasonably good agreement. An estimate of the diffraction contribution is obtained from the normal mode results. At the 232 foot receiver the transport results are in quite good agreement with the data. To be sure, the transport method does not reproduce all of the structure observed in the experimental data. This is primarily because the transport equation does not include diffraction effects due to the deterministic part of the sound speed profile.

FIG. 4.4 , BILINEAR PROFILE, S-O, INTERNAL WAVE SCATTERING(GENERAL)

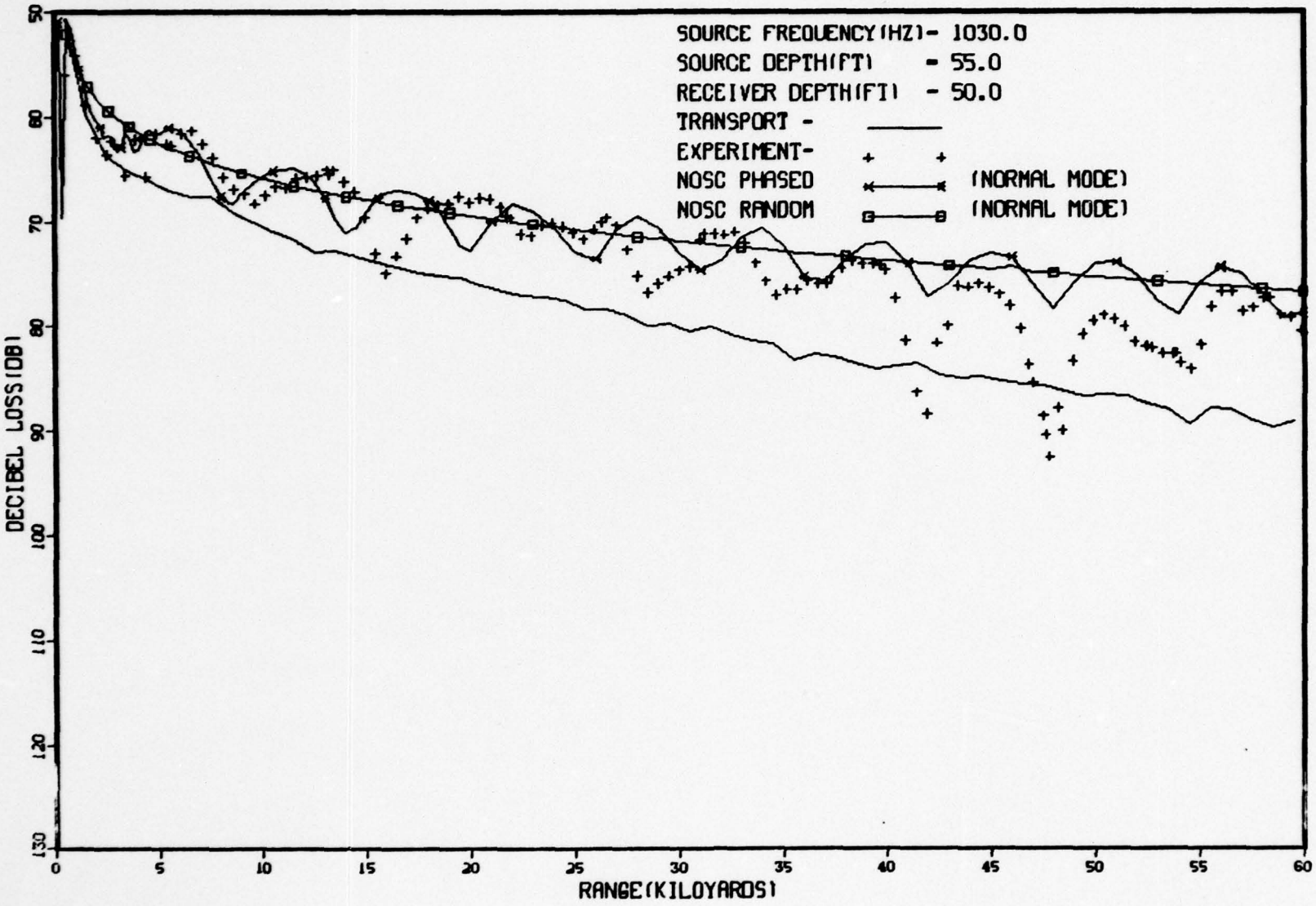

FIG. 4.5 , BILINEAR PROFILE, S-O, INTERNAL WAVE SCATTERING(GENERAL)

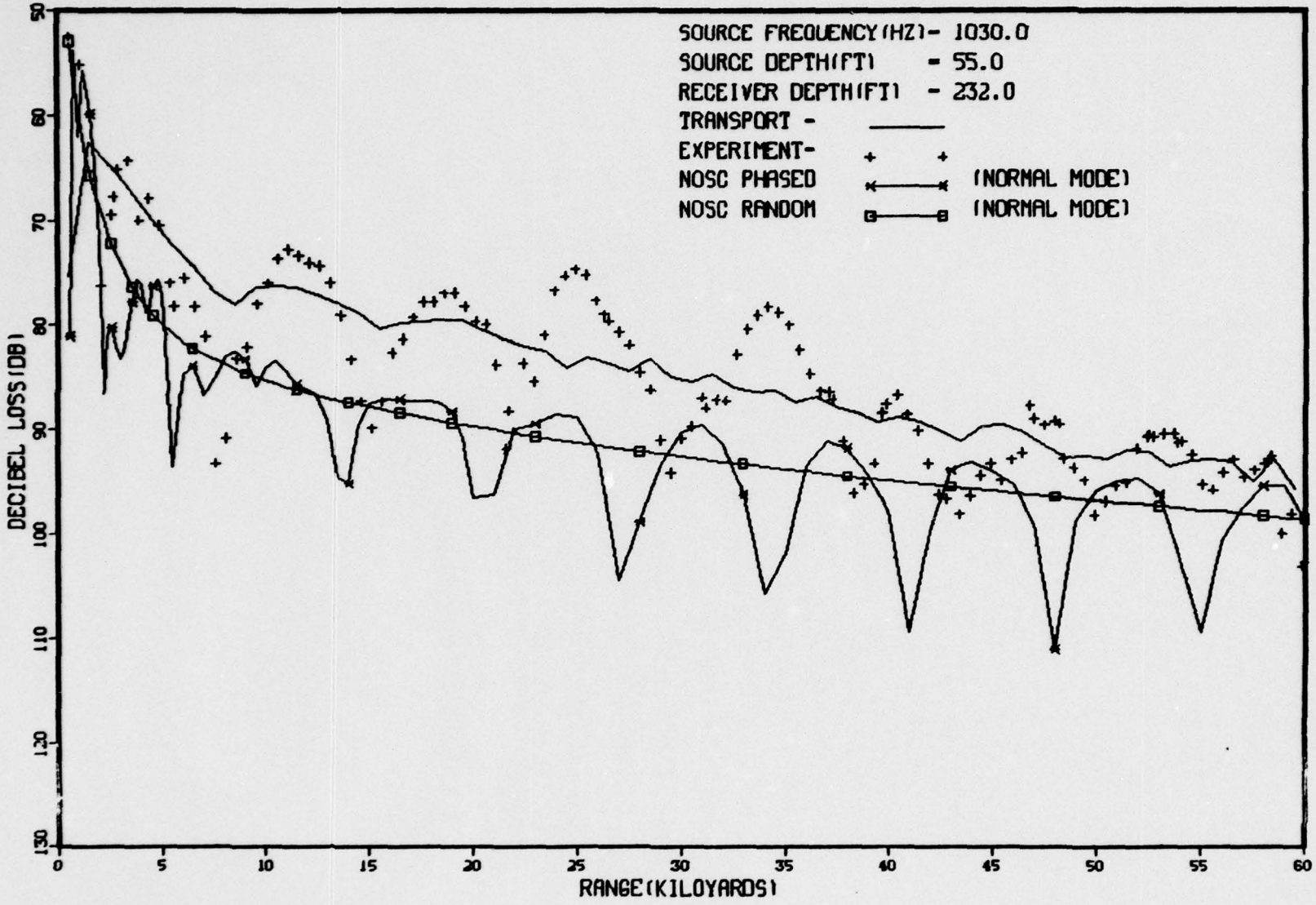

FIG. 4.6 , BILINEAR PROFILE, S-O, INTERNAL WAVE SCATTERING(GENERAL)

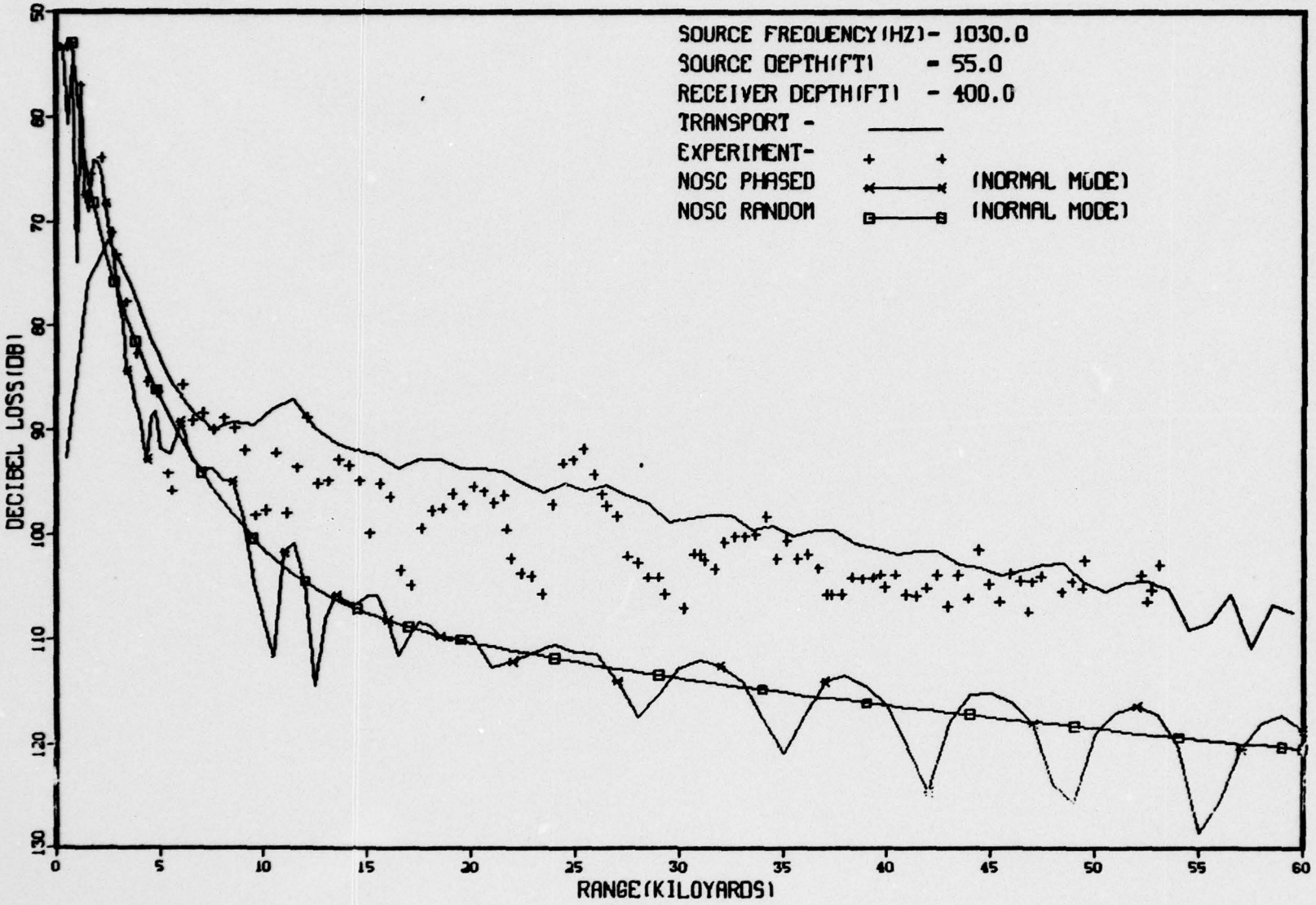

FIG. 4.7 , BILINEAR PROFILE, S-O, INTERNAL WAVE SCATTERING (LINEAR)

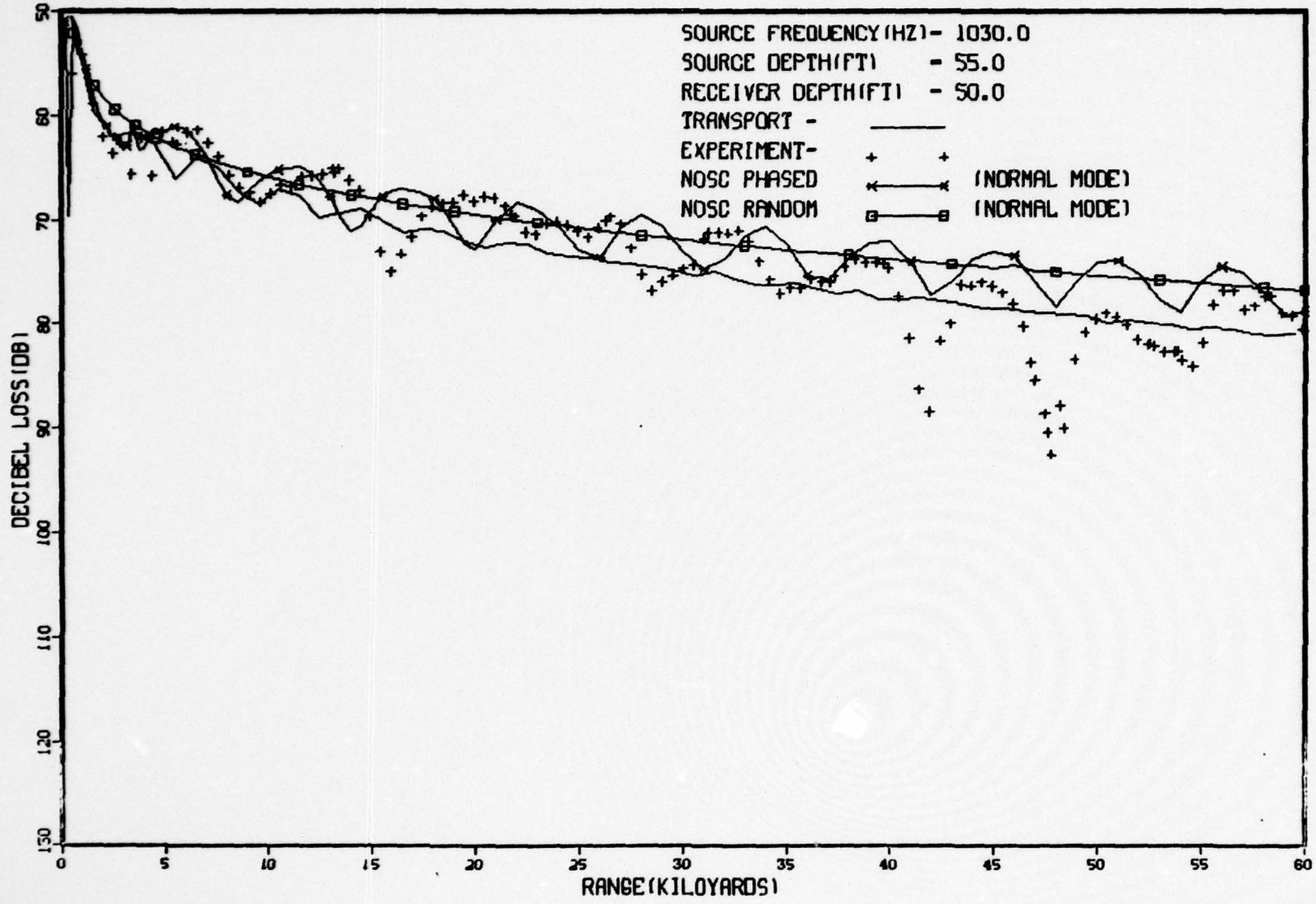

FIG. 4.8 , BILINEAR PROFILE, S-O, INTERNAL WAVE SCATTERING (LINEAR)

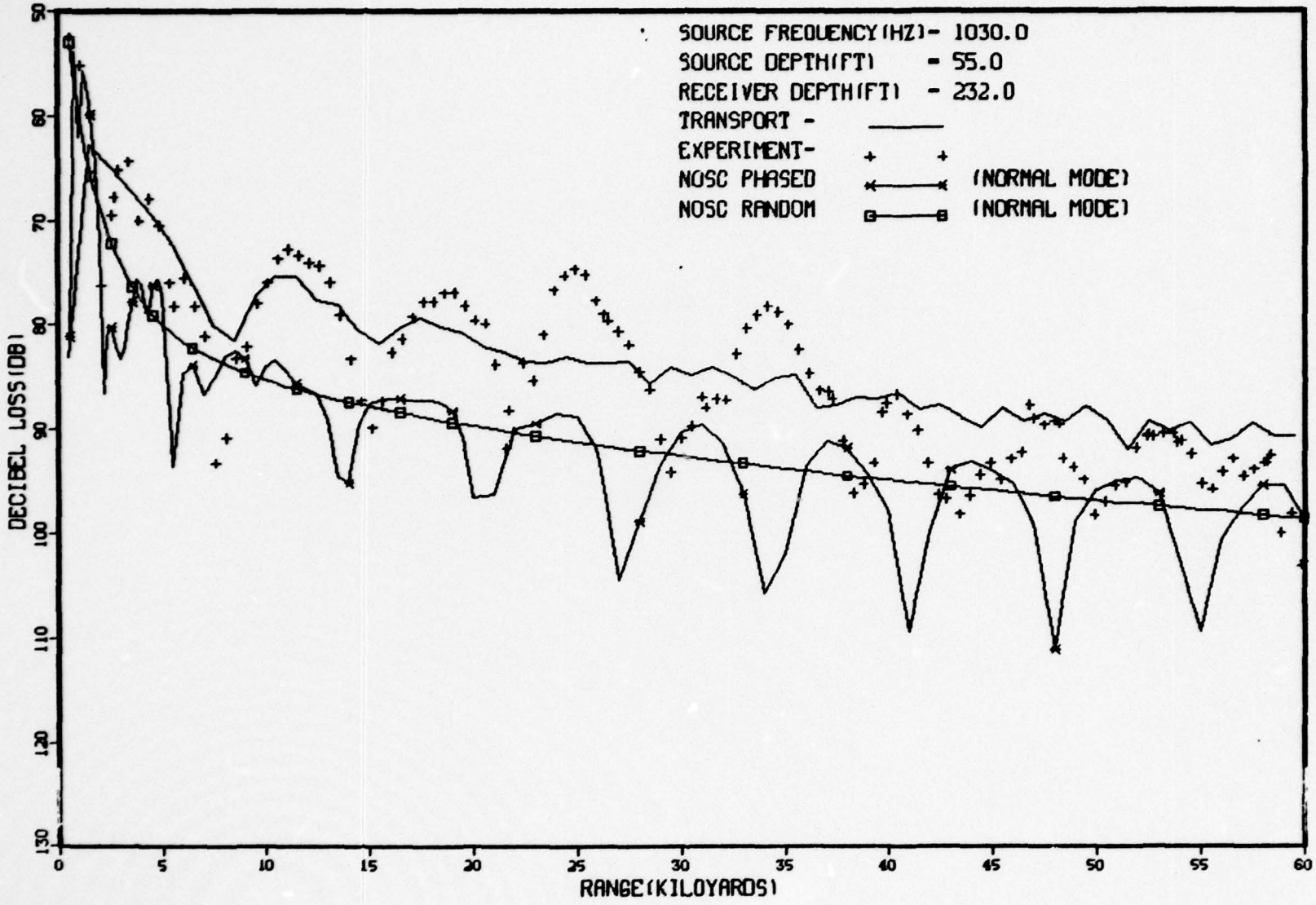

FIG. 4.9 , BILINEAR PROFILE, S-O, INTERNAL WAVE SCATTERING (LINEAR)

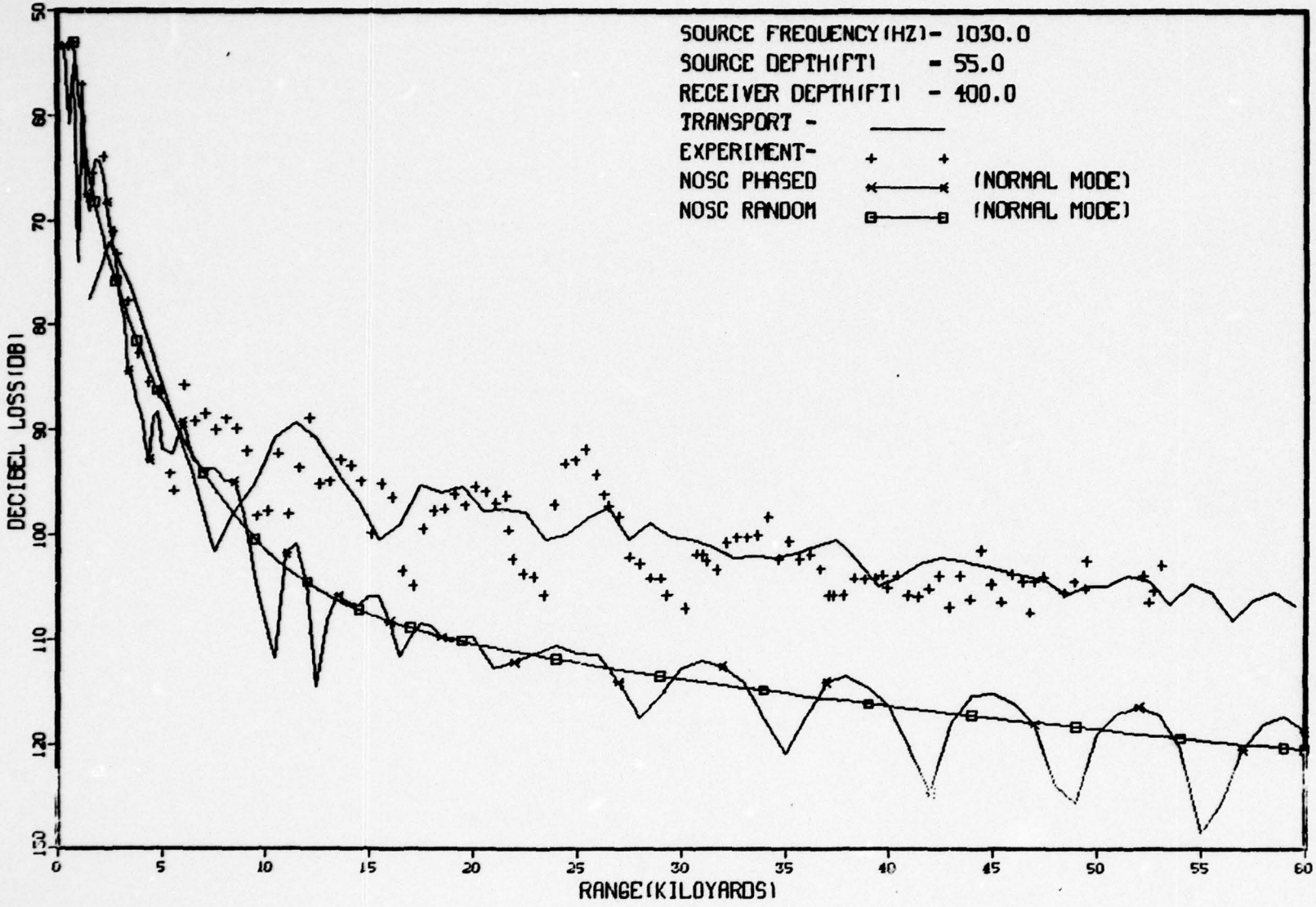

We next checked to see how the transport results would be modified if we switched to the quadratic option, still using $S = 0$. The results are shown in Figures 4.10 - 4.12. The transport results for the 50 foot receiver are raised considerably and now agree almost exactly with the normal mode results. The transport results for the 232 foot receiver (Figure 4.11) are in excellent agreement with the experimental data. Unfortunately, at the 400 foot depth we see from Figure 4.12 that not enough energy is being scattered out of the duct to this below duct receiver. This is rather disappointing in view of the excellent agreement with the experimental data at the other two depths.

The fact that the structure at the 232 foot level was predicted so well in spite of the neglect of diffraction suggested that we should increase the strength of the internal wave scattering by a factor of two. In the duct and near the bottom the scattering model could easily be wrong by such an amount. The results, however, as shown in Figures 4.13 - 4.15 indicate a relatively weak dependence on the magnitude of σ when the quadratic option is used. We note a slight deterioration of the transport results at 232 feet and practically no improvement at the 400 foot depth. The results indicate that a substantial change in the scattering cross section would have to be made within the framework of the quadratic option in order to get the correct amount of scattering below the duct. We would then expect also a further deterioration of the 232 foot results.

With these results in mind we next turned to the case where only surface scattering was used. Several calculations were made but only the results of the best one will be presented. These are contained in Figures 4.16 - 4.18. A similarity is observed between these results and those shown in Figures 4.7 - 4.9 for the case of the linear option with a flat surface. At the 400 foot level (Figure 4.18) we see what appear to be shadow zones in the transport results at about 7 and 14 kyd. This prompted us to combine surface scattering ($S = 0.0025$)

FIG. 4.10, BILINEAR PROFILE, S-O, INTERNAL WAVE SCATTERING(QUADRATIC)

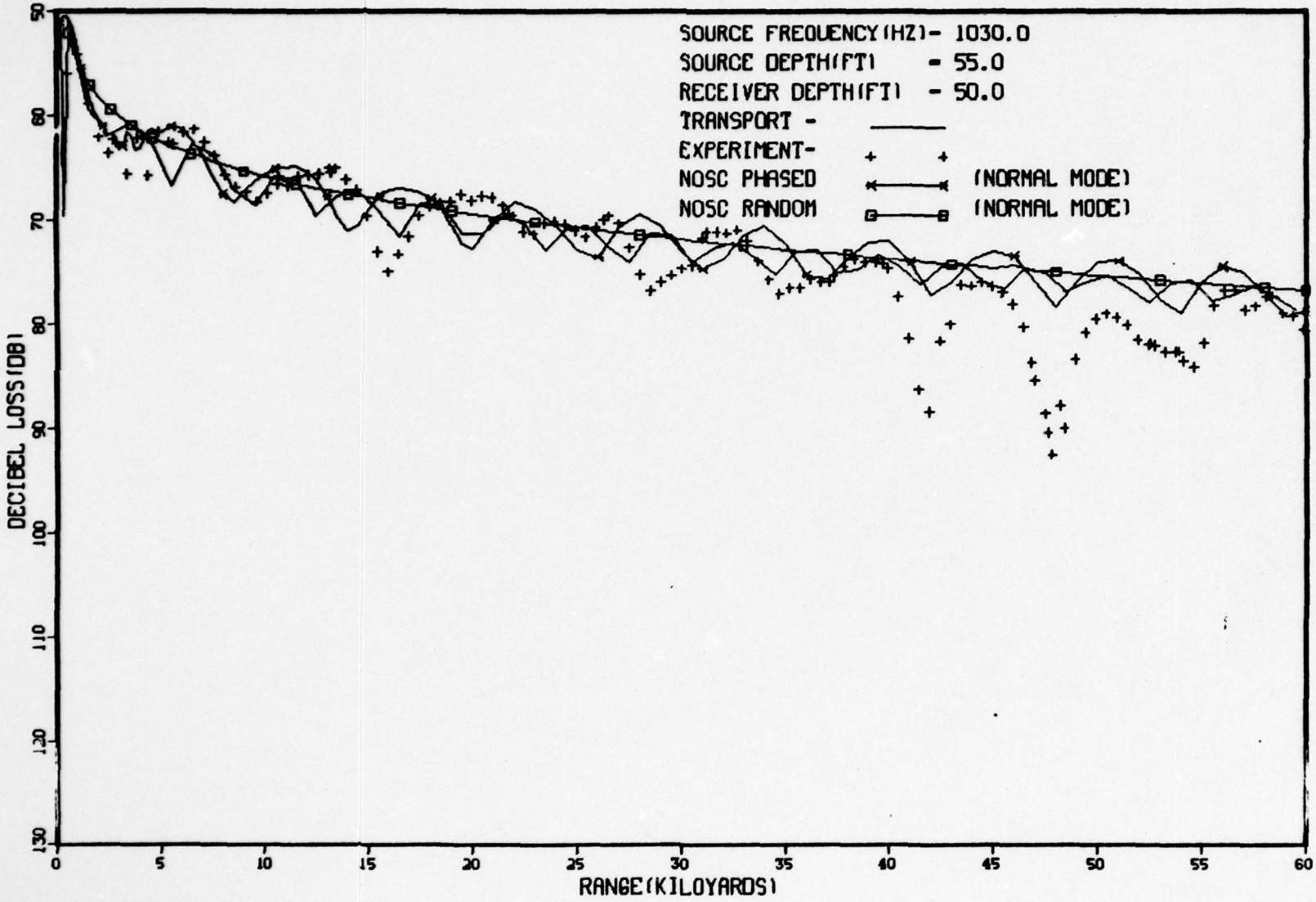

FIG. 4.11, BILINEAR PROFILE, S-O, INTERNAL WAVE SCATTERING(QUADRATIC)

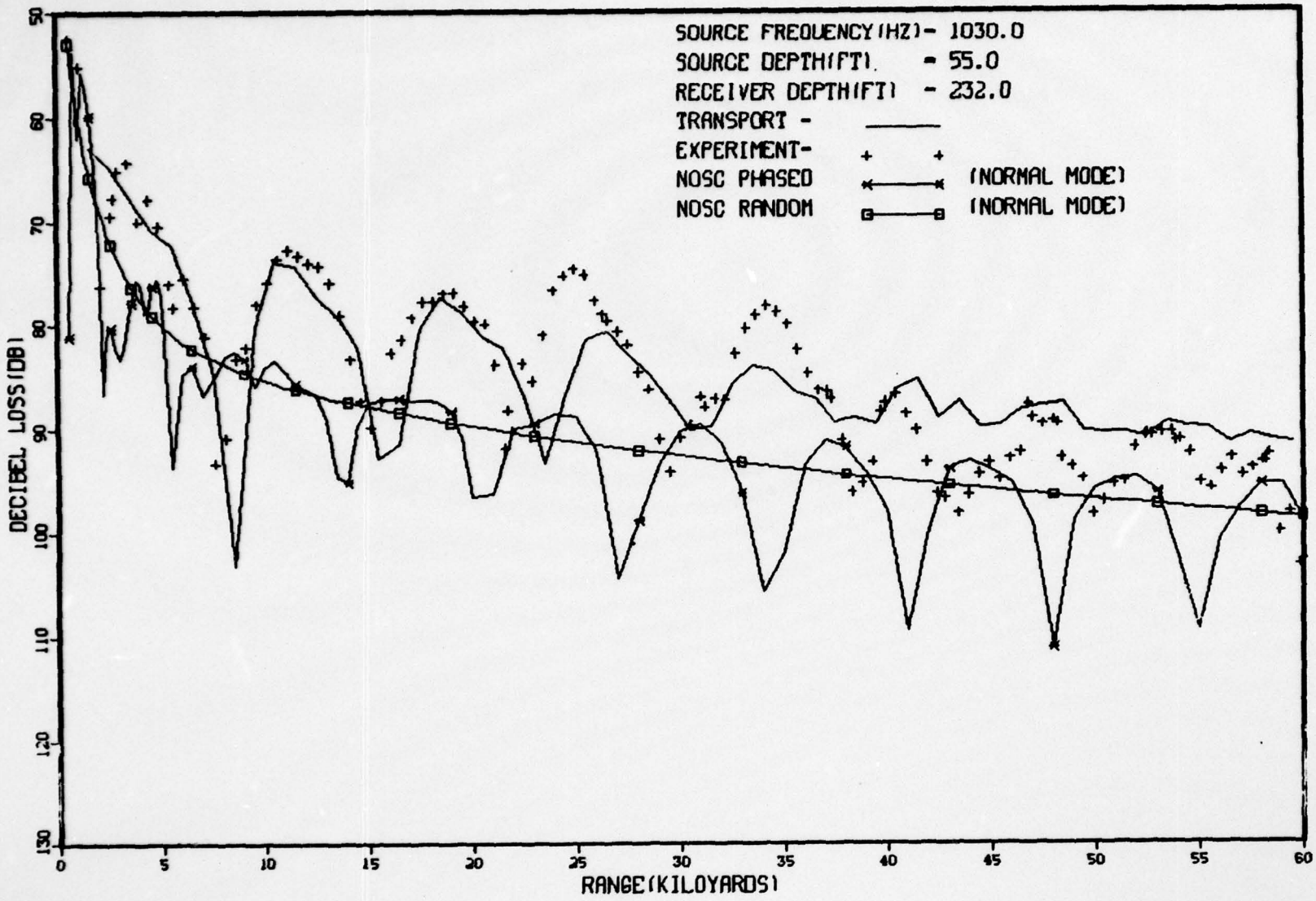

AD-A057 128 SCIENCE APPLICATIONS INC LA JOLLA CALIF F/G 20/1
ACOUSTIC PROPAGATION IN RANDOM OCEANS USING THE TRANSPORT EQUAT--ETC(U)
APR 78 H L WILSON, F D TAPPERT N00014-77-C-0583
UNCLASSIFIED SAI-78-639-LJ NL

2 OF 2
AD
AD57 128

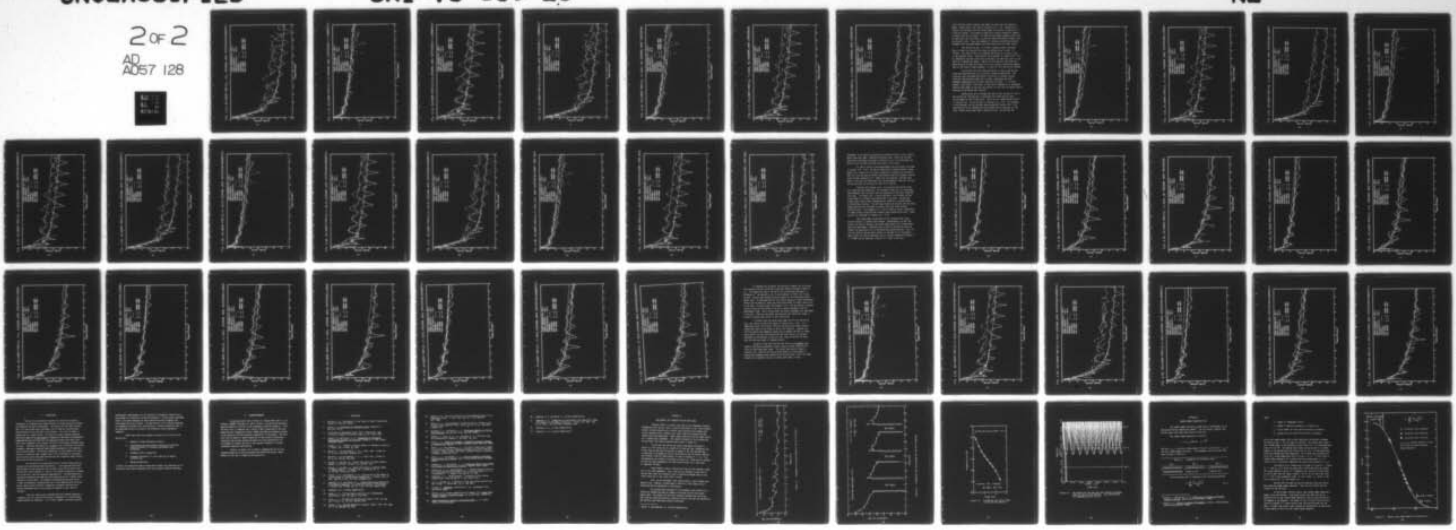

END
DATE
FILMED
9-78
DDC

FIG. 4.12, BILINEAR PROFILE, S-O, INTERNAL WAVE SCATTERING(QUADRATIC)

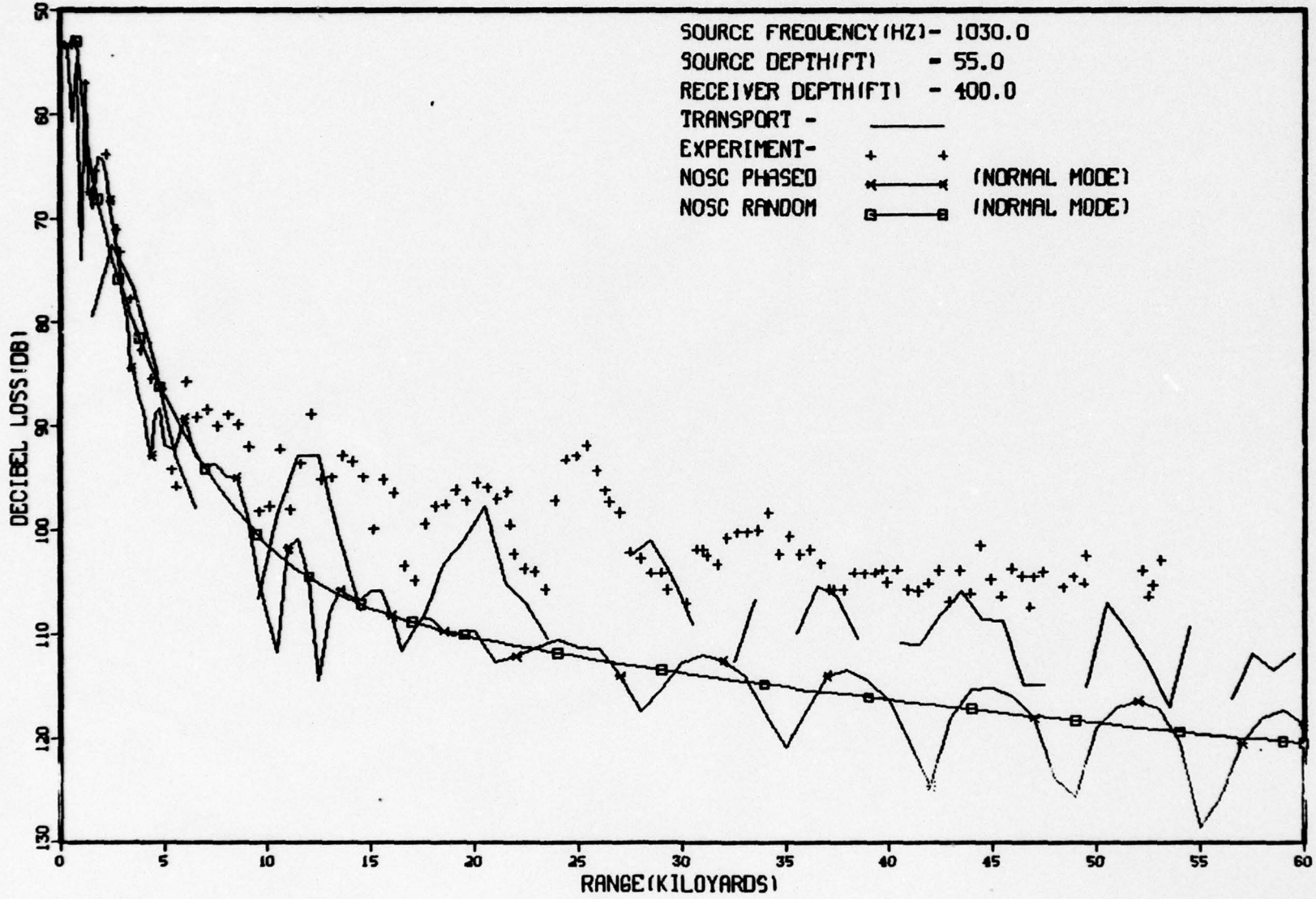

FIG. 4.13, BILINEAR PROFILE, S-O, INTERNAL WAVE SCATTERING (2 X QUADRATIC)

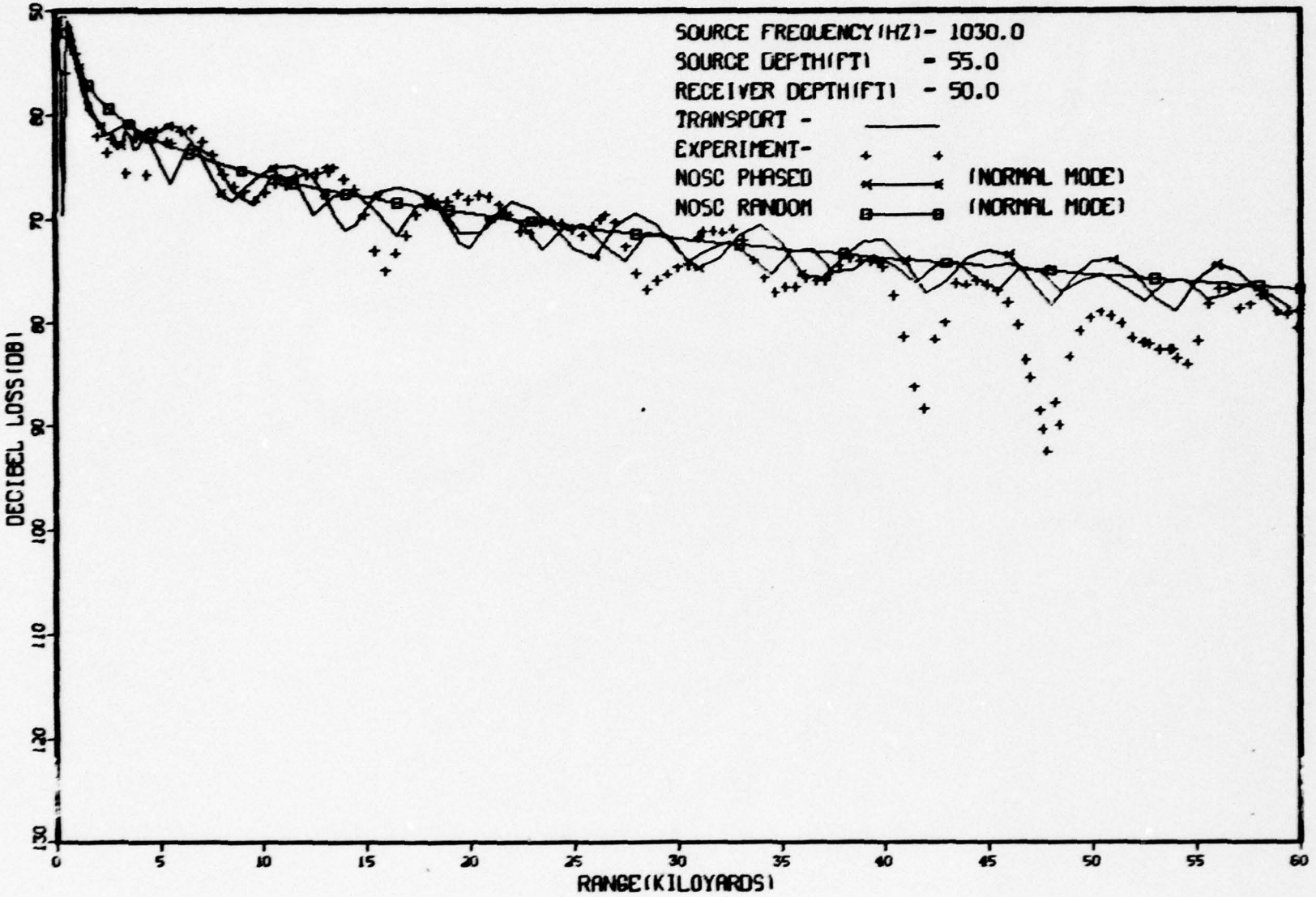

FIG. 4.14, BILINEAR PROFILE, S-0, INTERNAL WAVE SCATTERING (2 X QUADRATIC)

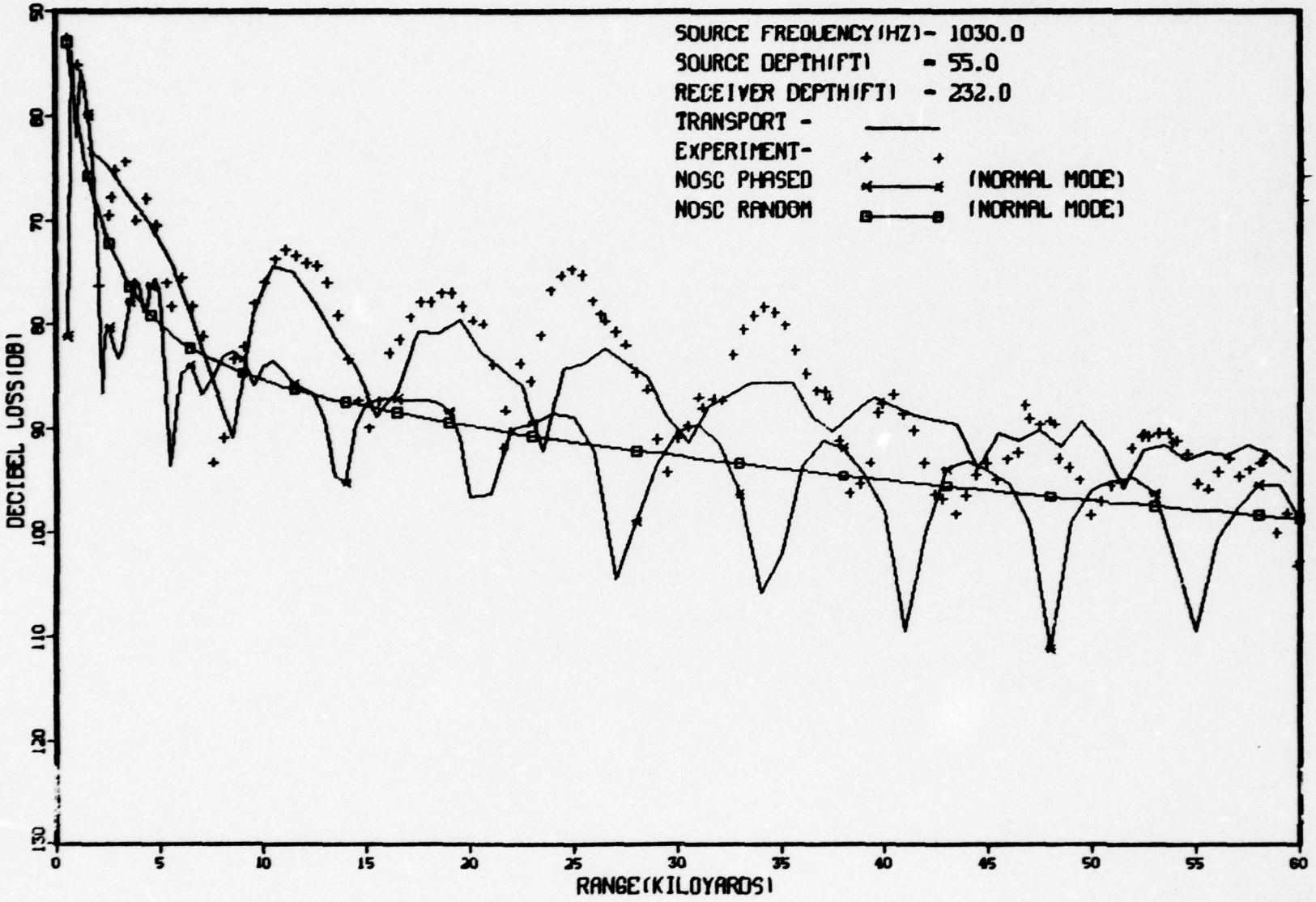

FIG. 4.15, BILINEAR PROFILE, S-O, INTERNAL WAVE SCATTERING (2 X QUADRATIC)

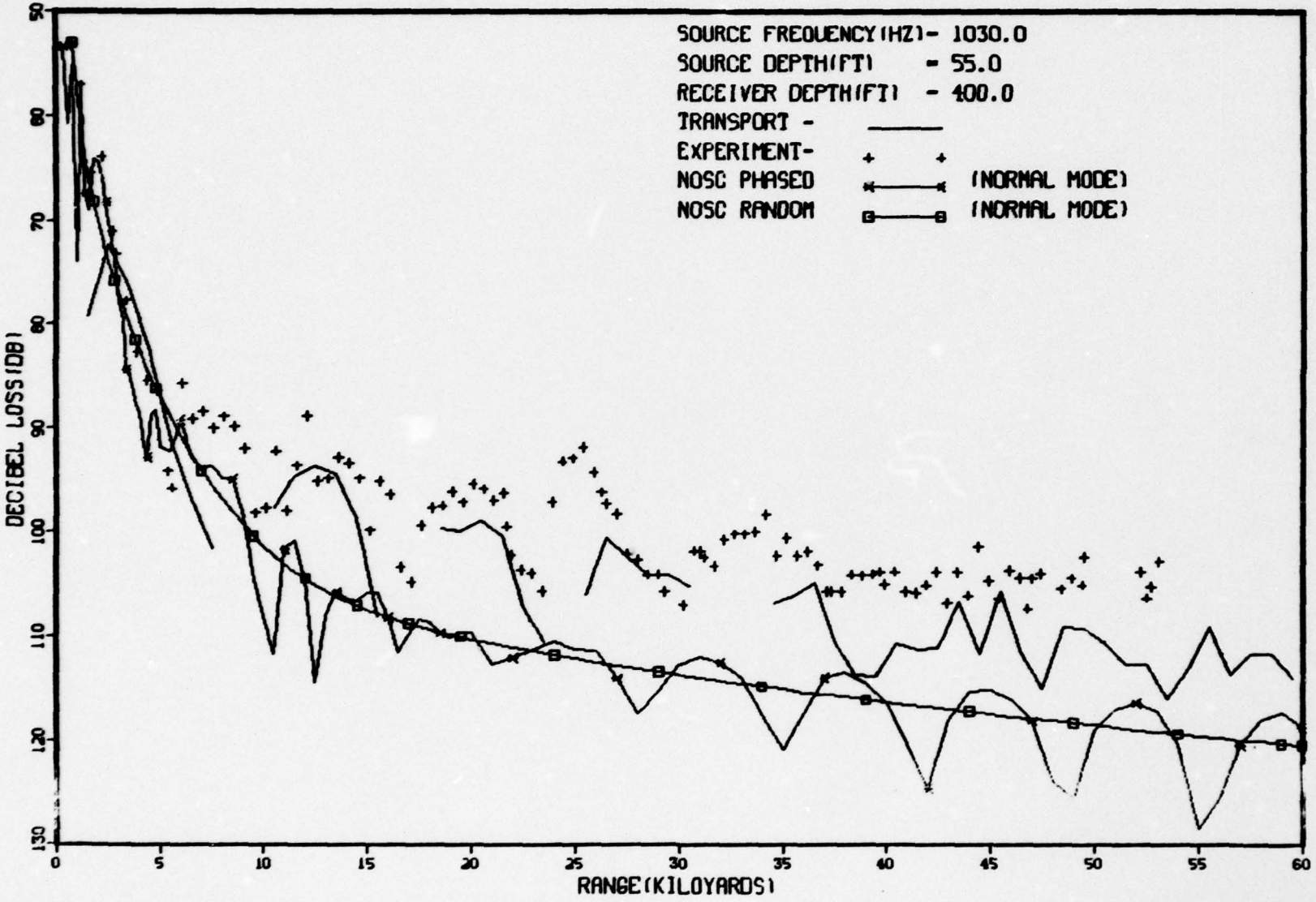

FIG. 4.16, BILINEAR PROFILE, S-.0025, NO INTERNAL WAVE SCATTERING

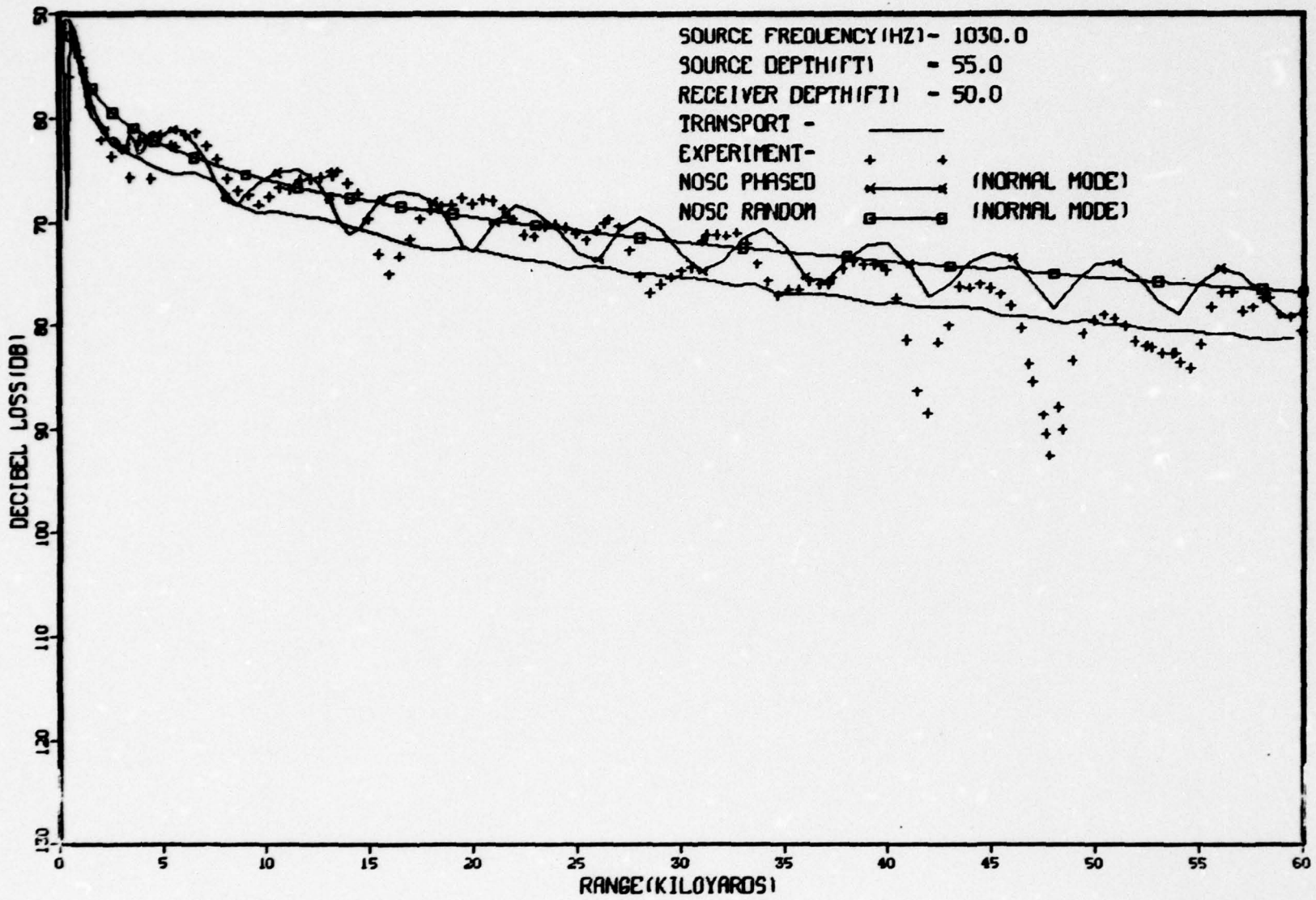

FIG. 4.17, BILINEAR PROFILE, S-.0025, NO INTERNAL WAVE SCATTERING

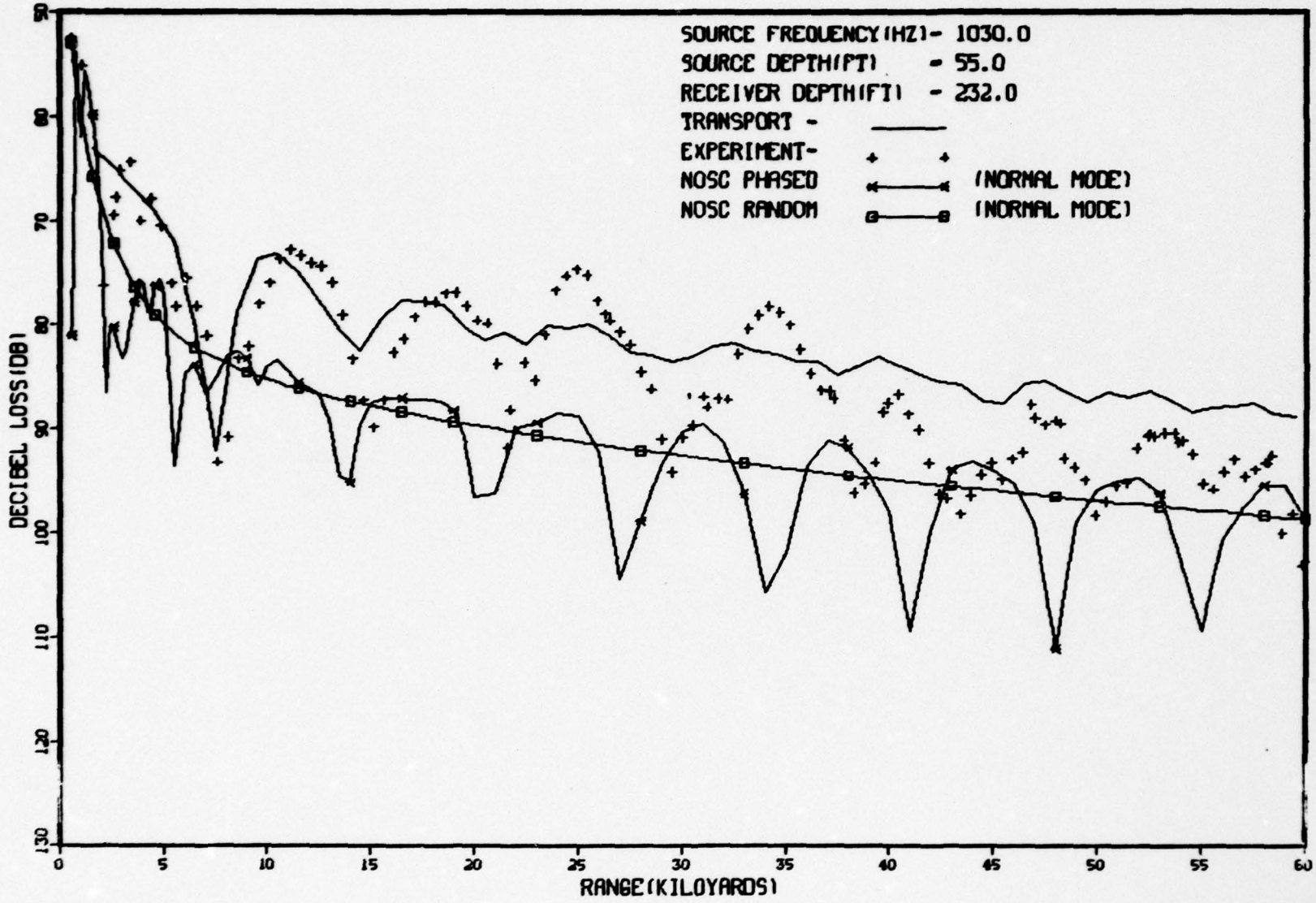

FIG. 4.18, BILINEAR PROFILE, S=.0025, NO INTERNAL WAVE SCATTERING

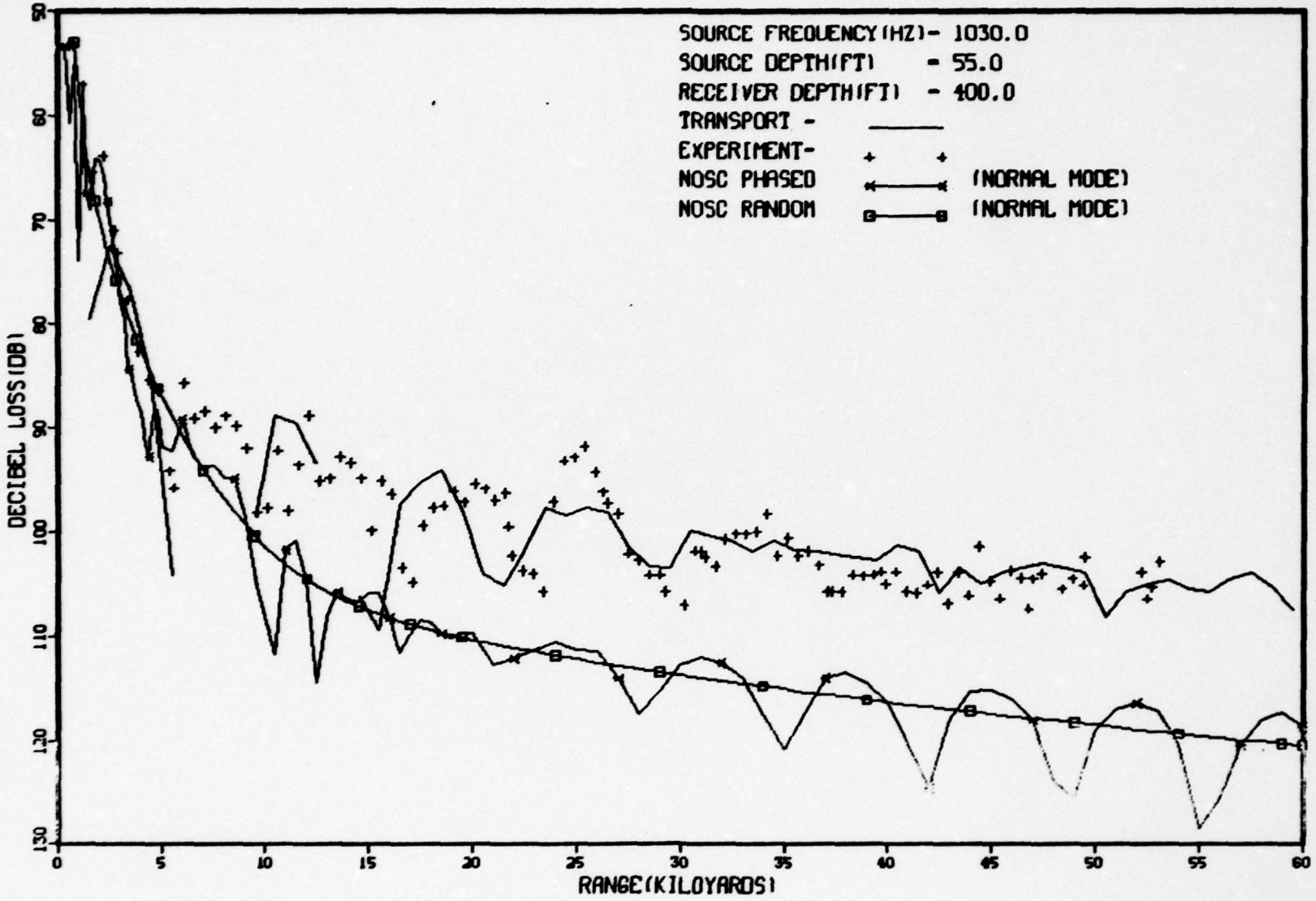

first with the linear internal wave model and then with the quadratic model. These results are given in Figures 4.19 - 4.24. Observation of Figure 4.21 indicates that the linear model with surface scattering is a little too strong. The quadratic model with surface scattering, however, is about right at all levels. It might be considered somewhat low at the 50 foot level, but this level is such that mode interference effects could be playing a role. Thus, less emphasis is placed on achieving accurate agreement with the experimental data here than at the two lower levels.

The results for the $S = 0.0025$ quadratic model indicated that, at least as a sensitivity check, we should rerun it with $S = 0.00125$. This would allow us to examine the effect of a factor of two in the sawtooth slope. These results are presented in Figures 4.25 - 4.27. We immediately see that the energy scattered to the 400 foot level is too small by a substantial amount. Hence, we conclude that the below duct ensonification is much more sensitive to the surface scattering parameter than to the internal wave parameter, at least for this particular problem.

We are thus left with some uncertainty in how to ascribe the below duct ensonification to the various scattering mechanisms. The situation could have been more easily clarified if accurate surface condition data had been taken and if better range-depth and time-dependent temperature and salinity data were available. It is clear, however, that either a very small surface swell component or a reasonable internal wave model in the duct can account for the level on ensonification measured at the below-layer receiver.

Before going on to consider the 530 Hz data, we want to look at the statistical fluctuations in the Monte Carlo data due to using a finite number of rays or particles. We do this by comparing the results in Figures 4.28 - 4.30 with those in Figures 4.22 - 4.24. As indicated in the captions, the calculation used to generate Figures 4.28 - 4.30 used 7000 particles, whereas the calculations used to generate all the other figures used either 3000 or 4000 particles. We see that the

FIG. 4.19, BILINEAR PROFILE, S-.0025, INTERNAL WAVE SCATTERING(LINEAR)

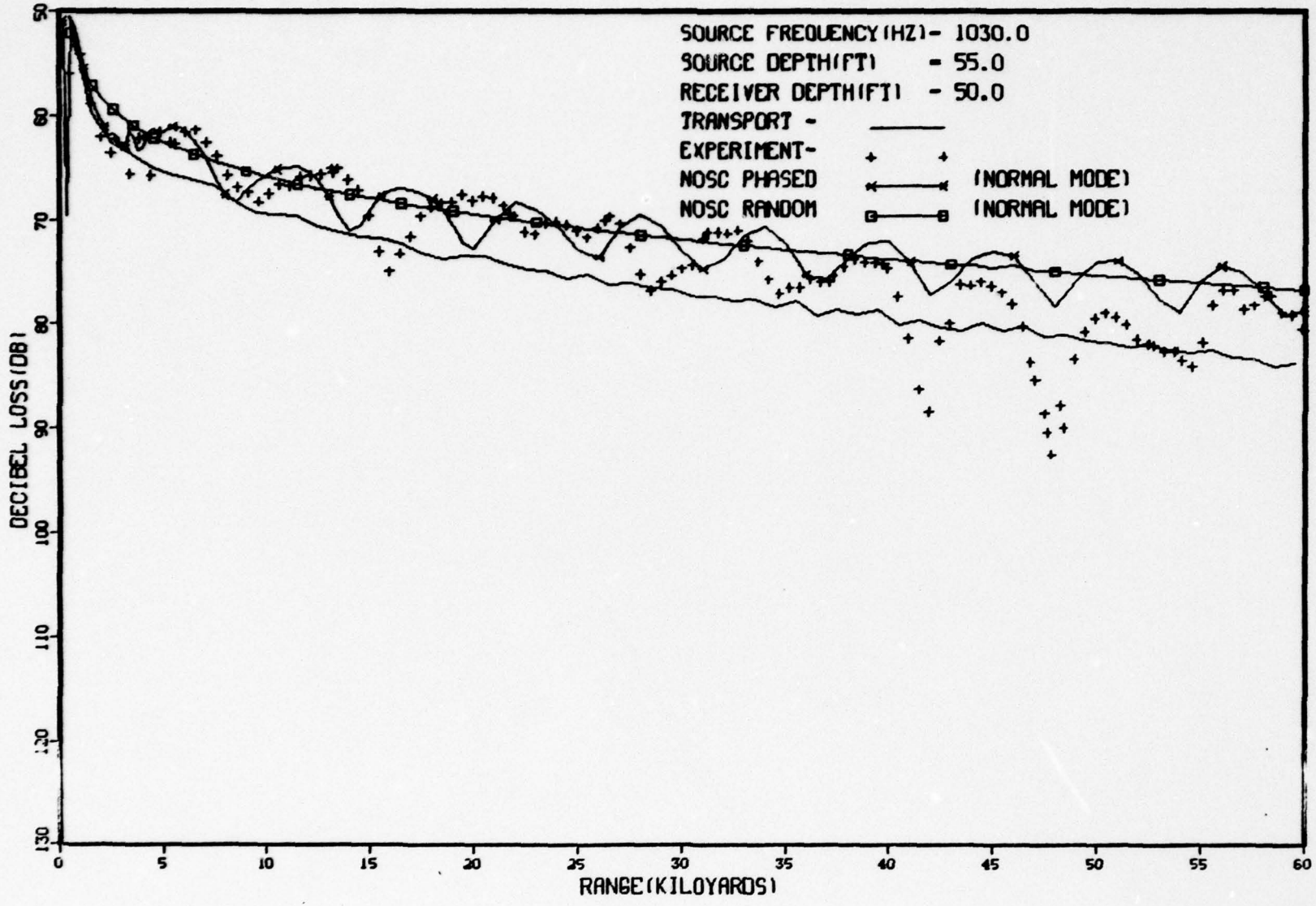

FIG. 4.20, BILINEAR PROFILE, S-.0025, INTERNAL WAVE SCATTERING(LINEAR)

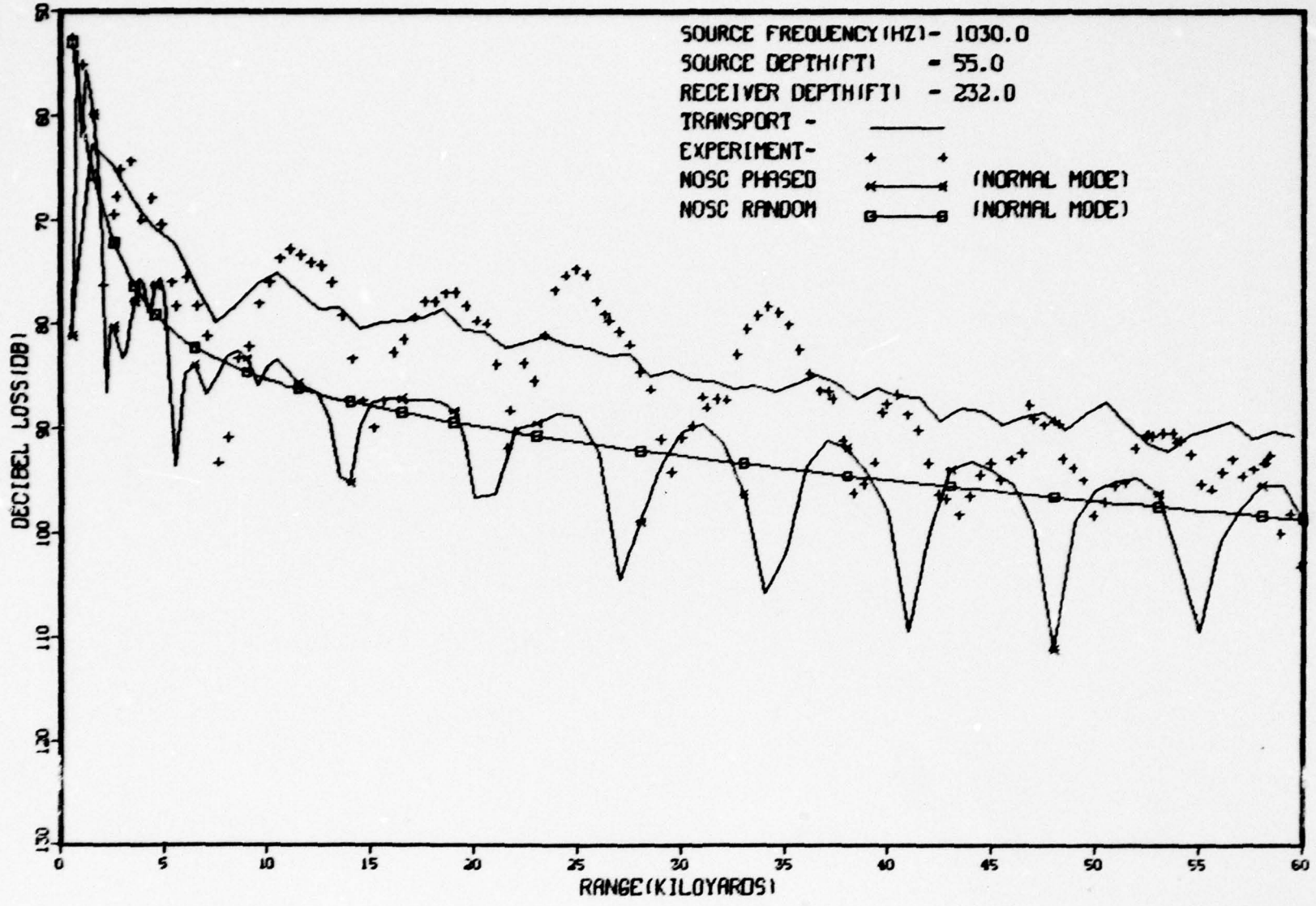

FIG. 4.21, BILINEAR PROFILE, S-.0025, INTERNAL WAVE SCATTERING(LINEAR)

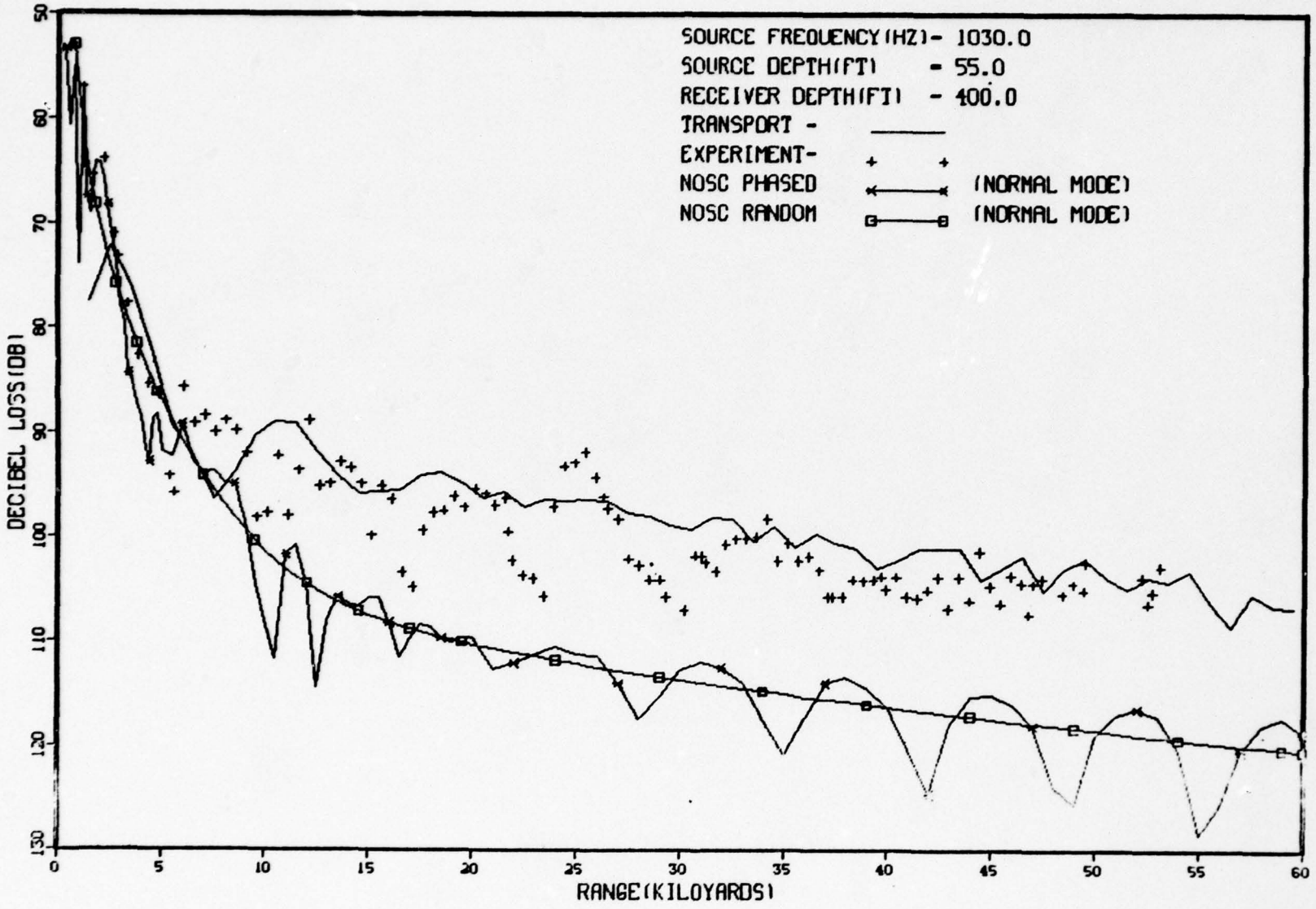

FIG. 4.22, BILINEAR PROFILE, S-.0025, INTERNAL WAVE SCATTERING(QUADRATIC)

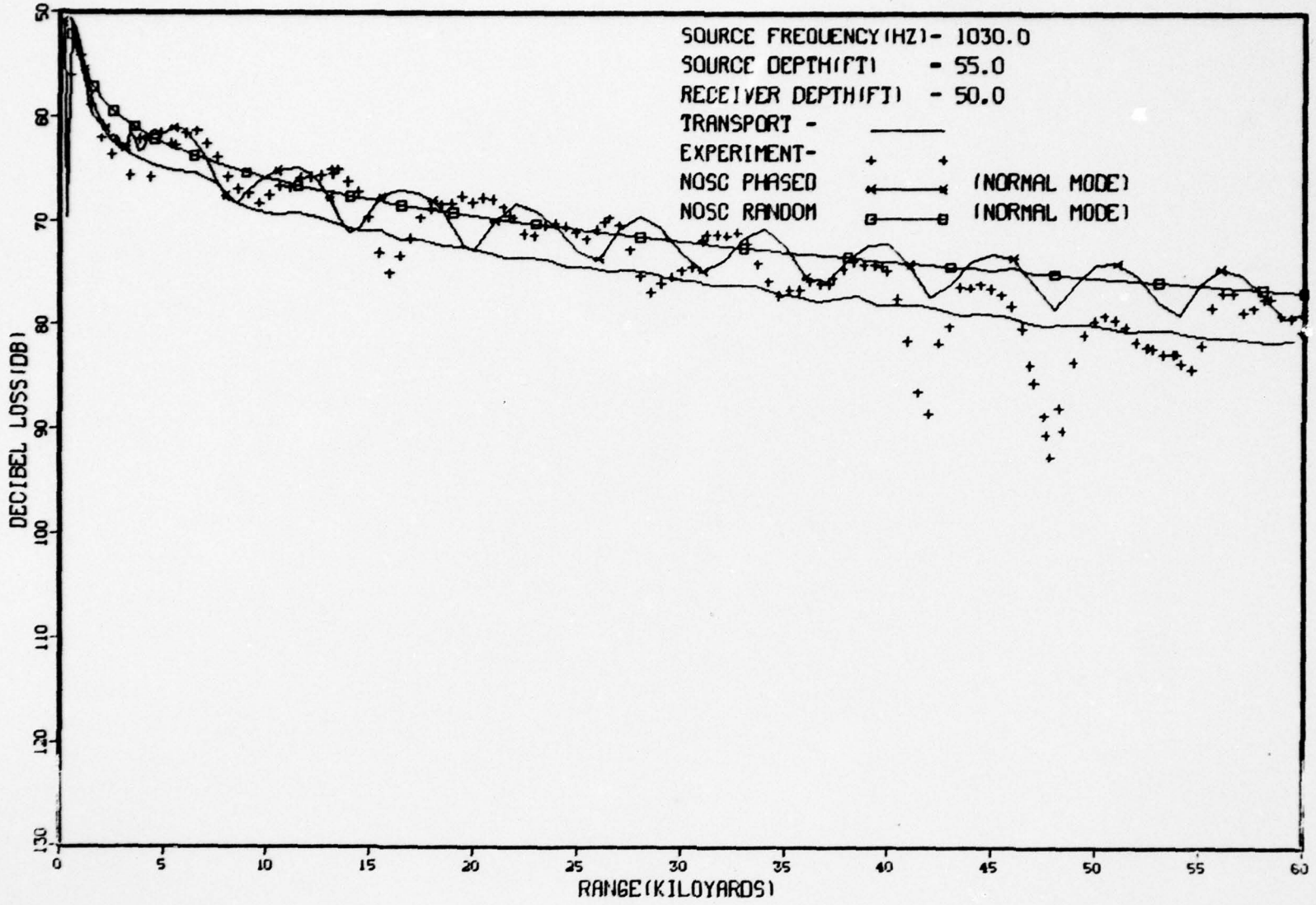

FIG. 4.23, BILINEAR PROFILE, S=.0025, INTERNAL WAVE SCATTERING(QUADRATIC)

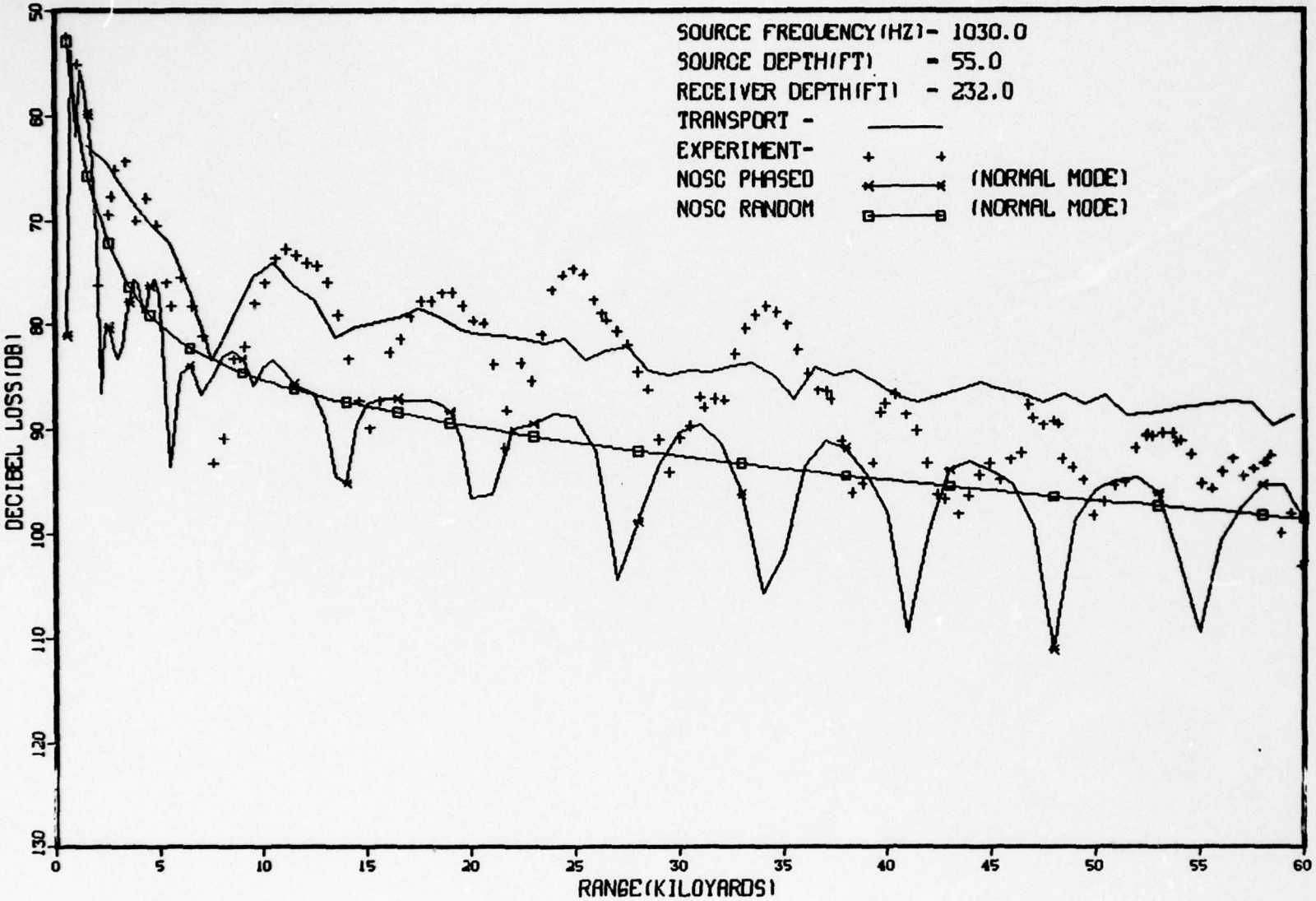

FIG. 4.24, BILINEAR PROFILE, S=.0025, INTERNAL WAVE SCATTERING(QUADRATIC)

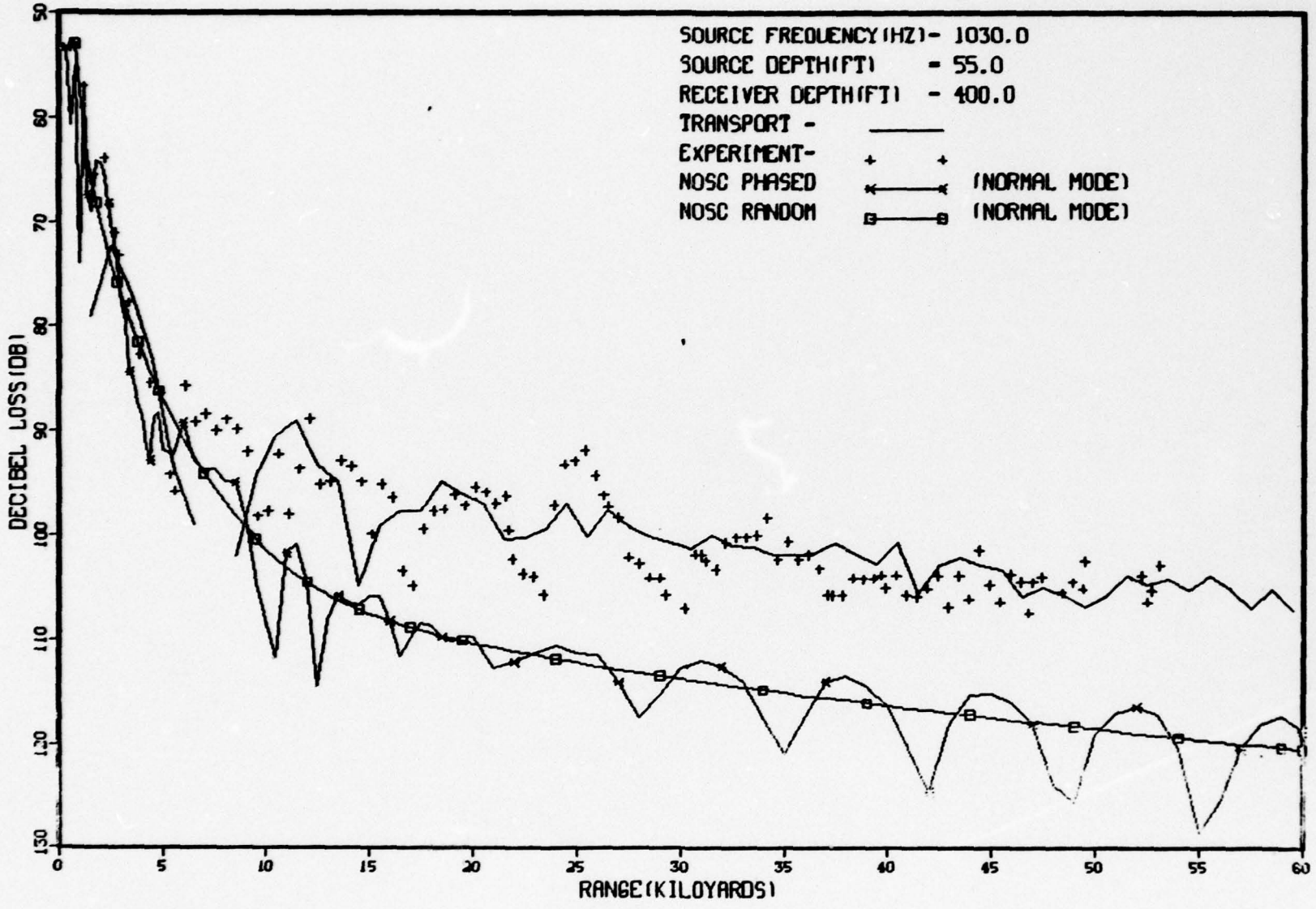

FIG. 4.25, BILINEAR PROFILE, S=.00125, INTERNAL WAVE SCATTERING (QUADRATIC)

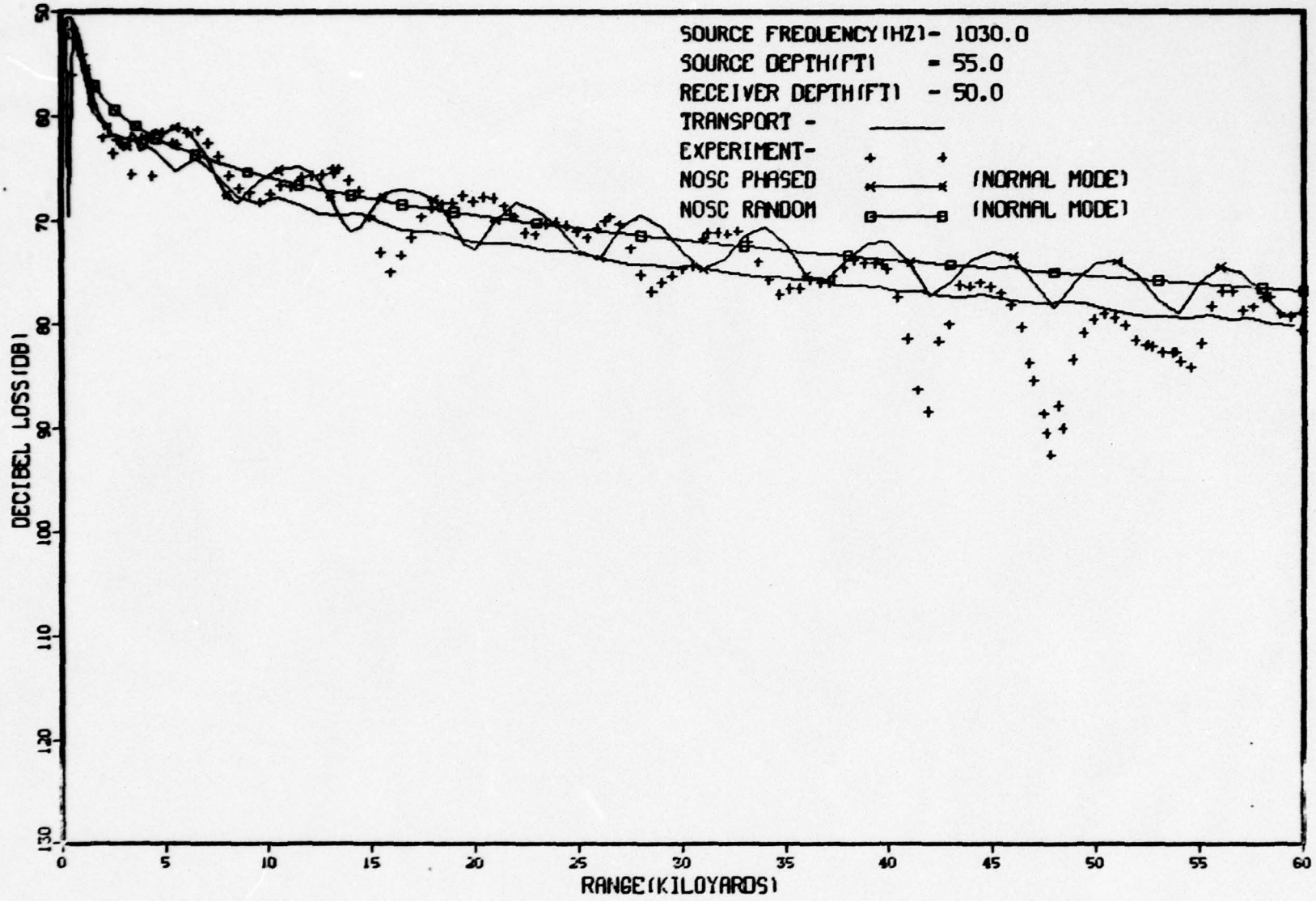

FIG. 4.26, BILINEAR PROFILE, S-.00125, INTERNAL WAVE SCATTERING(QUADRATIC)

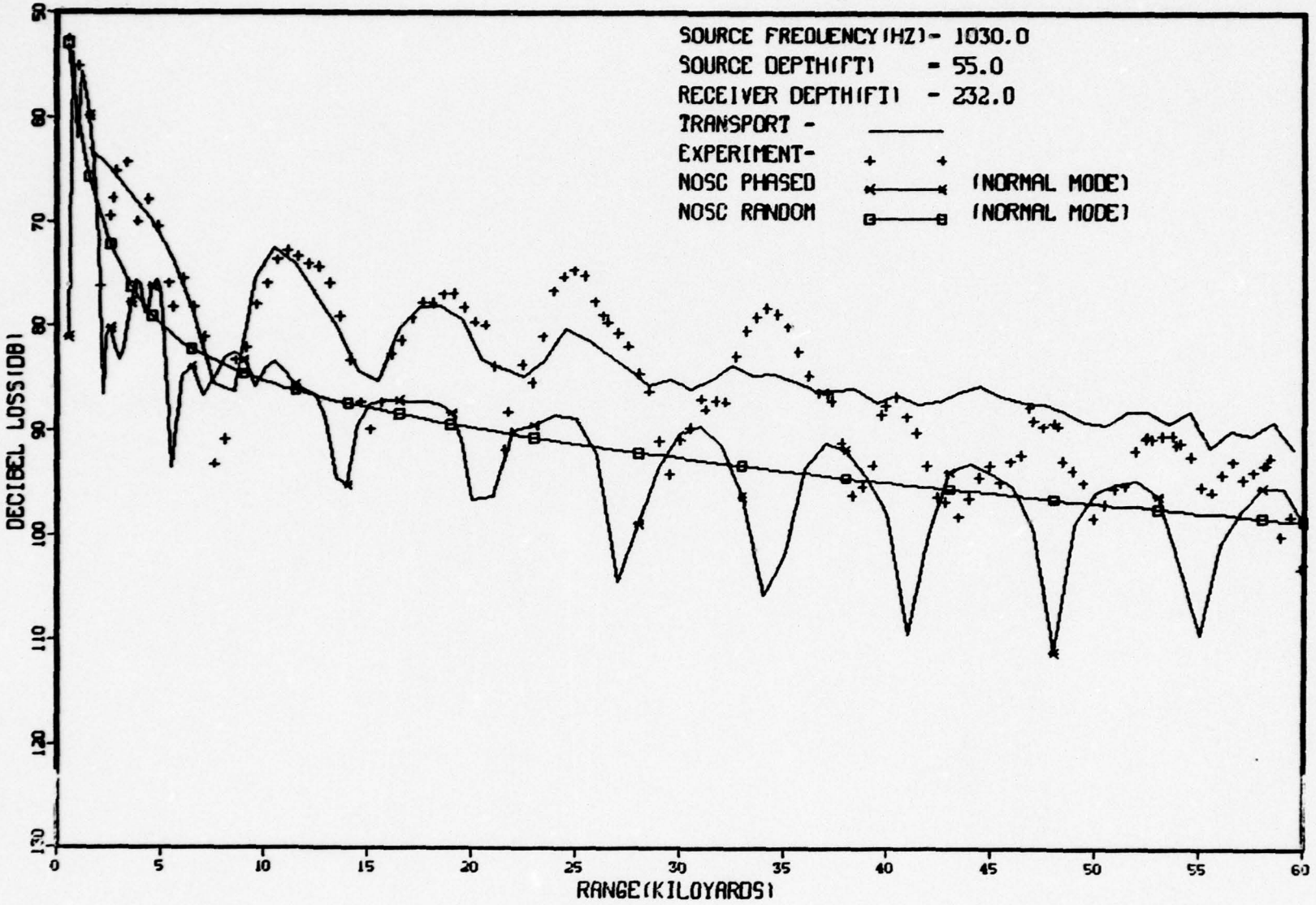

FIG. 4.27, BILINEAR PROFILE, S=.00125, INTERNAL WAVE SCATTERING (QUADRATIC)

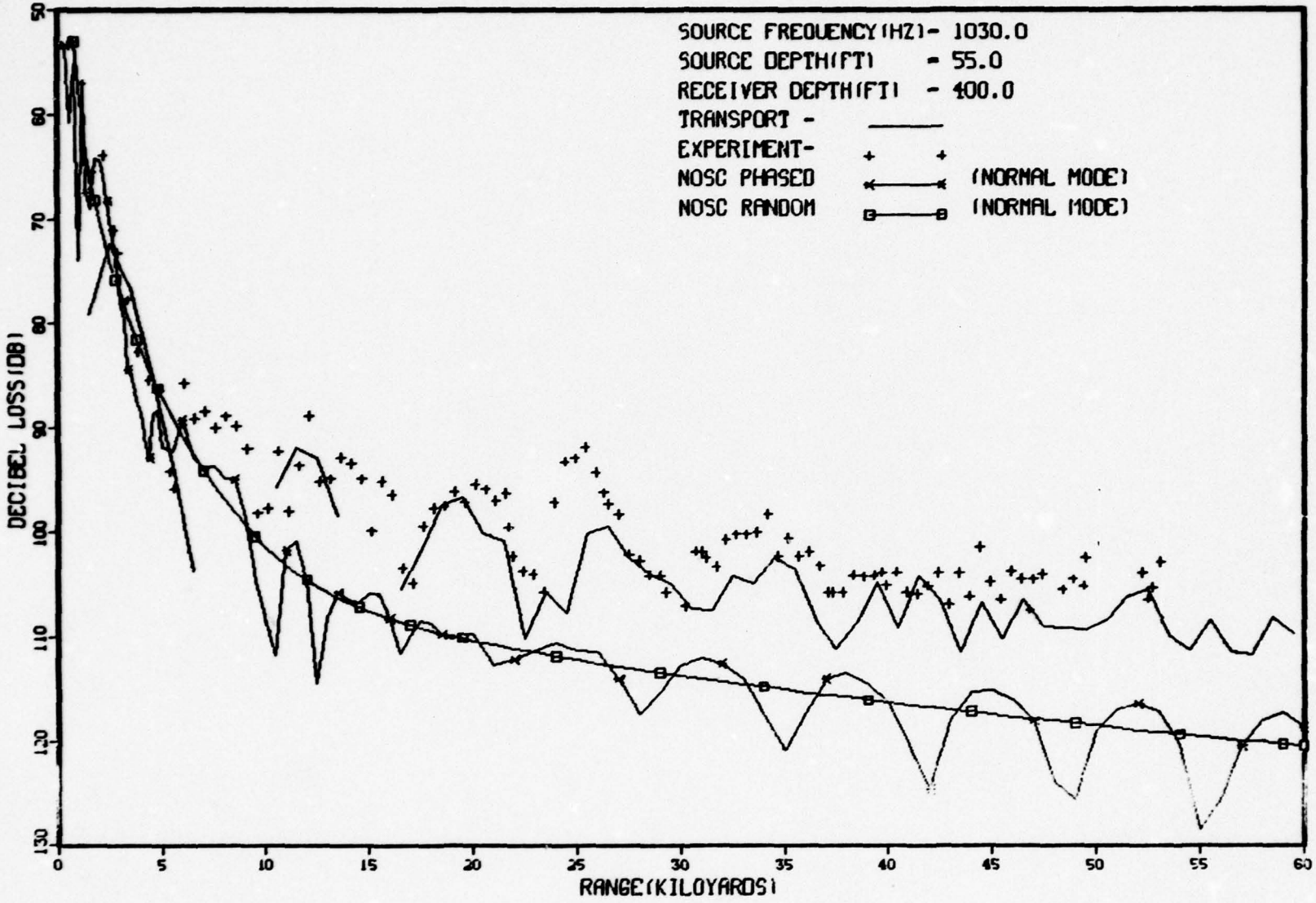

FIG. 4.28, BILINEAR PROFILE, S-.0025, INT. WAVE SCATTERING(QUAD) 7000 RAYS

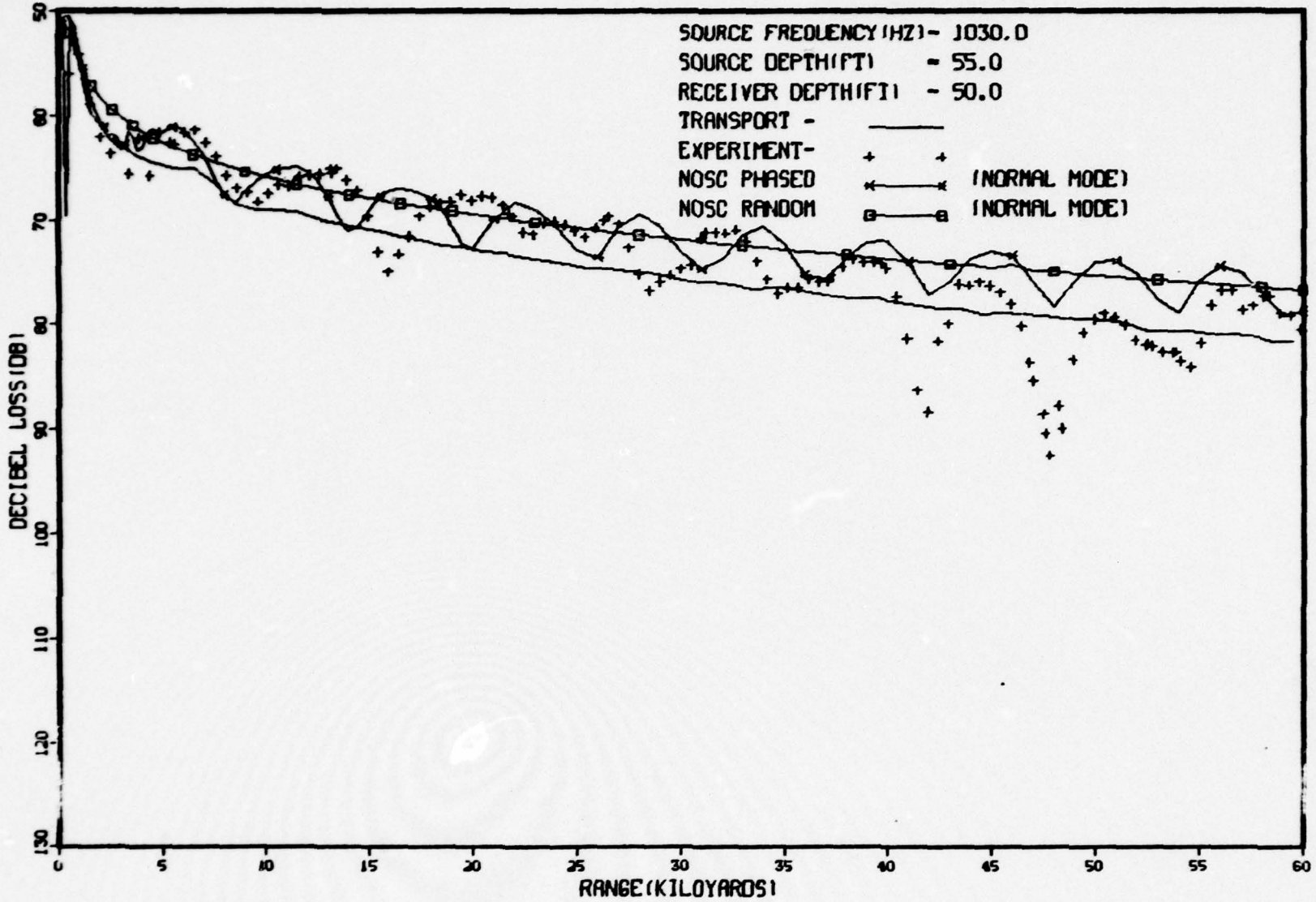

FIG. 4.29, BILINEAR PROFILE, S-.0025, INT. WAVE SCATTERING(QUAD) 7000 RAYS

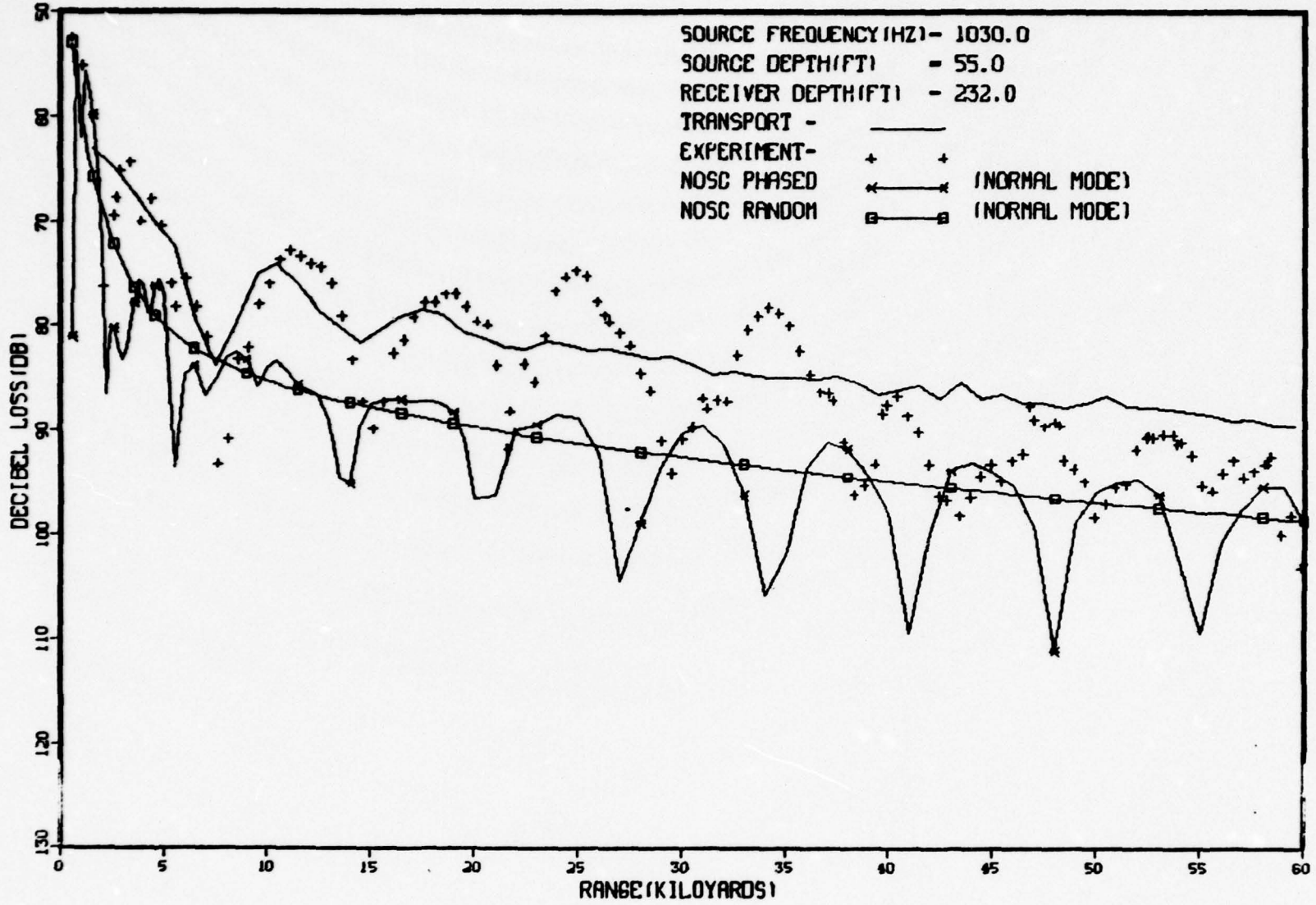

FIG. 4.30, BILINEAR PROFILE, S-.0025, INT. WAVE SCATTERING(QUAD) 7000 RAYS

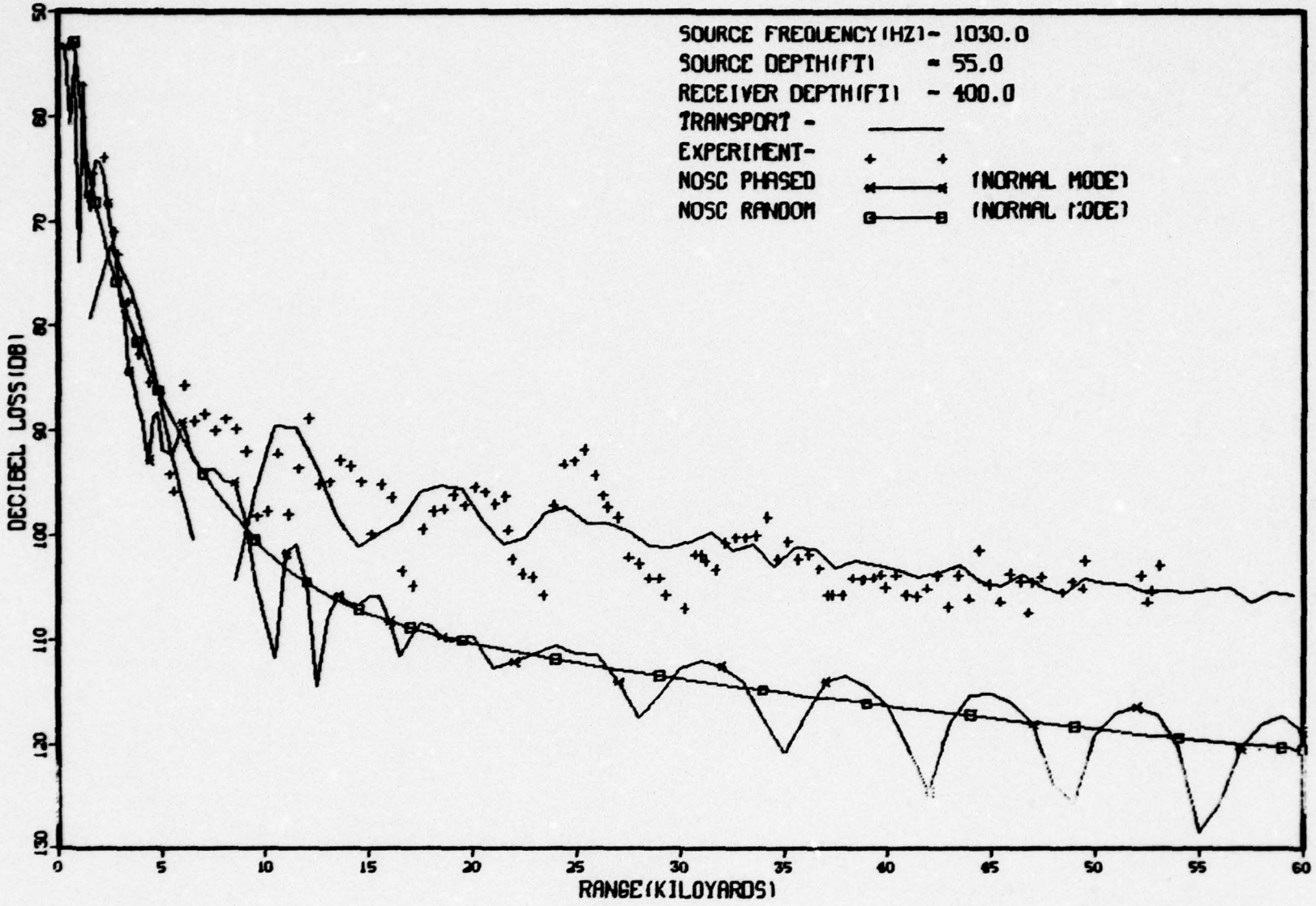

smoothness in the results obtained using 7000 particles is only slightly better than when 3000 - 4000 particles were used. After the variance calculation technique (discussed in Section 2.3.3) is incorporated into ACTOR, we will be able to place error bars on the curves.

The 530 Hz results, both experimental and calculated, are shown in Figures 4.31 - 4.42. At 530 Hz scattering by internal waves is much weaker (by a factor of four) than at 1030 Hz, so essentially the 530 Hz data will only be used as further confirmation that the transport results using surface scattering (S = .0025) with the quadratic internal wave model in the duct are consistent with the experimental data and, in fact, provide the best fit at 530 Hz as well as at 1030 Hz.

Starting with Figures 4.31 - 4.33 we have the results using only rough surface scattering. The transport results are in reasonably good agreement with the data, with the exception of the short range 400 foot case. In Figures 4.34 - 4.36 we consider a flat surface and the linear model for internal wave scattering in the duct. We see that without some rough surface scattering the intensity is overestimated at the 50 foot receiver. The 232 foot results are not bad, and the short range predictions at 400 feet are better than with rough surface scattering only. This suggests, as it did at 1030 Hz, that a combination of rough surface scattering and internal wave scattering be used. These results are displayed in Figures 4.37 - 4.42.

The normal mode calculations do not include either rough surface effects or internal wave effects. Nevertheless, we see from Figure 4.39 that at 400 feet the normal mode results are in good agreement with experiment, indicating that at 530 Hz diffraction alone can account for essentially all of the below-duct ensonification. Thus, as with the 1030 Hz case we again select, as the best fit to the experimental data, the results obtained using a surface roughness parameter of S = 0.0025 and the quadratic internal wave model in the duct.

FIG. 4.31, BILINEAR PROFILE, S-.0025, NO INTERNAL WAVE SCATTERING

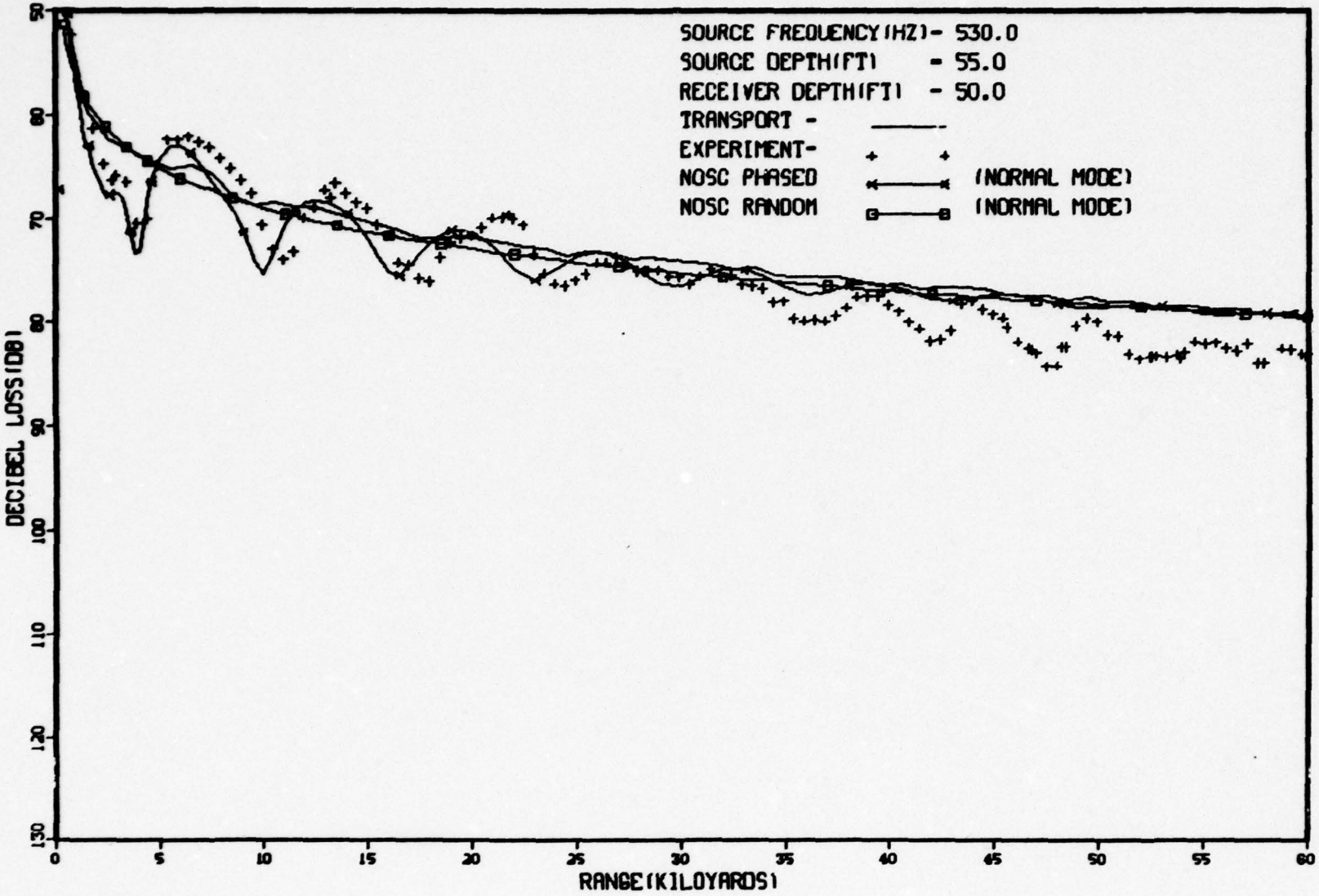

FIG. 4.32, BILINEAR PROFILE, S=.0025, NO INTERNAL WAVE SCATTERING

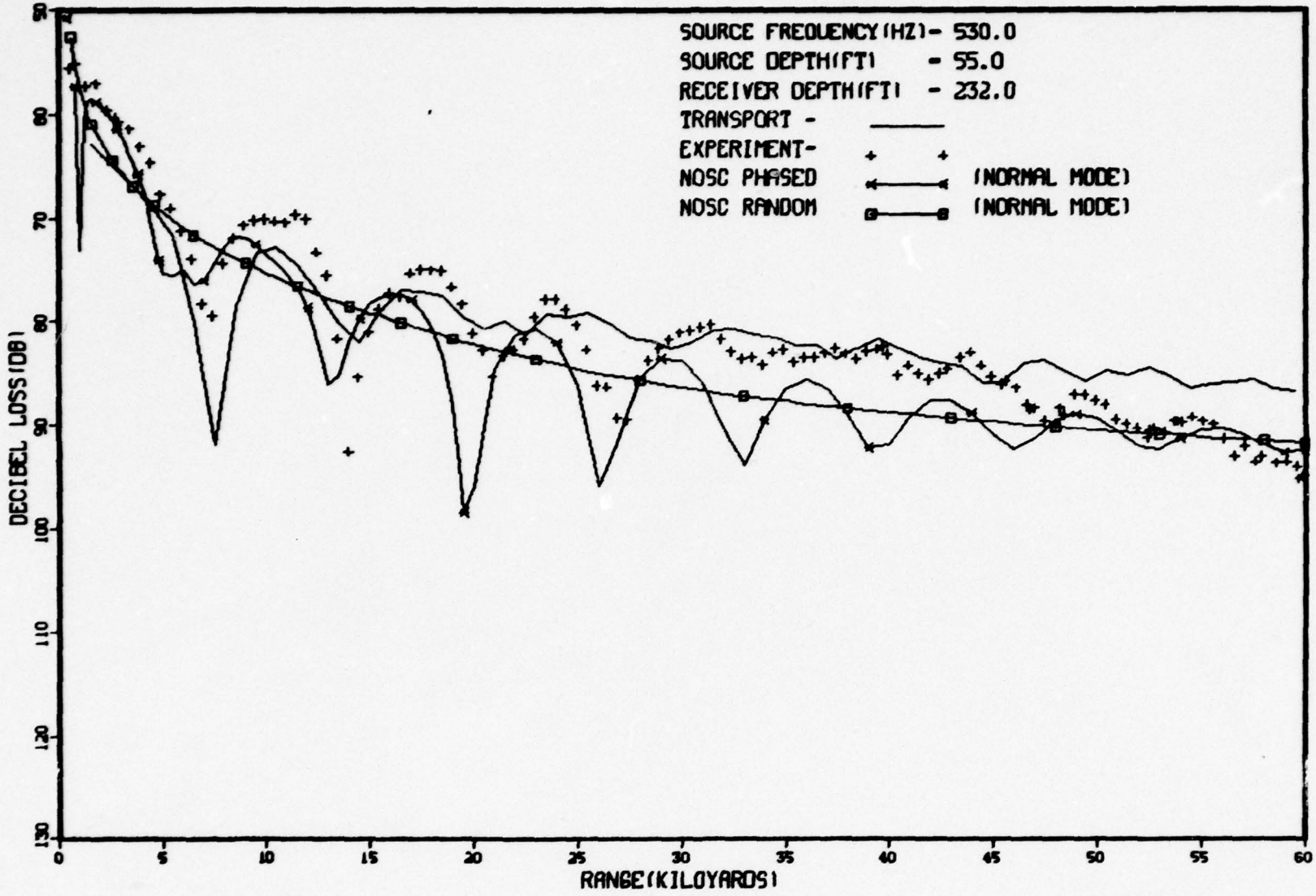

FIG. 4.33, BILINEAR PROFILE, S-.0025, NO INTERNAL WAVE SCATTERING

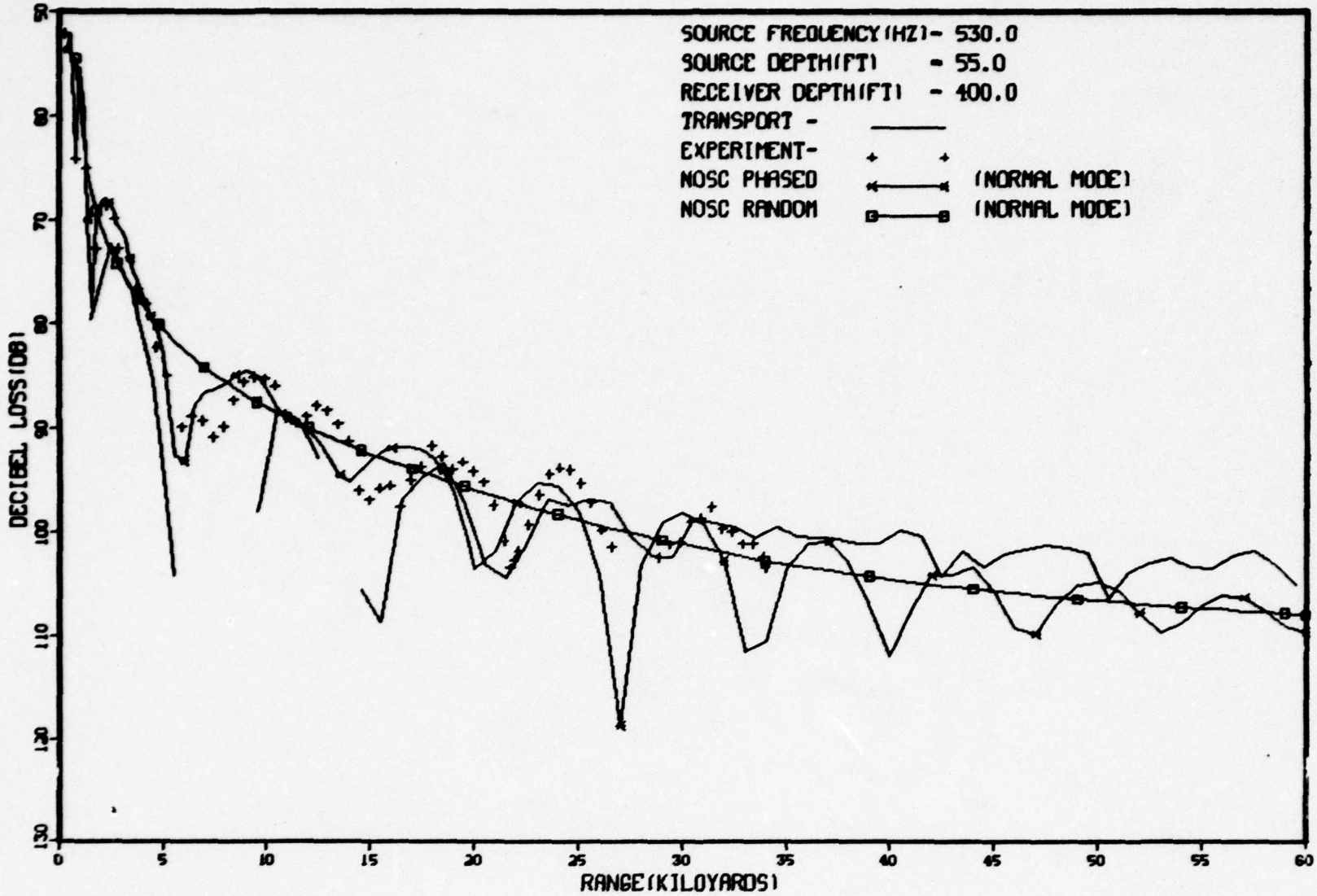

FIG. 4.34, BILINEAR PROFILE, S-O, INTERNAL WAVE SCATTERING(LINEAR)

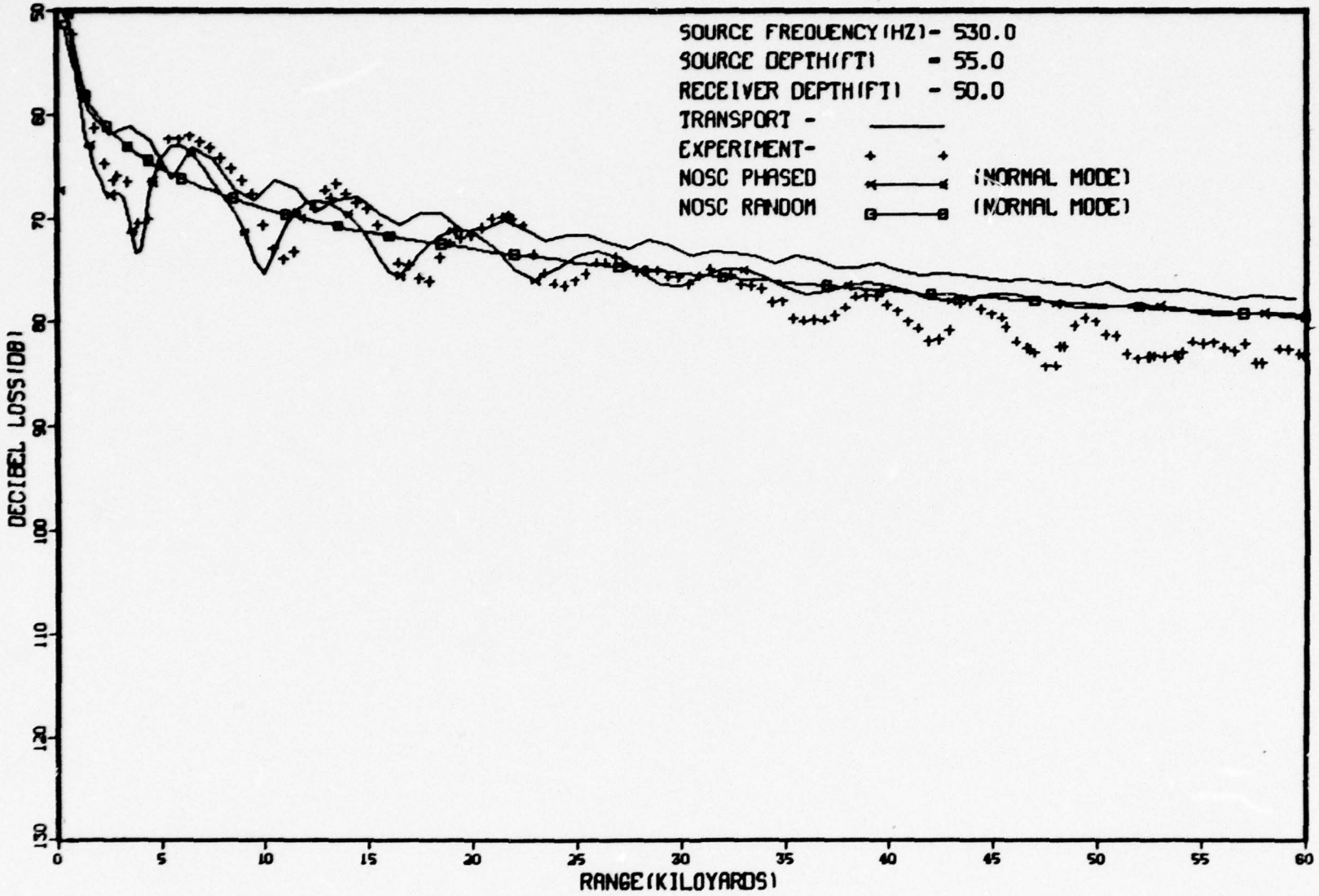

FIG. 4.35, BILINEAR PROFILE, S-O, INTERNAL WAVE SCATTERING(LINEAR)

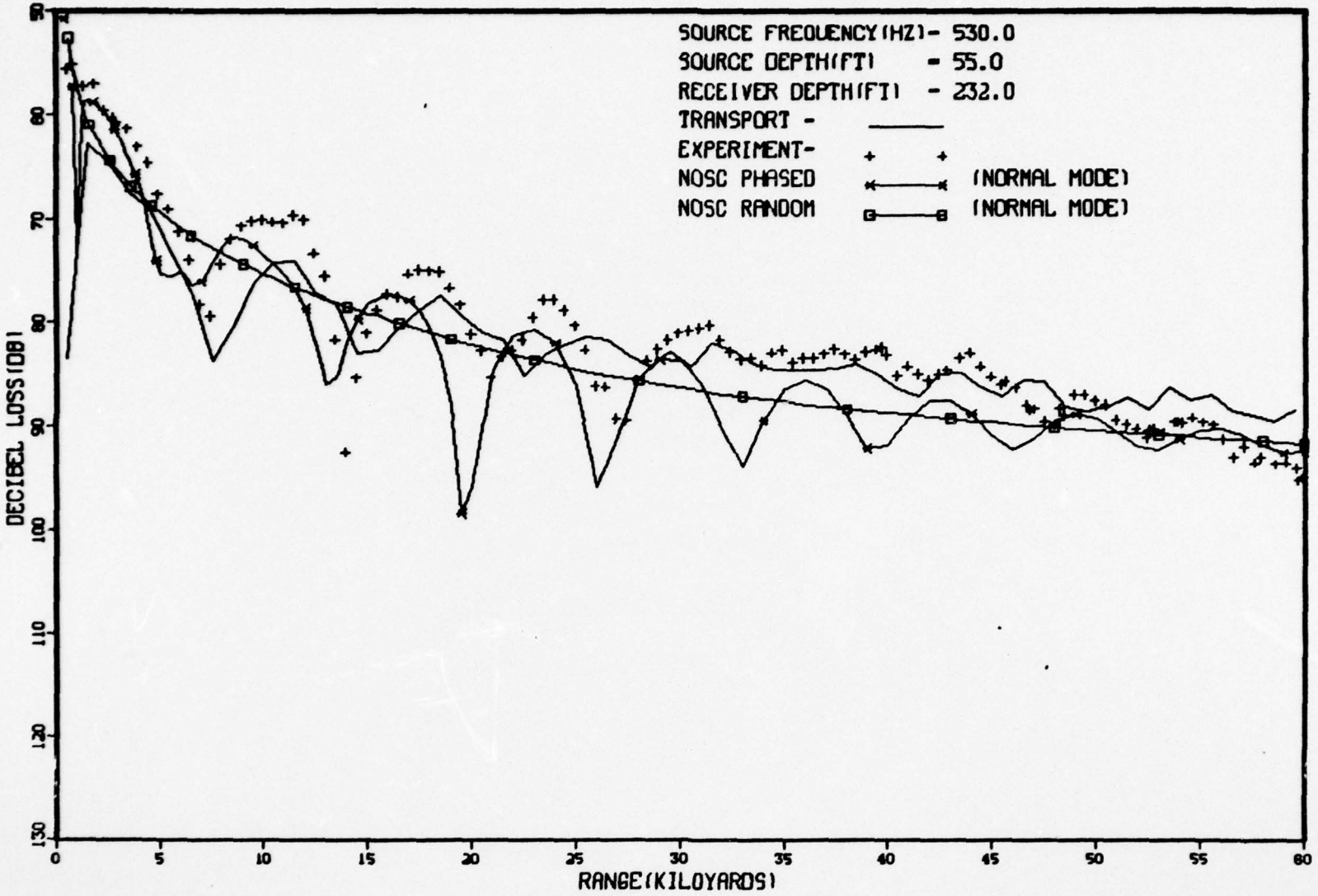

FIG. 4.36, BILINEAR PROFILE, S-0, INTERNAL WAVE SCATTERING(LINEAR)

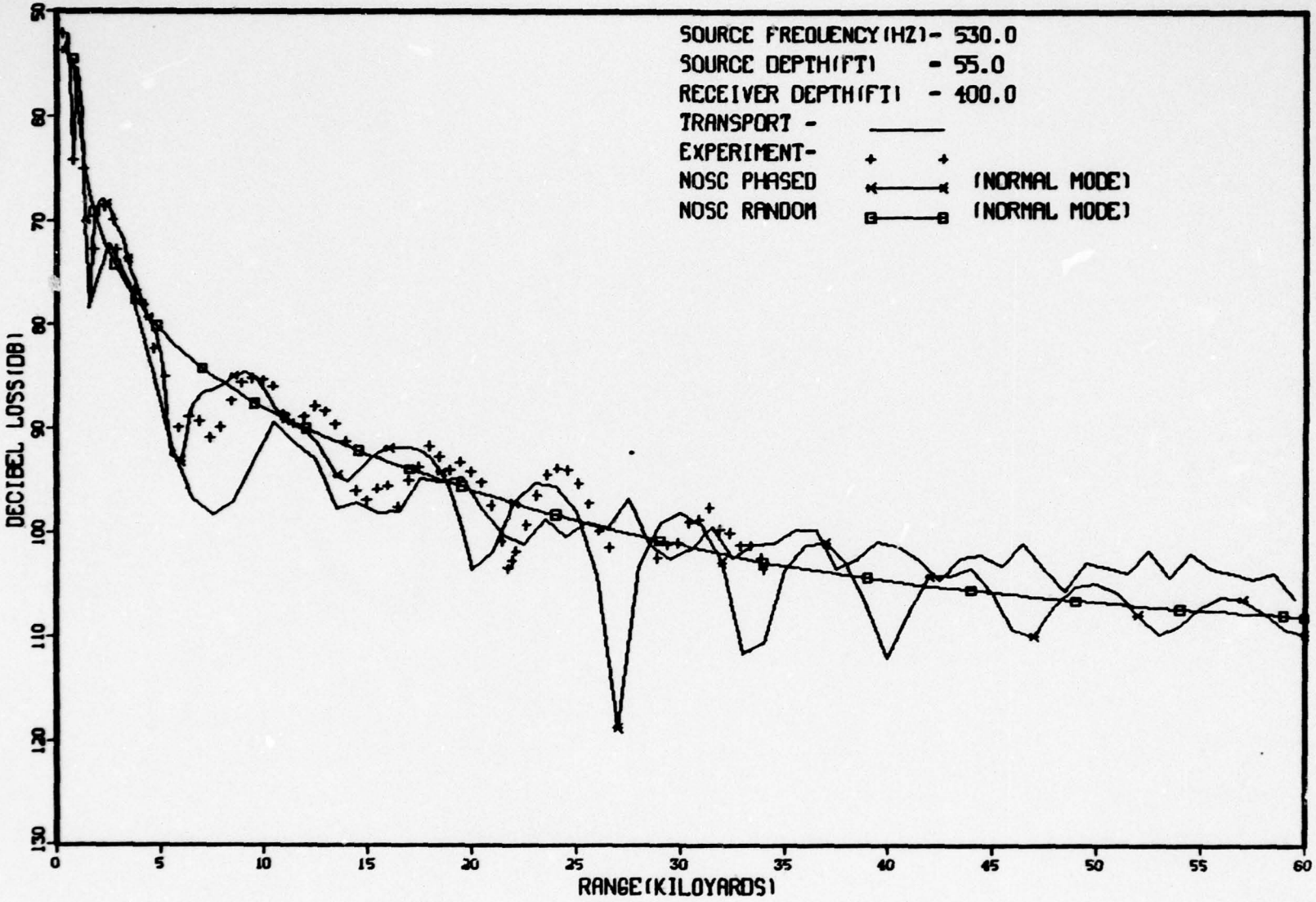

FIG. 4.37, BILINEAR PROFILE, S-.0025, INTERNAL WAVE SCATTERING(LINEAR)

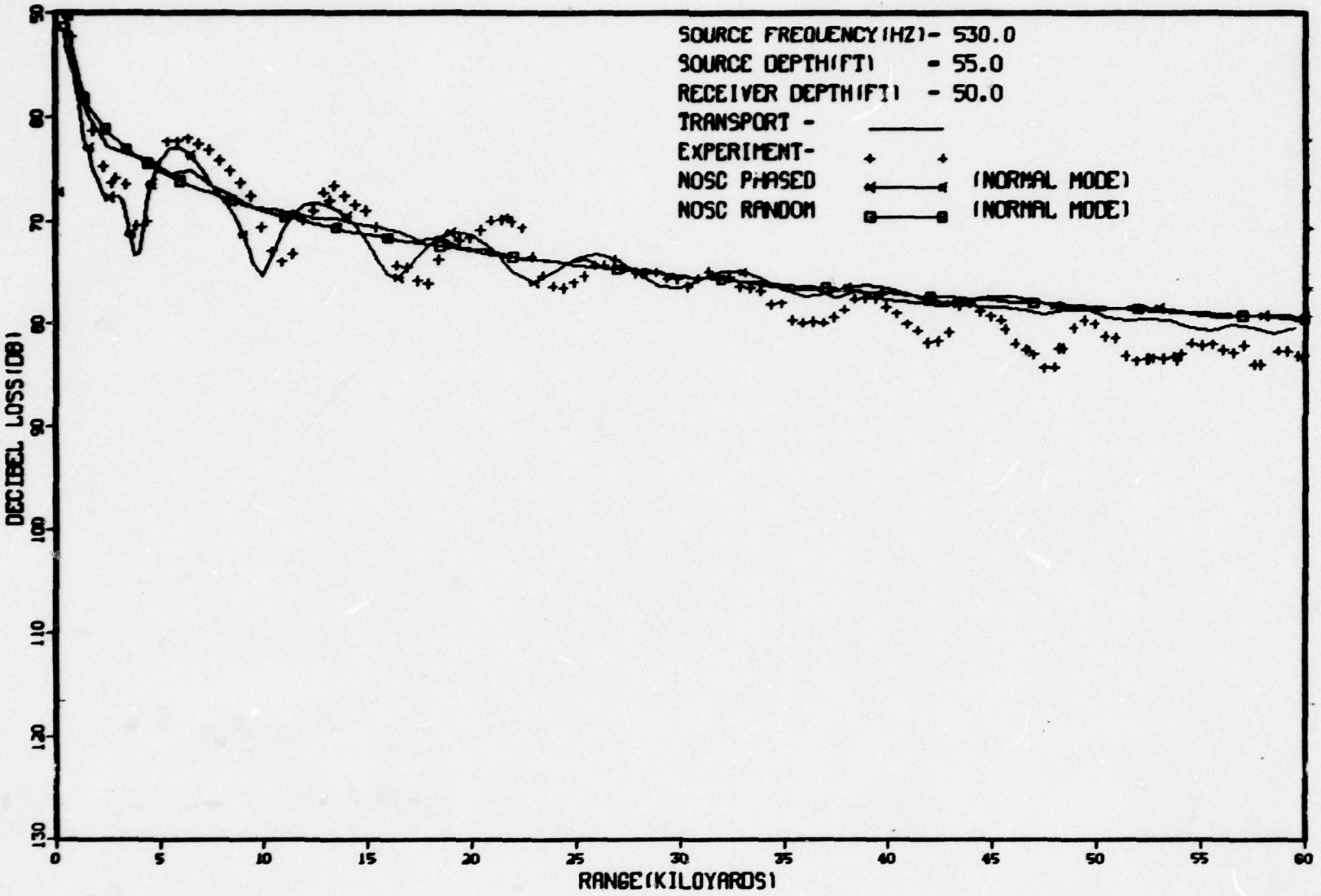

FIG. 4.38, BILINEAR PROFILE, S-.0025, INTERNAL WAVE SCATTERING(LINEAR)

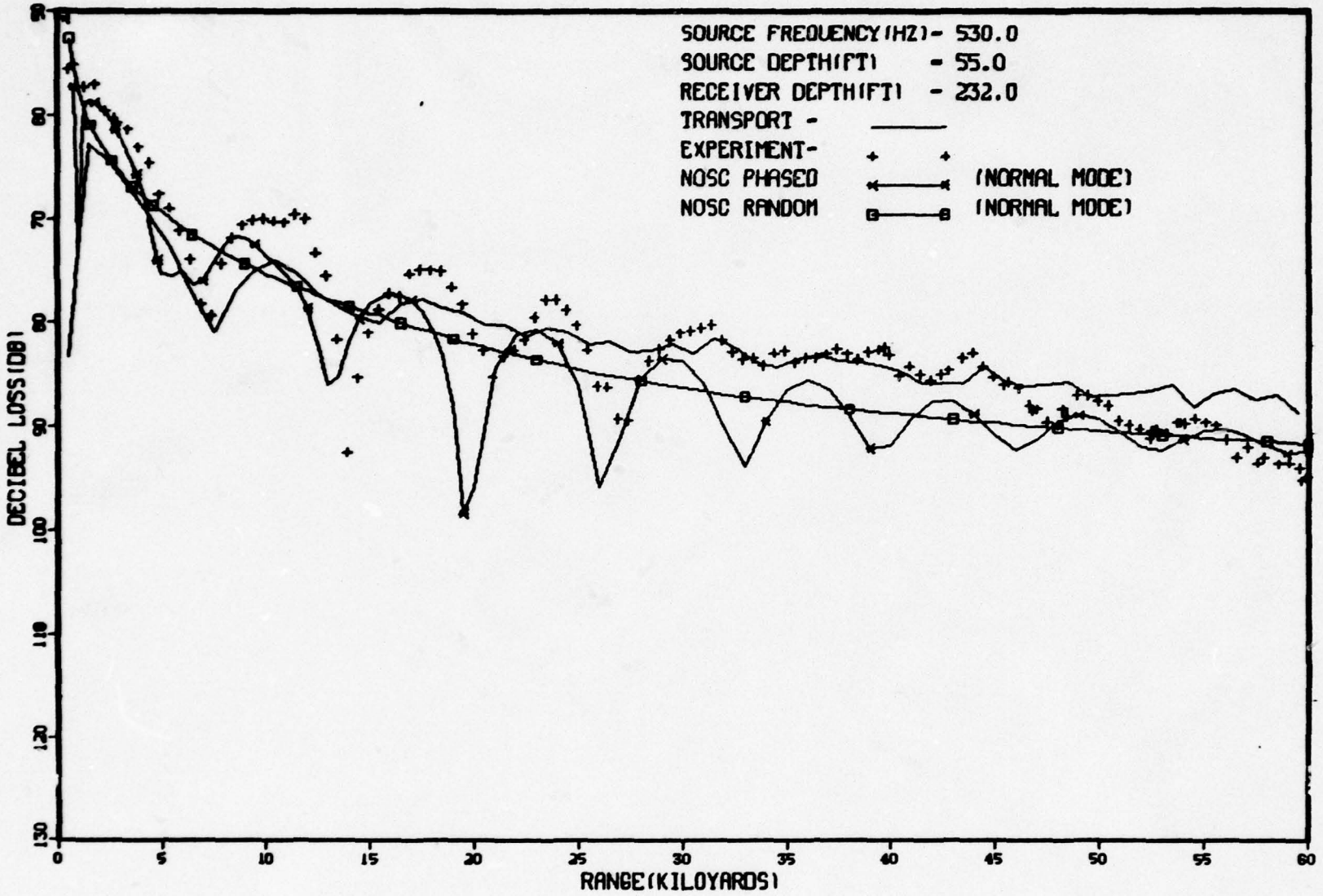

FIG. 4.39, BILINEAR PROFILE, S-.0025, INTERNAL WAVE SCATTERING(LINEAR)

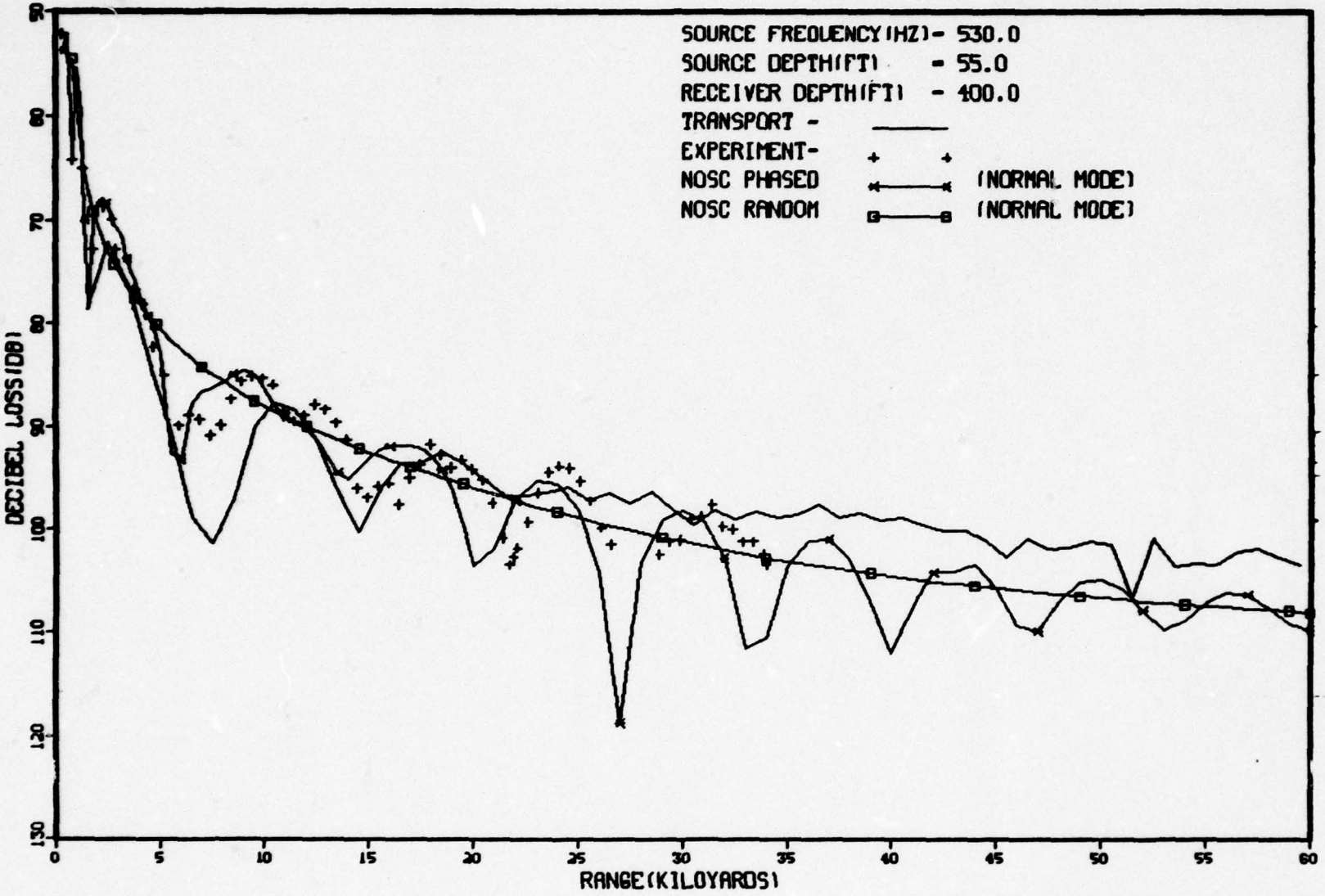

FIG. 4.40, BILINEAR PROFILE , S=.0025, INTERNAL WAVE SCATTERING(QUADRATIC)

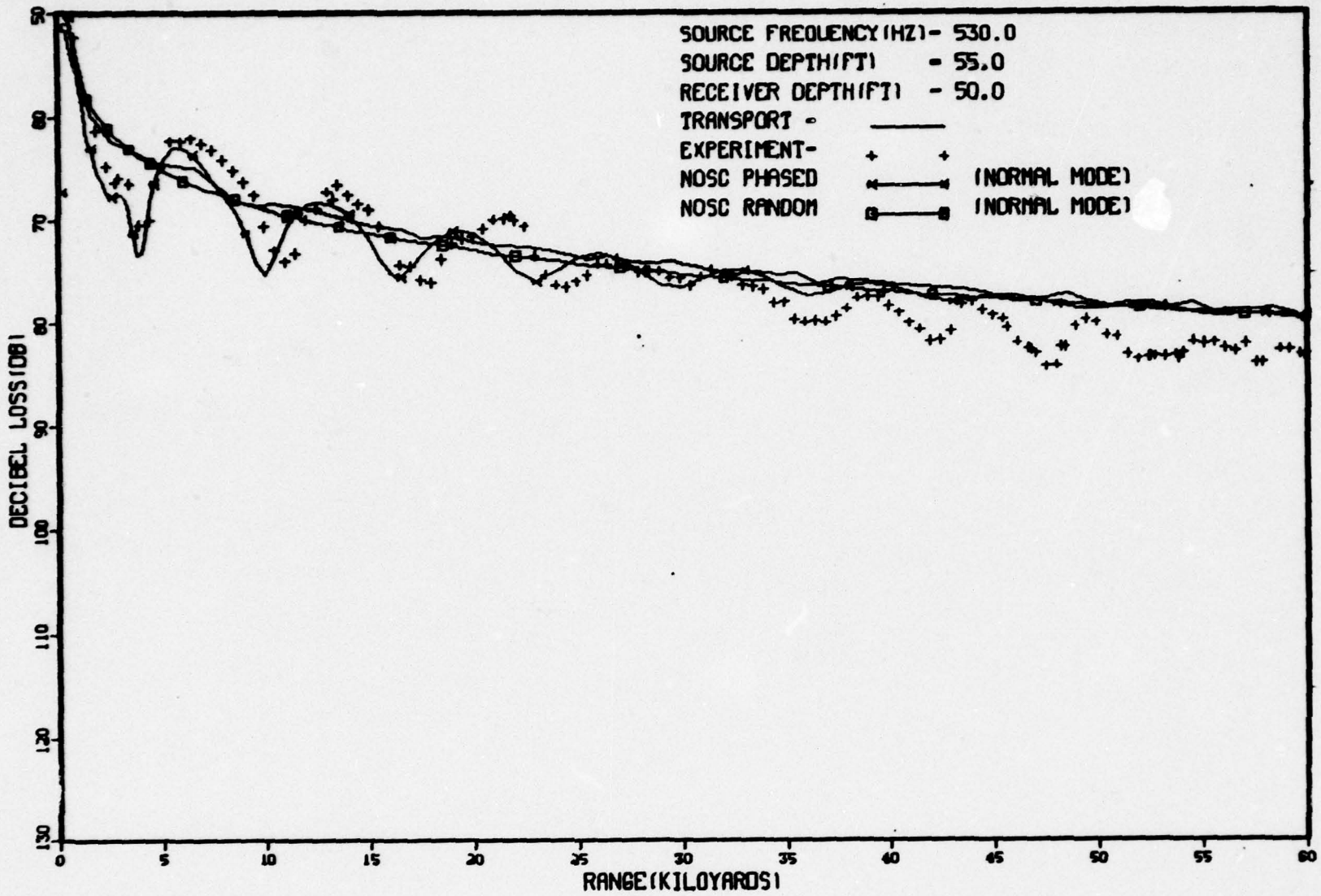

FIG. 4.41, BILINEAR PROFILE ,S-.0025, INTERNAL WAVE SCATTERING(QUADRATIC)

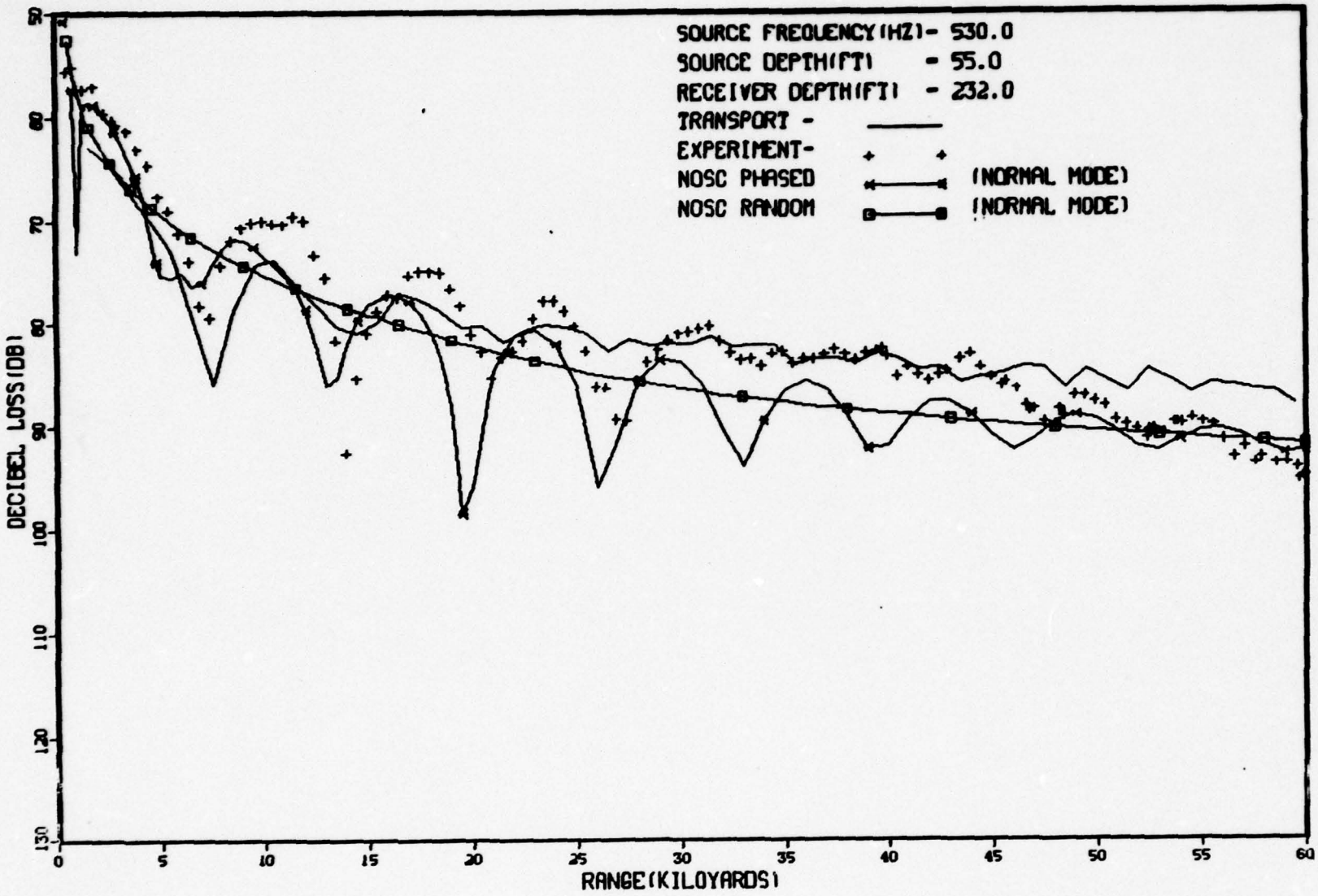

FIG. 4.42, BILINEAR PROFILE , S-.0025, INTERNAL WAVE SCATTERING(QUADRATIC)

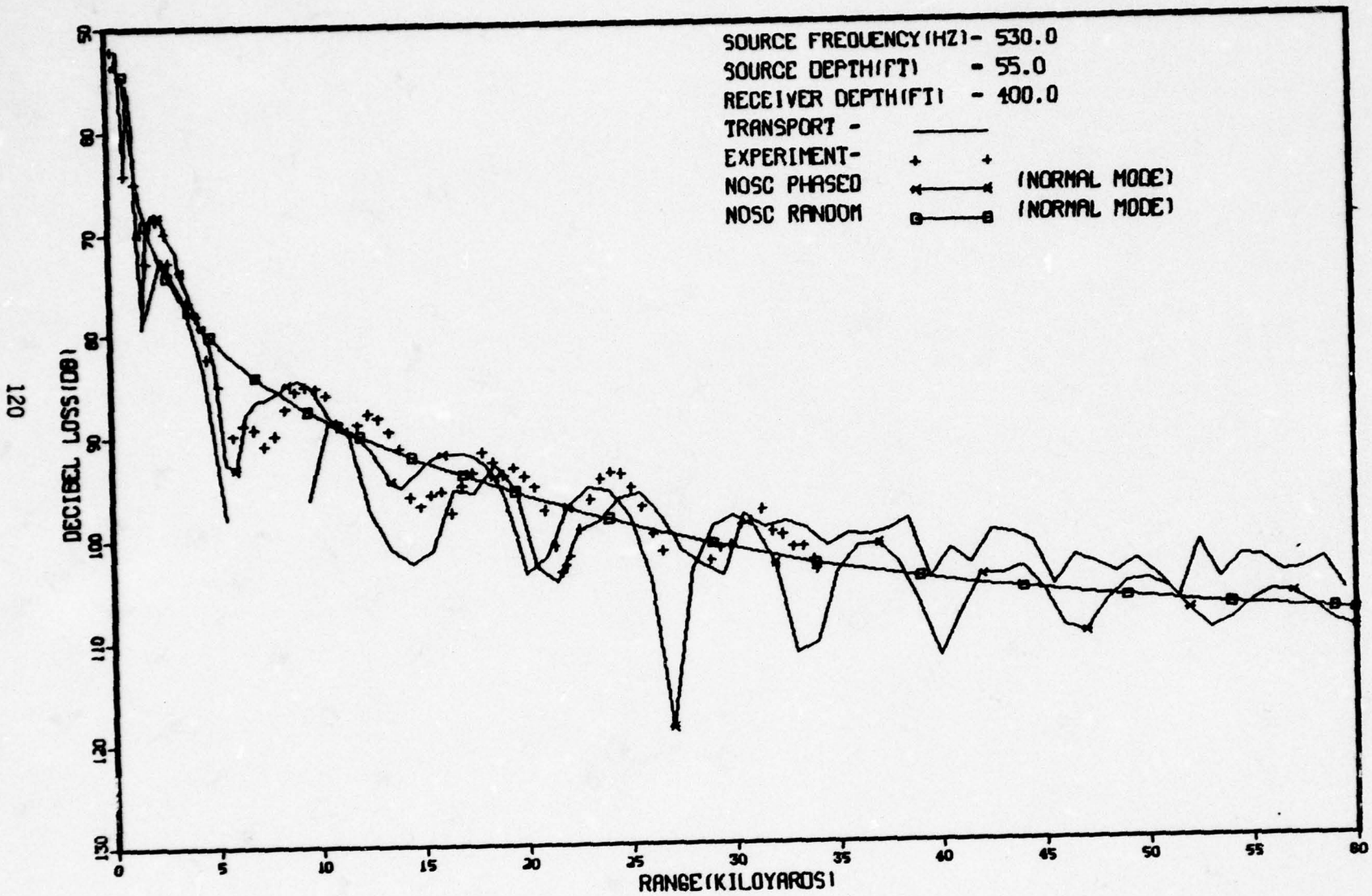

To complete the transport calculational program, we calculated the transport solution using the three-layer model discussed in Section 4.2. This model was used in the early ray calculations described in Reference 31. We decided to use it here because in Figure 4.22 at the 50 foot receiver the transport results appear to fall below the experimental data. As mentioned earlier this may be because of mode interference effects but we wanted to check the three-layer model for model sensitivity in any case. As can be seen from Figures 4.43 - 4.45 the 1030 Hz transport results at the 50 foot receiver are now in better agreement with the experimental data. Also, at the other two depths agreement with experiment is not bad. From this one might conclude that the three-layer model is actually a better description of the surface duct.

To further test the three-layer model we also ran the 530 Hz case, the results of which are shown in Figures 4.46 - 4.48. It is immediately clear from Figure 4.46 that the three-layer model predicts intensities that are too large at the 50 foot receiver. Because the 232 foot results are somewhat insensitive to whether the two- or three-layer profile is used, and because the 400 foot results are probably dominated by diffraction, we can only say, based on the 50 foot data, that the two-layer model is somewhat better.

We had to state that the 400 foot results are <u>probably</u> dominated by diffraction because we actually have no normal mode calculations for the three-layer model. The normal mode results shown in Figures 4.46 - 4.48 are for the two-layer model; we are assuming in making the statement above concerning diffraction that it will be rather insensitive to whether the two- or three-layer model is used.

FIG. 4.43, TRILINEAR PROFILE, S-.0025, INTERNAL WAVE SCATTERING(QUADRATIC)

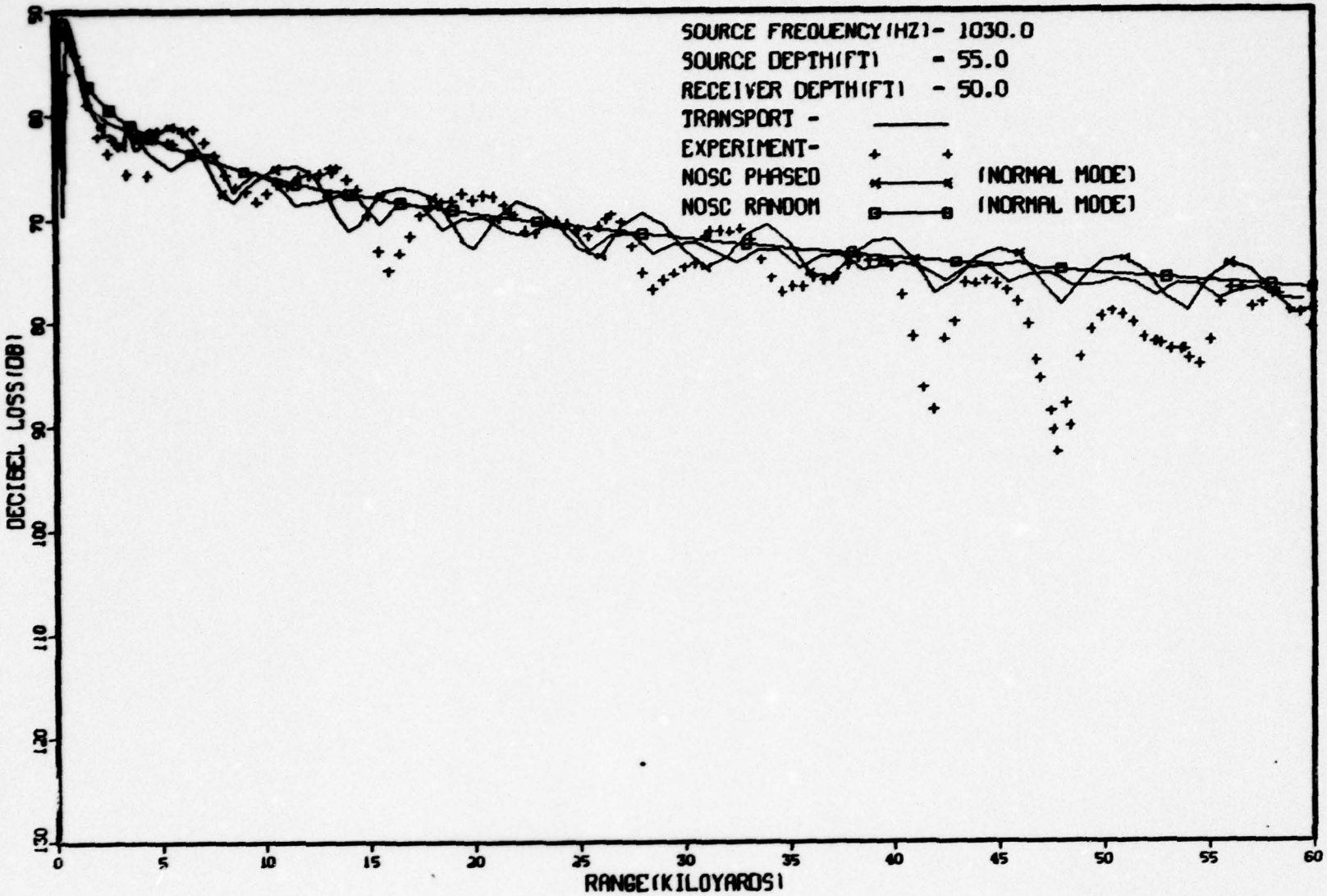

FIG. 4.44, TRILINEAR PROFILE, S-.0025, INTERNAL WAVE SCATTERING(QUADRATIC)

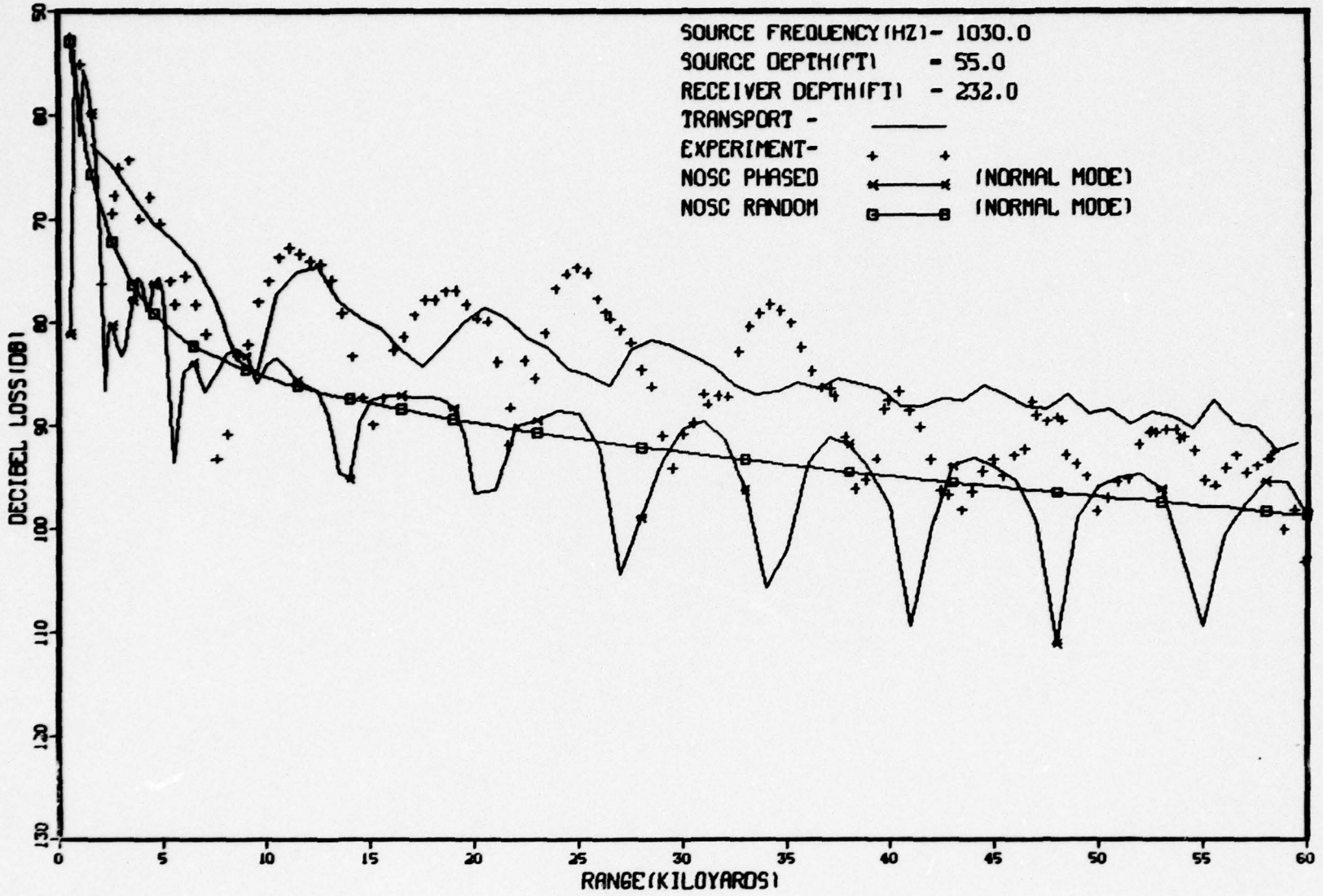

FIG. 4.45, TRILINEAR PROFILE, S-.0025, INTERNAL WAVE SCATTERING (QUADRATIC)

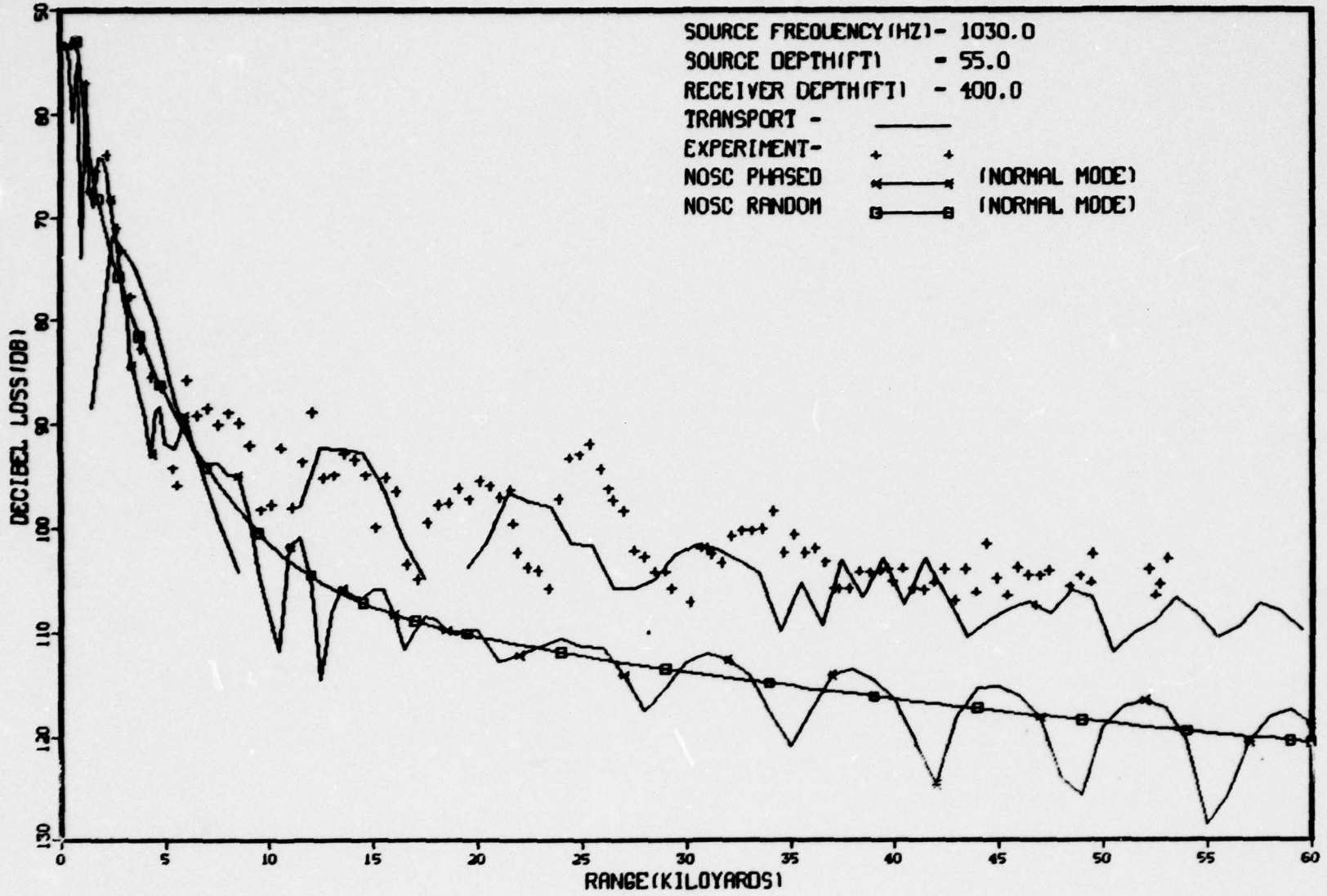

FIG. 4.46, TRILINEAR PROFILE, S=.0025, INTERNAL WAVE SCATTERING (QUADRATIC)

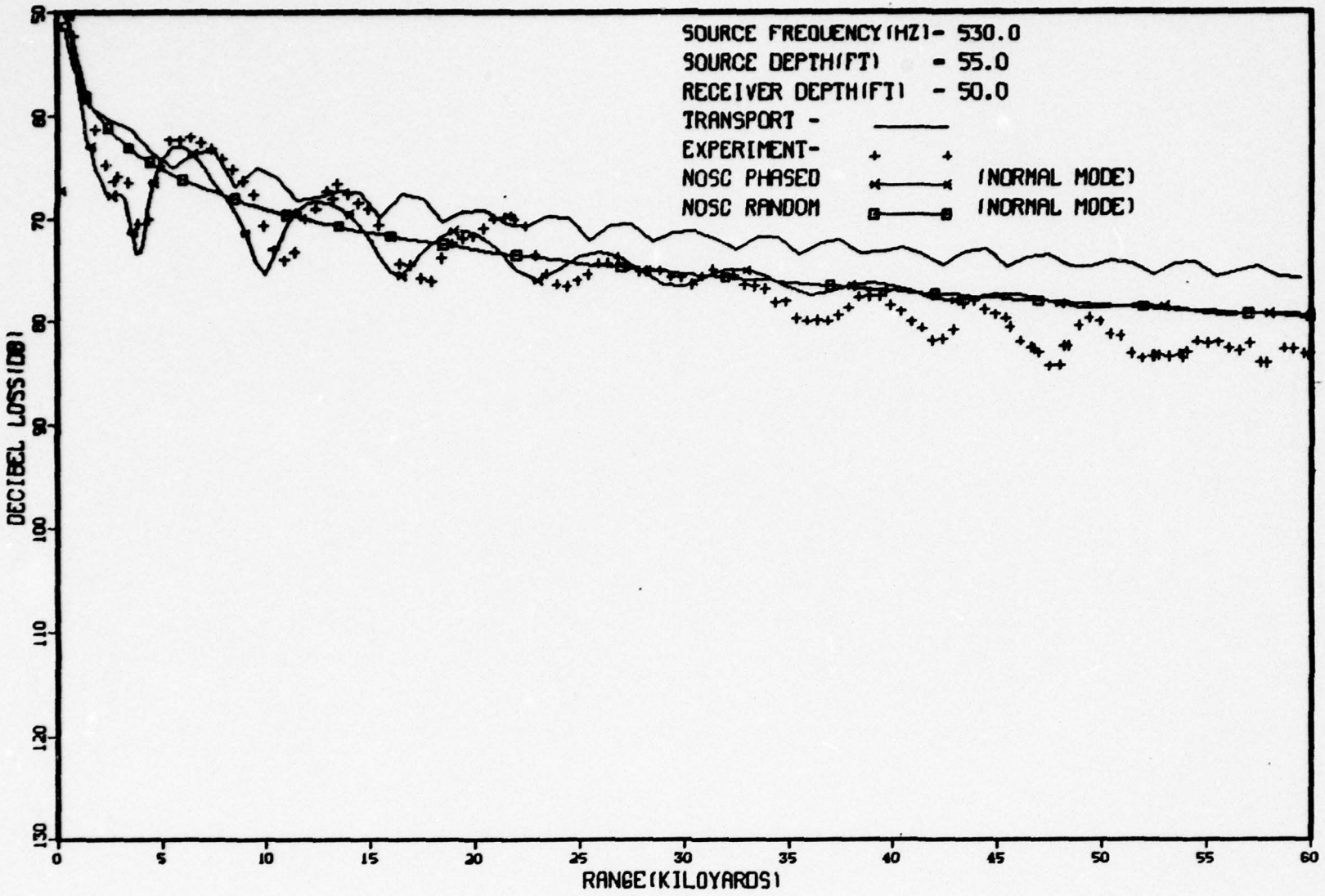

FIG. 4.47, TRILINEAR PROFILE, S-.0025, INTERNAL WAVE SCATTERING (QUADRATIC)

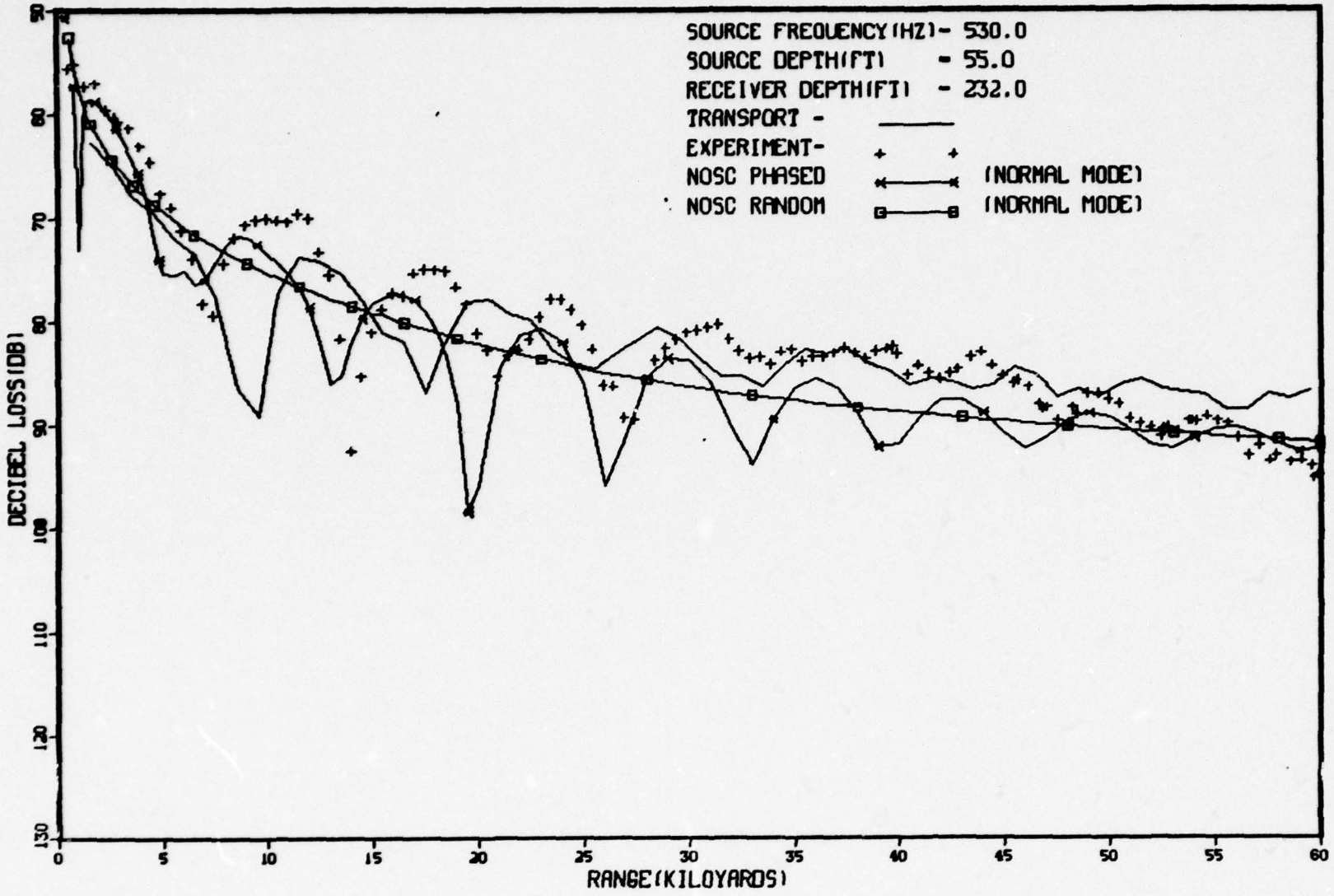

FIG. 4.48, TRILINEAR PROFILE, S=.0025, INTERNAL WAVE SCATTERING(QUADRATIC)

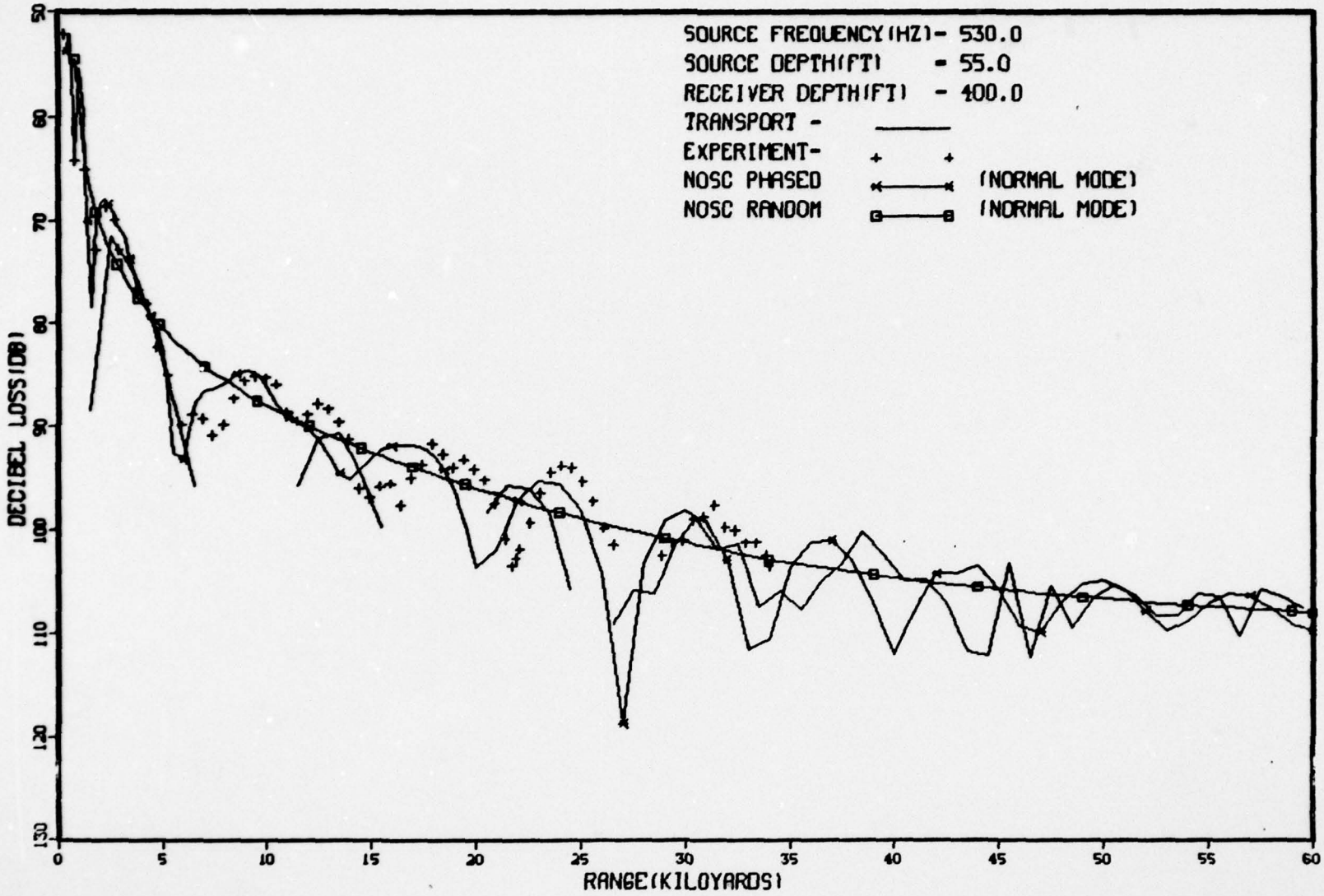

5. CONCLUSIONS

The use of the transport equation for calculating acoustic propagation in a medium where rough surface and volume scattering effects are important has been investigated. The results of the study indicate that, for the surface duct considered, and at 1030 Hz, the below-duct ensonification can be ascribed to two effects. The first of these is scattering by a rough surface. No detailed surface roughness measurements were made during the acoustic propagation experiments that ~~we were comparing our~~ the calculations were compared with, but ~~our~~ the study showed that even a very small swell component could account for much of the energy scattered below the duct. There was some ambiguity in exactly how to describe the surface roughness. ~~We used~~ a sawtooth model is used to which accounted for both shadowing and multiple scatter. Preliminary comparisons of this model with a more realistic sinusoidal model suggest that little difference in the propagation results would have been observed had the sinusoidal model actually been used in the calculations.

The inclusion of volume scattering by internal waves was also studied using the Garrett-Munk description. It was observed that their prescription for the scattering cross section could not be used in the surface duct itself because it led to a far greater scattering of energy out of the duct than was observed experimentally. The more physically reasonable assumption was made that the scattering due to internal waves vanishes at the surface. Two methods of approaching zero were tried (linear and quadratic interpolation) and it was observed that the propagation results were relatively insensitive to exactly how the cross section approached zero at the surface as long as it was linear or stronger.

From this study we can conclude that the transport equation is a powerful tool for calculating acoustic propagation in a medium where random effects are important. It is clear, however, that more accurate

oceanographic measurements will be required if propagation losses are to be ascribed to a particular scattering mechanism. A more recent experiment (SUDS I) has been completed for which detailed surface roughness and sound speed data are available. The application of the transport equation in attempting to explain this data would be a further interesting test of the technique and also of value to the underwater sound propagation community.

Other areas where the transport equation could fruitfully be applied are:

1. Anomalous volume attenuation studies;
2. Convergence zone peaks/widths considering diffraction versus scattering in spreading convergence zone boundaries;
3. Broadband signal propagation;
4. Frequency spreading in a real ocean due to Doppler shifting; and
5. Bottom interactions.

In short, any application where random media effects are important can be efficiently and simply addressed using the transport equation technique.

6. ACKNOWLEDGEMENTS

The authors would like to thank LtC. George Ranes and Dr. E. M. Stanley of NORDA (Code 500) for their interest in bringing the transport equation method to fruition in the underwater acoustics community. Also, the help of M. A. Pedersen and D. White of NOSC (supported by the Long Range Acoustic Propagation Project, NORDA Code 600) was generously given. It was essential for the successful completion of the project. We would also like to thank Dr. Gerald Pomraning for many helpful discussions concerning the surface scattering models and Chuck Spofford for his willingness to discuss the use of the transport equation in further underwater acoustics applications.

Finally, we would like to thank Al Engebretson for his programming expertise in putting together the ACTOR code and Ms. Gayle Wathen for her care in preparing the manuscript.

7. REFERENCES

1. Officer, C. B., Introduction to the Theory of Sound Transmission, Mcraw-Hill, New York (1958).

2. Urick, R. J., Principles of Underwater Sound, McGraw-Hill, New York (1975).

3. "Principles of Underwater Sound," Natl. Defense Res. Comm. Division 6, Summary of Technical Report 7, pp. 90-98, 1947.

4. Tappert, F.D. and Hardin, R. H., Proceedings of the Eighth International Congress on Acoustics, Volume II, p. 452, London: Goldcrest (1974).

5. Tappert, F. D., "Parabolic Equation Method in Underwater Acoustics," J. Acoust. Soc. of Amer. 55, S34A.

6. Besieris, I. M. and Tappert, F. D., J. Math. Phys., Volume 14, No. 12, pp. 1829-1836, December 1973.

7. Besieris, I. M. and Tappert, F. D., J. Math. Phys., Volume 17, No. 5, pp. 734-743, May 1976.

8. Garrett, C. and Munk, W., "Space-Time Scales of Internal Waves," Geophys. Fluid Dyn., Volume 2, pp. 225-264, 1972.

9. Garrett, C. and Munk, W., "Space-Time Scales of Internal Waves: A Progress Report," J. Geophys. Res., Volume 80, No. 3, pp. 291-297, January 20, 1975.

10. Flatte´, S. M., and Tappert, F. D., "Calculation of the Effect of Internal Waves on Oceanic Sound Transmission," J. Acoust. Soc. of Amer., 58, No. 6, pp. 1151-1159, December 1975.

11. Pedersen, M. A. and Gordon, D. F., "Normal-Mode Theory Applied to Short-Range Propagation in an Underwater Acoustic Surface Duct," J. Acoust. Soc. of Amer. 37, No. 1, pp. 105-118, January 1965.

12. Pedersen, M. A., private communication.

13. Wigner, E. P., "On the Quantum Correction for Thermodynamic Equilibrium," Phys. Rev. 40, p. 749, 1932.

14. Foldy, L. L., "The Multiple Scattering of Waves," Phys. Rev. 67, Nos. 3 and 4, pp. 107-119, February 1945.

15. Watson, K. M., "Quantum Mechanical Transport Theory," Phys. Rev. 118, No. 4, pp. 886-898, May 1960.

16. Watson, K. M., "Multiple Scattering of Electromagnetic Waves in an Underdense Plasma," J. Math. Phys. 10, No. 4, pp. 688-702, April 1969.

17. Watson, K. M., "Electromagnetic Scattering Within a Plasma in the Transport Approximation," Phys. Fluids 13, No. 10, pp. 2514-2523, October 1970.

18. Richtmyer, R. D. and Morton, K. W., Difference Methods for Initial Value Problems, 2nd Edition, Wiley, New York (1967).

19. Straker, E., Scott, W. H., Jr. and Bryn, N. R., "The Morse Code with Combinatorial Geometry," DNA 2860T, May 1972.

20. Fleck, J. Jr., Monte Carlo Method in Radiation Transport, Methods in Computational Physics, Volume 1, Academic Press, New York (1962).

21. Fleck, J. Jr. and Cummings, J. O., "An Implicit Monte Carlo Scheme for Calculating Time and Frequency Dependent Non-linear Radiation Transport," Report Number UCRL-72924, Lawrence Radiation Laboratory, Livermore, California, 1970.

22. Carter, L. L. and Cashwell, E. D., Particle-Transport Simulation with the Monte Carlo Method, ERDA Critical Review Series TID-26607, (1975).

23. Cashwell, E. D. and Everett, C. J., A Practical Manual on the Monte Carlo Method for Random Walk Problems, Pergamon Press (1959).

24. Pierson, W. J., Jr. and Moskowitz, L., " Proposed Spectral Form for Fully Developed Wind Seas Based on the Similarity Theory of S. A. Kitaigorodskii," J. Geophys. Res. 69, No. 24, 1964.

25. Schneider, H. G., "Rough Boundary - Scattering in Ray-Tracing Computations," Acustica 35, No. 1, pp. 18-25, 1976.

26. Cox, C. and Munk, W., "Statistics of the Sea Surface Derived from Sun Glitter," J. Marine Res. 13, p. 198, 1954.

27. Kinsman, B., Windwaves, Prentice Hall, Inc., Englewood Cliffs, New Jersey (1965).

28. Watson, K. M., private communication of Chapter 13 of Sound Transmission Through a Fluctuating Ocean, to be published, Stanley M. Flatte', Editor.

29. Sound Transmission Through a Fluctuating Ocean, S. M. Flatte' Editor, to be published.

30. Pedersen, M. A. and White, D., private communication.

31. Pedersen, M. A., "Comparison of Experimental and Theoretical Image Interference in Deep-Water Acoustics," J. Acous. Soc. Amer., 34, No. 9, Part 1, pp. 1197-1203, September 1962.

32. Pedersen, M. A., private communication.

33. Pedersen, M. A., private communication.

APPENDIX A

PRELIMINARY TEST PROBLEM FOR THE ACTOR CODE

Because ACTOR is a totally new code in the underwater acoustic propagation area, we felt that it would be desirable to run a test problem without surface scattering or internal wave scattering and compare the results obtained with a standard ray theory code also without the mentioned scattering mechanisms. Under these conditions the two codes should be in almost exact agreement. The problem selected for this purpose was the two-layer duct whose properties were given in Table 4.2.

As was the case during the actual experiment discussed in Section 4.1 the source was at a depth of 55 feet and the propagation loss versus range curves were calculated at depths of 50, 232 and 400 feet. A comparison of propagation loss as calculated by the ray theory code and the transport code for these depths is given in Figures A.1 - A.3. The corresponding ray diagram is provided in Figure A.4. Both the ray diagram and the ray code propagation loss data were provided by D. White and M. Pedersen* of NOSC.

These figures clearly indicate that the ray and transport codes are in very good agreement. Also, from the ray diagram, we see that at the 232 foot level the transport code is predicting shadow zones at the right places and of the right width in range.

Also, at the 400 depth, both codes predict a total shadow zone beyond 5 kyd. However, as mentioned in Section 4, this region can be ensonified due to scattering or diffraction.

The calculations discussed in this Appendix were actually run before any attempt was made to compare calculated results with experimental data. The results of this test problem indicated that the transport code was doing the particle tracking correctly and that the absorption and editing algorithms were properly formulated.

---

* White, D. and Pedersen, M., private communication.

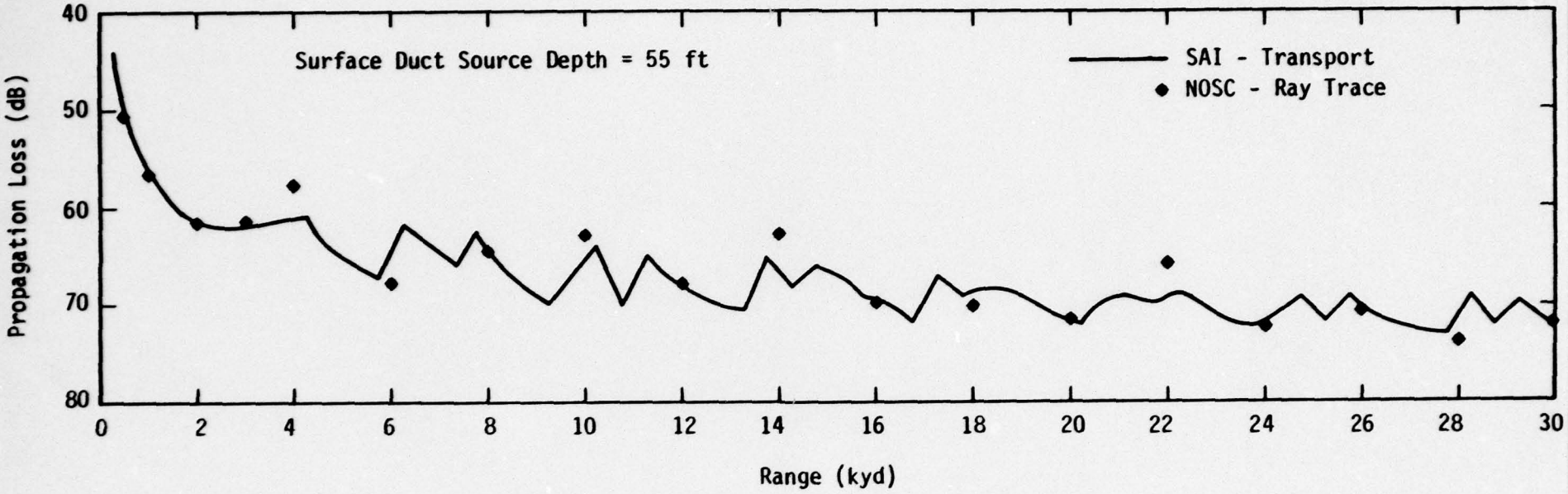

Figure A.1. Propagation Loss Versus Range for the 50 ft Receiver.

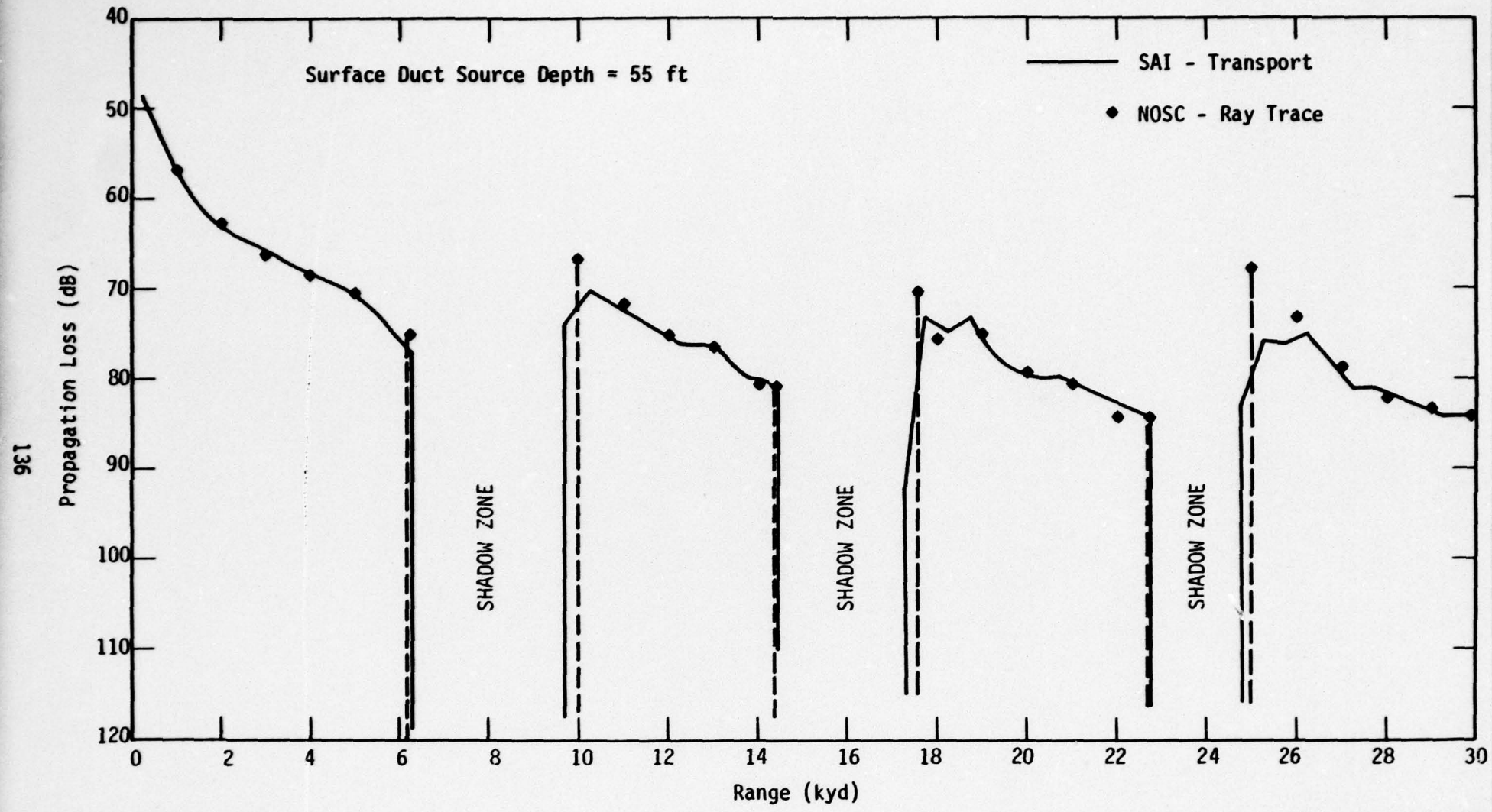

Figure A.2. Propagation Loss Versus Range for the 232 ft Receiver.

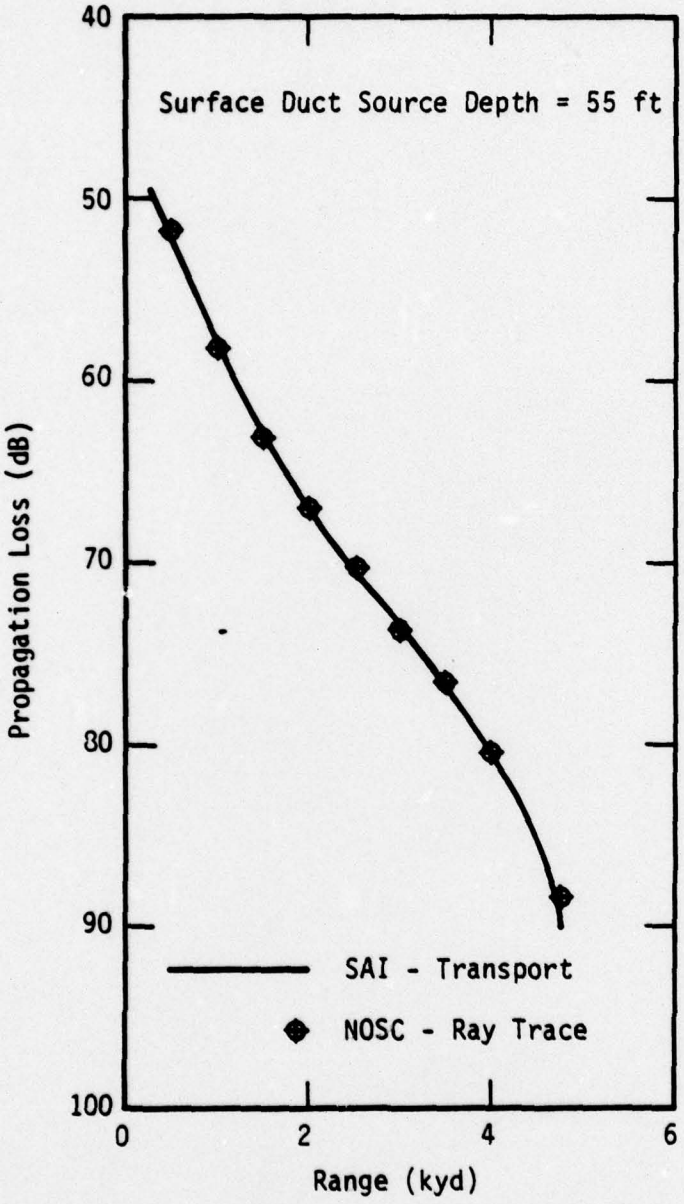

Figure A.3. Propagation Loss Versus Range for the 400 Foot Receiver.

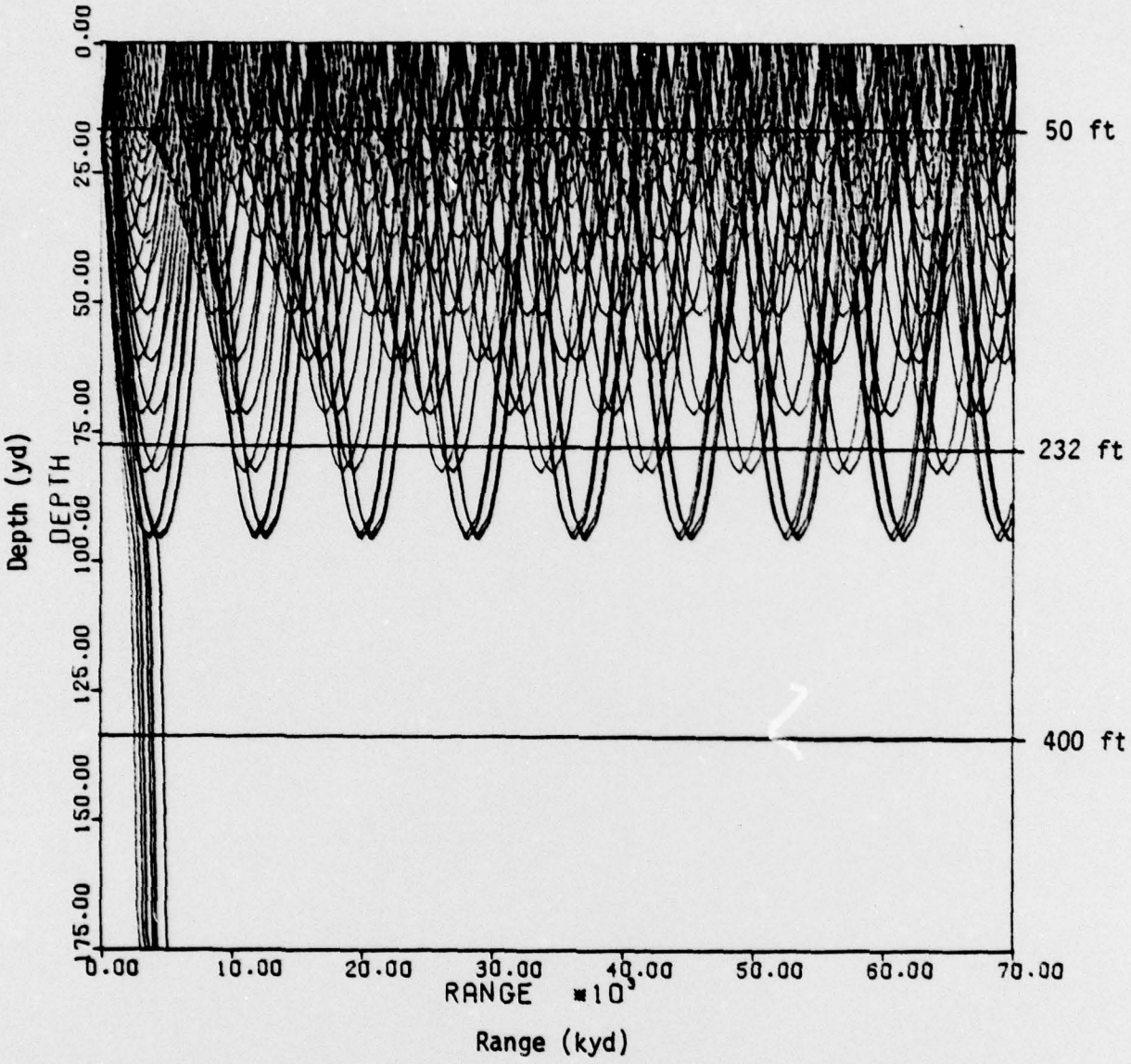

Figure A.4. Ray Diagram for the Two-Layer Duct Showing the Shadow Zones for the 232 Foot Receiver. The Limiting Rays for Propagation are at ± 2.41°.

APPENDIX B

RANDOM NUMBER GENERATION TEST

The random number generation scheme used in ACTOR makes use of the multiplicative congruential method.[†] We ran singlet, doublet, and triplet tests, each type consisting of three sets.

The random number generator is given by

$$x = \lambda x_{i-1} \pmod{m}, \quad m = 2^{48} \quad .$$

The set 2 x_0 is the last random number from set 1 and the set 3 x_0 is the last random number from set 2. The parameters for the various sets were as given in Table B.1.

Table B.1. Parameters for Uniformity Tests.

SET 1	SET 2	SET 3
x_0=2000105715252220103 1	x_0=2000705034651265437 1	x_0=2000644354167473263 1
λ=2000000000100000053	λ=same as set 1	λ=same as set 1

The chi-square test is expressed by the following equation*

$$V = \sum_{s=1}^{k} \frac{(Y_s - np_s)^2}{np_s} \qquad (B.1)$$

[†] Spanier, J. and Gelsord, E. M., Monte Carlo Principles and Neutron Transport Problems, Addison Wesley Publishers, (1969).

* Knuth, D. E., The Art of Computer Programming, Volume 2, Addison-Wesley, Reading Massachusetts (1969).

where

n = number of independent trials

k = number of possible outcomes of a single trial

Y_s = actual number of trials which resulted in outcome s

p_s = probability that each trial results in outcome s.

We ran the random number test so that there were 729 possible outcomes for each set and n was set equal to 729,000. The singlet test places each random number in the appropriate equi-sized slot in a one-dimensional array of size 729. The doublet test places successive pairs of random numbers in the appropriate equi-sized slots in a 27 x 27 two-dimensional array and 729,000 pairs were generated. The triplet test proceeds similarly for a three-dimensional array of size 9 x 9 x 9. To fully test a random number generator all p-tuples should be tested where $p \to \infty$. Clearly this is a practical impossibility and we have settled on $p \leq 3$.

The results of all these tests are shown in Figure B.1. Values of V from Eq. (B.1) which lie above 820 or below 640 would be suspect. This would especially be so if it happened, say, two out of three times. As can be seen from the figure, however, for all of our tests the value of V lies in the acceptable range. In this figure O_1 refers to the first singlet set, O_2 the second, etc.

We have also included the results obtained using the Control Data supplied random number generator. Only one set of each type was checked for the CDC case.

As can be seen from the figure, both random number generators appear to be satisfactory. From these results one might ask why we bothered with our own random number generator since the one provided by CDC appears to be adequate. The reason is that in going from one installation to another it is never certain that the starting seeds are the same. In order that certain test problems be reproducible, we have found it much easier to carry our own random number generator.

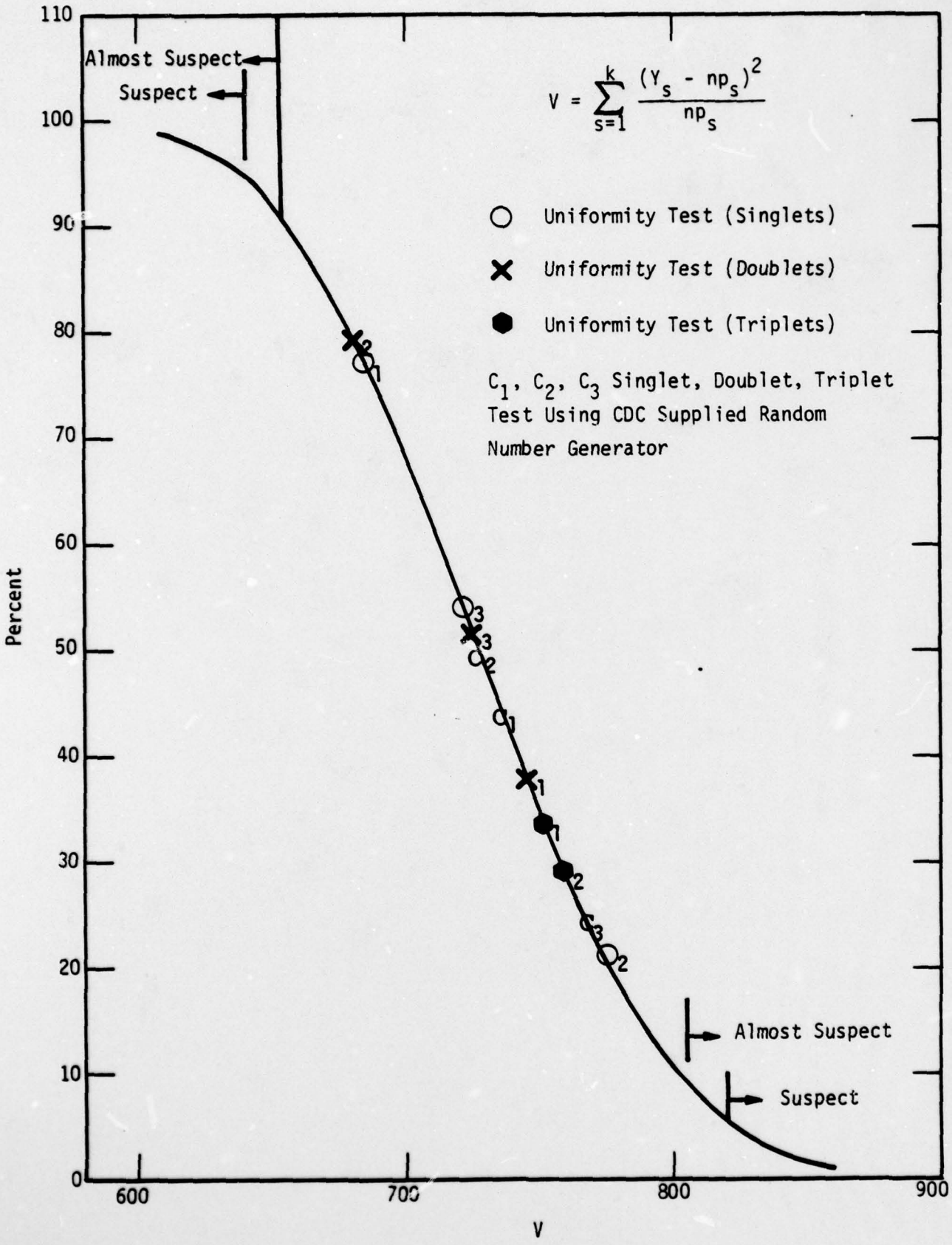

Figure B.1. Results from Random Number Chi-Squared Tests.